RICE UNIVERSITY

Direct Water and Fat Determination in Two-Point Dixon Imaging

by

Olen Henry Rambow

A THESIS SUBMITTED
IN PARTIAL FULFILLMENT OF THE
REQUIREMENTS FOR THE DEGREE

Master of Science

APPROVED, THESIS COMMITTEE:

John W. Clark, Jr., Chair
Professor, Electrical and Computer Engineering

Jingfei Ma
Professor, Department of Imaging Physics, The University of Texas MD Anderson Cancer Center

Thomas C. Killian
Professor and Chair, Physics and Astronomy

Kevin F. Kelly
Associate Professor, Electrical and Computer Engineering

HOUSTON, TEXAS
April 2013

ABSTRACT

Direct Water and Fat Determination in Two-Point Dixon Imaging

by

Olen Henry Rambow

The Dixon technique is a well-established method in magnetic resonance imaging for obtaining separate images of water and fat. Here we present a generalized solution to the two-point Dixon problem with a geometric interpretation, allowing for flexible echo times and a multi-peak fat model. By simulation and experiment, we have analyzed the dependence on the echo times of the error in the water, fat, and relative background phasor values due to both signal noise and T_2* decay. Furthermore, we have demonstrated that broken symmetry due to the multi-peak nature of fat enables direct water and fat determination without phase correction, and we have quantified the reliability of this technique as a function of the echo times. The results may provide valuable guidance for selecting scan parameters to balance the objectives of optimizing fat-water identification, minimizing error in the pixel values, and minimizing total scan time.

Acknowledgments

I would like to extend my sincere gratitude to the following people for their guidance and support. Thanks to Jingfei Ma for introducing me to MRI, directing me to the frontiers of the field, and providing me with invaluable opportunities for growth. Thanks to John Clark for taking me under his wing, helping me to find the path that was right for me, and giving me much-needed wise counsel. Thanks also to Kevin Kelly and Tom Killian, both for their guidance and for serving on my committee. I am also tremendously grateful to Randy Hulet, Qimiao Si, and Frank Jones for their help and encouragement. Finally, thanks to my family and friends for always being there for me throughout the travails of graduate school.

Contents

List of Figures

List of Tables

Nomenclature

2D imaging: a process in which only one slice is excited at a time and the 2D Fourier transform of each slice is acquired separately.

3D imaging: a process in which a 3D volume is excited and phase-encoding gradients are applied in both the *y* and *z* directions to obtain a true 3D Fourier transform of the image.

90° pulse (or π/2-pulse): the initial RF excitation pulse that tips the magnetization vector into the transverse plane and results in the precession that gives rise to the resonance signal.

180° pulse (or π-pulse): an RF pulse used in spin echo imaging to flip all magnetization isochromats across an axis in the transverse plane in order to rephase the signal, thereby generating a spin echo.

chemical shift (σ): the difference in resonance frequency, measured in ppm, between the hydrogen nuclei in some chemical species of interest (most typically fat) and hydrogen nuclei in water.

coil: a receiver or array of receivers used to detect the magnetic resonance signal.

Dixon imaging: any method for obtaining separate water-only and fat-only images by selecting echo times to yield fat-water phase differences that enable the calculation of the water and fat components in post-processing.

echo spacing: the difference between echo times when two images are acquired with different echo times.

echo time (*TE*): the time between the excitation pulse and the sampling of the central point in k-space.

fat fraction (*Q*): the ratio of the amount of fat to the sum of the amounts of fat and water in a given voxel; $Q = F/(F + W)$.

gradient echo: the signal maximum that occurs during the application of a magnetic field gradient at the moment when spins are in phase (at the center of a line in k-space).

isochromat: a microscopic region in which all spins are precessing at the same frequency. This is the bridge between the quantum mechanical and classical pictures of magnetic resonance.

MRI/NMR: These acronyms are *not* interchangeable. MRI (magnetic resonance imaging) refers specifically to applications in which field gradients are applied in order to generate an *image* of the object being studied. NMR (nuclear magnetic resonance) is a more general term that refers to the phenomenon that makes MRI possible and includes applications besides MRI such as spectroscopy experiments in which images are not generated.

phantom: any artificial object that is designed to be scanned for testing, calibration, or research purposes, such as a fake human torso or a bottle with compartments that contain different concentrations of solution.

phase encode gradient/direction: the gradient or the direction along which the gradient is applied (most often taken to be the *y* direction) that fixes the *y* value in k-space before the readout gradient is applied in another direction (usually the *x* direction). Unlike the readout gradient, the phase encode

gradient is not present during signal sampling; it is only turned on for short bursts between the acquisitions of different lines in k-space in order to move from one line to the next.

pulse sequence: a programmed set of RF pulses and applied magnetic field gradients that are carefully timed to yield an image with desired characteristics (such as T_2-weighted contrast). A typical pulse sequence consists of an initial RF pulse to excite the tissue followed by a series of magnetic field gradients that are used to traverse k-space while the signal is being sampled.

readout gradient/direction: the gradient or the direction along which the gradient is applied (most often taken to be the *x* direction) that varies the *x* value in k-space during signal sampling. During one application of the readout gradient, an entire line in k-space is sampled.

repetition time (*TR*): the time between consecutive RF excitation pulses. Since the resonance signal decays within about one second after initial excitation, the object being imaged must be excited repeatedly before enough points in k-space can be sampled to generate a satisfactory image.

RF pulse (radio-frequency pulse): an electromagnetic wave, typically circularly polarized and with a frequency at or near the Larmor frequency, that is applied to manipulate the magnetization vector in the tissue being imaged. The most familiar RF pulse is the initial 90° pulse (or $\pi/2$-pulse) that tips the magnetization vector into the transverse plane and results in the precession that gives rise to the resonance signal. Another common RF pulse is the 180°

pulse (or π-pulse) used in spin echo imaging to flip all isochromats across an axis in the transverse plane in order to rephase the signal, thereby generating a spin echo.

slice select gradient/direction: the gradient or the direction along which the gradient is applied (usually taken to be the *z* direction) that determines the *z* coordinate of the slice to be imaged (in 2D imaging). The slice select gradient is only present during the initial RF excitation pulse in order to limit the region that is excited.

spin: a hydrogen nucleus, typically in a water or fat molecule, which behaves like a magnetic dipole and precesses in a magnetic field, thereby giving rise to the magnetic resonance (MR) signal.

spin echo: the signal maximum that occurs when precessing spins rephase after the application of a 180° RF pulse.

voxel: volume element, just like a pixel but 3D; can refer to the actual volume in the object being imaged or to the corresponding element in the image as stored or viewed on a computer.

Introduction

This thesis describes advancements in the two-point Dixon technique, which is a method in the field of magnetic resonance imaging (MRI) for distinguishing between the signals from protons in fat molecules and protons in water molecules.[1] It is one of several techniques[2] that fall under the category of "fat-water separation" or "fat suppression" and are important for the following two reasons. First, they enable the removal of fat from an image, thereby improving the visibility of anatomical and pathological features of interest.[3] Second, they make possible the quantification of the fat content of imaged tissue, thereby enabling the accurate identification of masses of interest based on tissue composition.[4]

Before discussing specific problems in Dixon imaging that are of current interest, we present a brief introduction to the principles of MRI in Chapter 1, "Foundations of MRI," aimed at readers who have a background in physics but are unfamiliar with MRI. Readers who already understand how MR images are acquired

and are familiar with basic contrast mechanisms (specifically, T_1 and T_2 weighting) may wish to skip Chapter 1.

In Chapter 2, "Fat-Water Separation and the Dixon Technique," we summarize the principles of fat-water separation and the traditional two-point Dixon technique in particular. The recent advancements (as of the time of this writing) that led to the problems addressed in this work are described in detail. Then in Chapter 3 we present a generalized solution to the two-point problem along with our own geometric interpretation, which is especially useful as a visual aid for understanding the main problems addressed in this work.

The three main projects addressed in this thesis are presented in Chapter 4, Chapter 5, and Chapter 6 and are motivated by two recent advancements in two-point Dixon imaging. The first is the extension of the technique to allow arbitrary echo times[5,6] (as opposed to the traditional in-phase/opposed-phase times), and the second is the incorporation of a multiple-spectral-peak model[7] for protons in fat molecules. These two advancements raise the following questions:

1. How does error in the fat-water separation due to signal noise depend on the choice of echo times?

2. How does error caused by signal decay, which is neglected in the two-point Dixon model, depend on the choice of echo times?

3. Does the broken symmetry caused by the multi-peak nature of fat enable fat-water identification without phasor selection algorithms?

The first question is addressed in Chapter 4, “Error Due to Signal Noise.” There we examine the error in the water values themselves and in the relative background phasor, which is essential in identifying pixels as water-dominant or fat-dominant.[8] The error is quantified both analytically and by simulation as a function of signal noise magnitude, fat fraction, and both echo times. The results are confirmed by experiment using scans of a fat-water phantom.

The second question is addressed in Chapter 5, “Error Due to T_2* Decay.” The error is quantified as a function of the decay constant T_2* as well as both echo times. Theoretical results are obtained by simulation, and corresponding experimental results are obtained from scans of a fat-water phantom.

The third question is addressed in Chapter 6, “Fat-Water Determination without Phase Correction,” and is also approached by means of both simulation and experiment. Specifically, we quantify the reliability with which pixels can be identified as either water-dominant or fat-dominant as a function of signal noise magnitude and echo times.

The results that we present for these three projects can serve to guide doctors and technicians to choose scan parameters (specifically, the echo times) in order to balance the objectives of short scan time, small numerical error, and accurate water-fat identification. With carefully chosen echo times, higher quality images can be acquired using more reliable separation algorithms and faster scan times, resulting in improved diagnostic capabilities, reduced patient discomfort, and increased patient throughput.

Chapter 1

Foundations of MRI

1.1. Overview

This chapter is aimed at readers who are new to the subject of MRI, and it is intended to provide sufficient background information to enable the reader to understand how MR signals are generated and detected, how images are formed, and what the underlying principles are behind the most basic contrast mechanisms. In order to help the reader keep the big picture in mind, we present in this section a very brief summary of the entire image acquisition process. Then in the following sections, the details of each step are described more fully.

First, the sample to be studied (e.g., a patient) is placed in a static background magnetic field, B_0, which points in a direction that we take to be $\hat{z}$. The magnetic dipole moments in the sample—in particular, the hydrogen nuclei, to which we will refer simply as "spins"—tend to line up either parallel or antiparallel to the

background field. Slightly more of the spins line up parallel than antiparallel, resulting in a net magnetization, the magnitude of which varies with position in the sample according to spin density.

A radio-frequency (RF) field B_1 is then applied, exerting a torque on the spins and thereby tipping the magnetization vector away from the z direction. Once tipped, the magnetization vector precesses about $\hat{z}$ at a frequency that is proportional to the strength of the background field (the Larmor frequency). The precession of the magnetization results in a time-varying magnetic field in the vicinity of the sample. If a conducting coil is placed nearby, the changing magnetic flux through the coil generates an oscillating emf, the amplitude of which is proportional to the total number of spins in the sample. This emf is the MR signal from which images are generated.

To obtain enough information to form an image, the background magnetic field is varied spatially, thereby causing the spins in different locations to precess at different frequencies. Thus, the detected signal is a superposition of signals with different frequencies, and the location of the source of each component can be determined from the frequency. The actual data points that are collected constitute a matrix that is the spatial Fourier transform of the spin density within the sample. An inverse Fourier transform is applied to recover the image.[9]

1.2. Magnetization, Excitation, and Signal Detection

The MR signal depends entirely on the behavior of the magnetization in the sample, which in turn is determined by the fields B_0 and B_1. We therefore begin by considering the magnetization that results from placing a sample in a magnetic field B_0, after which we examine how an RF field B_1 causes this magnetization vector to tip and precess.

The magnitude of the magnetization, and hence that of the signal, is proportional to the difference between the fraction of the protons that are parallel (spin up) and the fraction that are anti-parallel (spin down) to the external field B_0. This difference, which we will call the net alignment fraction, can be calculated from the partition function for a proton in a magnetic field and is given by[10]

$$\left(\frac{n_+ - n_-}{N}\right) = tanh\left(\frac{\hbar\omega_0}{2kT}\right) \qquad \textit{Eq. 1.1}$$

where $\hbar$ is the reduced Planck's constant; k is Boltzmann's constant; T is temperature; and $\omega_0 = \gamma B_0$, with γ being the gyromagnetic ratio of a proton. For a free proton, $\gamma = 2.675 \times 10^8$ rad/s/T. In medical imaging, the protons of interest are usually the hydrogen nuclei in water molecules, for which the gyromagnetic ratio is almost exactly the same as that of a free proton;[9] we shall therefore ignore any difference between the two.

The equilibrium magnetization is then given by

$$M_0 = \frac{\rho\gamma\hbar}{2} tanh\left(\frac{\hbar\omega_0}{2kT}\right)$$

Eq. 1.2

The MR signal is proportional to this. In a typical clinical situation, with a B_0 value of 1.5 T and a patient composed mostly of water at body temperature, this corresponds to a net alignment fraction of about 3 out of a million protons with a magnetization of 0.003 A/m. At temperatures in the vicinity of room temperature and body temperature, these values change only very slightly with changes in temperature. In order to double the magnetization by reducing temperature, the patient would have to be cooled to about 153 K (–120° C), which would likely defeat the purpose of performing a diagnostic scan. Considering how small the net alignment fraction is, it is remarkable that a strong enough signal can be generated to produce a high quality image.

We now examine the tipping of the magnetization vector by an RF field B_1. We can understand this process classically in the following way. We consider the system from the point of view of a coordinate system that is rotating about the *z* axis of the lab frame at the Larmor frequency, which is the frequency at which proton spins precess about $\hat{z}$ and is given by $\omega_0 = \gamma B_0$. The coordinates in the rotating frame are given by

$$\hat{x}' = \hat{x}\, cos(\omega_0 t) - \hat{y}\, sin(\omega_0 t)$$
$$\hat{y}' = \hat{x}\, sin(\omega_0 t) + \hat{y}\, cos(\omega_0 t)$$

Eq. 1.3

We then simply apply (in the lab frame) an RF field $[\hat{x}\cos(\omega_0 t) - \hat{y}\sin(\omega_0 t)]B_1$, which is a circularly polarized plane wave. In the rotating frame, this corresponds to a constant magnetic field in the *x'* direction with magnitude B_1, which exerts a torque on the magnetization, rotating it down from the *z* axis. In the lab frame, the magnetization vector spirals downward, while in the rotating frame, it rotates directly down toward the *y'* axis, as shown in Figure 1.1. The magnitude and duration of the pulse can be chosen to rotate the magnetization by 90° so it ends up in the *x*-*y* plane and precesses (in the laboratory frame) with frequency ω_0.

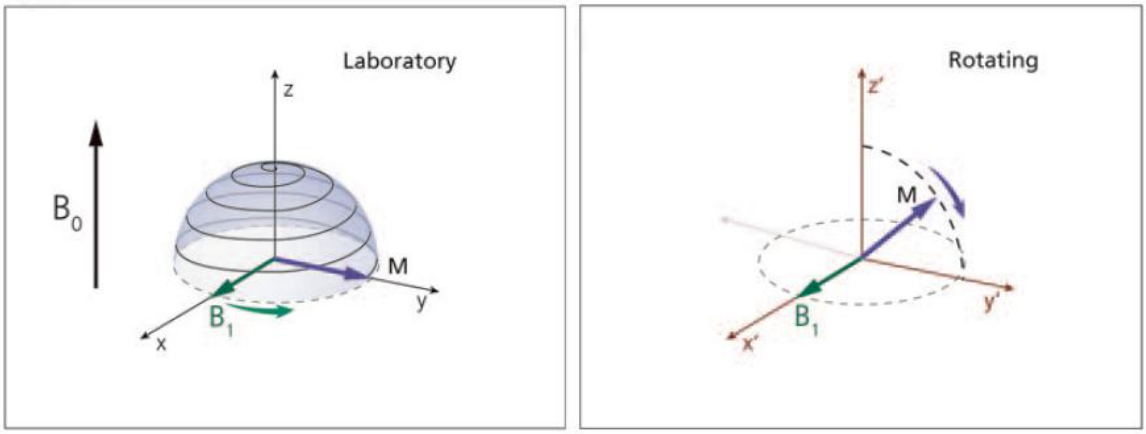

Figure 1.1. On the left is depicted the downward spiraling trajectory of the magnetization vector as seen from the lab frame. On the right is the direct downward rotation of the magnetization as seen from the rotating frame. (Reproduced from "Basic MRI Physics," by Aletras.[11])

The above process can be analyzed in the framework of quantum mechanics, in which case the initial state of an individual proton is taken to be spin up (aligned with B_0). As the RF field is applied, the proton's wave function evolves into a state for which the expectation value precesses in the transverse plane. For a large

number of protons, this yields the same net magnetization as that obtained classically.

Once the magnetization vector has been tipped into the transverse plane, it precesses as

$$\boldsymbol{M}(t) = M_0(sin(\omega_0 t)\,\hat{x} + cos(\omega_0 t)\,\hat{y}) \qquad \textit{Eq. 1.4}$$

This generates an emf in the receiver coil equal to

$$-\int \frac{d}{dt}(\boldsymbol{M} \cdot \boldsymbol{B}_r) d^3 r \qquad \textit{Eq. 1.5}$$

where $\boldsymbol{B}_r$ is the magnetic field that would be generated by the receiver coil if it were carrying one unit of current, and the integral is taken over the volume of the sample. Thus, the signal strength is essentially proportional to the time derivative of the precessing magnetization vector. Since the components of the magnetization oscillate at frequency ω_0, the derivative introduces an additional factor of ω_0, and the signal amplitude S satisfies the following proportionality relation:

$$S \propto \omega_0 \frac{\rho \gamma \hbar}{2} tanh\left(\frac{\hbar \omega_0}{2kT}\right) \qquad \textit{Eq. 1.6}$$

At reasonable temperatures (body or room temperature), the argument of the hyperbolic tangent function is small; furthermore, since relative magnitude is all we're interested in, we can ignore the constants and write

$$S \propto \frac{\rho \gamma^3 {B_0}^2}{T}$$

Eq. 1.7

Given that ρ, γ, and T are beyond our control, all we can do to improve signal strength is to use a stronger background field. The degree to which B_0 can be increased is limited by physiological and technological constraints. (In fact, γ can be controlled to some extent by imaging other particles besides hydrogen nuclei. However, the other types of particles that are present in the body and have nonzero spin are much less abundant than hydrogen, and in some cases the required frequency is inconvenient.)[9]

1.3. Image Formation

In the preceding discussion, the sample being studied has been assumed to be in a uniform background magnetic field B_0. In this case, when the RF pulse is applied to tip the spins into the transverse plane, the entire sample is excited. The resulting signal may be sufficient for performing spectroscopic measurements on the bulk of the sample; but since the signals from spins at different locations in the sample are all superposed into a single composite signal, it would seem that there is no way to form an image, even if multiple receivers are used. Specifically, the problem that must be solved in order to generate an image is to determine the positions within the sample from which the different components of the signal originate. In the following, we describe how this is accomplished by applying

magnetic field gradients in order to make the proton resonance frequency a function of position.

Although in practice one must take into account the decay of the signal and various other complicating factors, an understanding of the principles discussed thus far—namely, the magnetization vector, its precession, and the detection of the resulting signal—is a sufficient foundation for understanding how an image can be formed. We shall consider signal decay and other complicating factors later.

The first step in localizing the resonance signal is to limit the excitation of the sample to a single transverse plane corresponding to a fixed z value. This is accomplished by varying B_0 in the z direction, i.e., by applying a gradient so that the static field is now given by

$$B(z) = (B_0 + G_z z)\hat{z}$$

Eq. 1.8

where G_z is measured in mT/m and is typically on the order of 10 mT/m.[9] The resonance frequency of protons in the sample is now a function of position along the z direction. We can limit the excitation to a plane with z coordinate z_{slice} by choosing the frequency of the RF excitation pulse to be $\omega = \gamma(B_0 + G_z z_{slice})$. Immediately after the excitation pulse is applied, the gradient is removed; the background field is once again uniformly B_0, and the spins in the plane $z = z_{slice}$ emit a resonance signal while all other spins remain in their equilibrium state.

Localizing the resonance signal in the xy plane is a little more complicated, but it is based on the same principle and involves the application of gradients in the *x* and *y* directions. Suppose the slice we're considering has width L_x and height L_y. Before the *x* and *y* gradients are applied, every spin in the excited plane is precessing with frequency ω_0. The next step is to apply a gradient G_y in the *y* direction for a short time t_y. While this gradient is on, the magnetic field is a function of *y*, and the spins at different *y* positions precess at different frequencies. The spins at the positive end of the gradient get ahead in phase, while the spins at the negative end get behind. After the gradient is turned off, the spins all return to their normal precession rate ω_0, but they remain out of phase. Using $\rho(x, y)$ to represent the spin density as a function of position, the signal emitted by a volume element at (x, y) is now proportional to

$$\rho(x, y)e^{i(\omega_0 t+\gamma G_y t_y y)}$$

Eq. 1.9

Next, we turn on a gradient G_x in the *x* direction for time t_x. While this gradient is on, the phases of the spins change along the *x* direction just as they changed along the *y* direction when the gradient G_y was applied. The combined effect is a signal from the volume element at (x, y) proportional to

$$\rho(x, y)e^{i(\omega_0 t+\gamma G_y t_y y+\gamma G_x t_x x)}$$

Eq. 1.10

which can be rewritten as

$$\rho(x,y)e^{i\omega_0 t}e^{i(\gamma G_x t_x x+\gamma G_y t_y y)}$$

Eq. 1.11

The receiver coil detects the sum of the signals from tissue at all locations, which is given by

$$\iint dxdy\ \rho(x,y)e^{i\omega_0 t}e^{i(\gamma G_x t_x x+\gamma G_y t_y y)}$$

Eq. 1.12

Note that this can be thought of as

$$\left(\iint dxdy\ \rho(x,y)e^{i(\gamma G_x t_x x+\gamma G_y t_y y)}\right)e^{i\omega_0 t}$$

Eq. 1.13

so that all of the information of interest, namely the magnitude and phase of the signal, is contained in the quantity in parentheses. This quantity turns out to be the spatial Fourier transform of $\rho(x,y)$. That is, if we let $k_x = \gamma G_x t_x$ and $k_y = \gamma G_y t_y$, then the signal that we measure at time t_x is

$$\iint dxdy\ \rho(x,y)e^{i(k_x x+k_y y)}$$

Eq. 1.14

Different values of t_x and t_y are chosen carefully with the repeated application of gradients of suitable strengths until the signal has been sampled for all points (k_x, k_y) in a discrete k-space matrix. The final image is obtained by taking the inverse Fourier transform of this matrix.

In fact, separate gradients do not need to be applied for each point in k-space. The receiver coil is "on" at all times (i.e., we can record the signal picked up by the coil at any time), so that once a *y* gradient has been applied to achieve a given value of k_y, we need only turn the *x* gradient on and then record the detected signal at equally spaced times $t_x = \frac{2\pi n}{\gamma G_x L_x}$, where n runs from 0 to $N_x - 1$, with N_x being the number of pixels in the *x* direction. This way, we can fill in a whole horizontal line of k-space in the time that it takes for t_x to go from zero to $\frac{2\pi(N_x-1)}{\gamma G_x L_x}$.

For simplicity, the scheme described above assumes nonnegative k_x and k_y values and acquires a matrix in the first quadrant of k-space. In practice, negative gradients are applied to sample points in k-space with negative k_x and k_y values, and the matrix that is obtained is centered on the origin of k-space, with k_x ranging from $-\frac{\pi N_x}{L_x}$ to $\frac{\pi(N_x-2)}{L_x}$. Figure 1.2 shows a simplified "pulse sequence diagram" (neglecting slew rate and other details) illustrating the timing of the RF pulse, the three gradients, and the sampling of the signal.

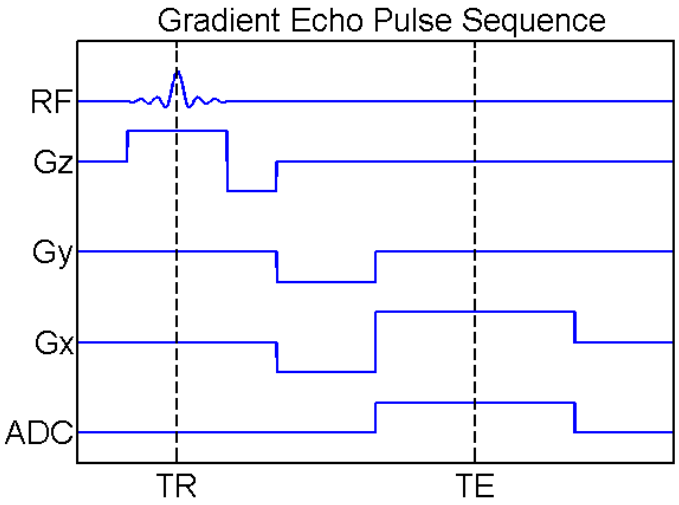

Figure 1.2. A gradient echo pulse sequence diagram. The RF pulse (top) is applied at time TR while the z gradient is turned on to excite a specific slice. A negative y gradient is turned on to move down to the lowest row in k-space. Simultaneously, a negative x gradient is turned on to move to the left-most position in k-space. Then a positive x gradient, called the readout gradient, is turned on to traverse one complete line in k-space. While the readout gradient is on, the amplitude and phase of the signal are sampled and stored by electronics (designated "ADC" here) at regular intervals along that line in k-space. The time at which the center of a line is sampled is called the echo time, TE. The entire sequence is repeated with different y gradients in order to sample different lines in k-space. (Adapted from Haacke.[9])

After one line is acquired, we repeat the sequence using a different *y* gradient in order to acquire a different line in k-space. To cover all of k-space, the process must be carried out for N_y different values of $k_y = \gamma G_y t_y = \frac{2\pi n}{L_y}$. When we're done, we'll have an $N_x \times N_y$ matrix for each slice. For fairly obvious reasons, the gradients are given the following names: G_z is called the "slice select gradient" because it is used to ensure that only spins in a particular slice are excited; G_y is called the "phase encode gradient" because it is used to encode *y* position of spins by changing their

phase as a function of y position; and G_x is called the "readout gradient" because an entire line in k-space is sampled while G_x is on.

The sequence of RF signals and gradients that are applied during an MRI scan is called a "pulse sequence." In a traditional pulse sequence, the sample might be re-excited with a new RF pulse for each line in k-space. Denoting the time between excitations as T_R (for "repetition time"), the total scan time for multiple slices is roughly

$$T_{scan} = N_z N_y T_R \qquad \textit{Eq. 1.15}$$

where N_z is the number of slices. The time required to sample one line in k-space is typically much shorter than T_R, and therefore the x-direction or "read direction" is generally chosen to correspond to the larger of the two dimensions of the image matrix (if the matrix is not square). Scan time can be shortened significantly by acquiring multiple lines between successive excitations, i.e., within one T_R.

In the scheme just described, when the center of a line in k-space is sampled, the spins are momentarily in phase (along the readout direction) and the signal magnitude reaches a maximum. This is called an echo, and in this context, since it is brought about by the application of a field gradient, it is called a "gradient echo." Such pulse sequences are called gradient echo sequences (or GRE, for "gradient-recalled echo"). In general, there is one echo per line in k-space, and the time at which the signal maximum occurs is called the echo time (*TE*).

It should be noted that the slice selection step is optional. Alternatively, a 3D volume can be excited, after which phase encoding gradients in the z and y directions are applied for times t_z and t_y, and then a readout gradient in the x direction is applied. In this way, a 3D array of points in k-space can be sampled, and the image is recovered by taking the inverse 3D Fourier transform of the data set. In the context of MRI, this is what is meant by "3D imaging."

1.4. Relaxation and Contrast

So far we have assumed a signal with constant amplitude that is proportional to spin density. In fact, the signals from different tissue types decay at different rates, and the relaxation to equilibrium (longitudinal) magnetization also occurs at different rates. Thus, different tissues that have the same spin density might in fact generate significantly different signals and therefore have different intensity in the resulting image. In this way, the relaxation and decay mechanisms make possible different ways to generate contrast among tissue types.

1.4.1. T_1: Spin-Lattice Relaxation

The first time constant of interest is the one that determines how quickly the sample returns to its equilibrium state. Note that after the RF pulse has been applied and the magnetization vector is precessing, the system is not in equilibrium. Within a given time interval, each precessing spin has some probability of exchanging energy with the surrounding structure and returning to a spin up or spin down state. That probability depends on the nature of the surrounding material (the

tissue type) and determines the time constant with which the magnetization exponentially approaches its equilibrium value. Because this process involves the statistical relaxation to an equilibrium state and comes about via energy exchange between the spins and the surrounding structure, it is called spin-lattice relaxation. The longitudinal magnetization regrows according to the equation

$$M_z(t) = M_0\left(1 - e^{-t/T_1}\right)$$

Eq. 1.16

The relaxation time T_1 is significant for the following reason. Due to signal decay (see the following sections for further decay mechanisms), a complete image generally cannot be acquired after a single excitation. Thus, repeated excitations are necessary. However, if the magnetization does not fully relax back to its equilibrium value before the second excitation, the magnitude of the precessing magnetization vector after the second excitation will be smaller than the magnitude after the first. In other words, the signal will be weaker. In this way, T_1 limits the rate at which we can repeatedly excite the sample to obtain successive lines in k-space.

In practice, because T_1 is typically on the order of about a second, time constraints require that the repeated excitations be carried out before the longitudinal magnetization has fully recovered. Tissues with shorter T_1 values recover faster and end up producing stronger signals than tissues with longer T_1 values. The time interval between repeated excitations is called the "repetition time" and is denoted *TR*. Using a longer *TR* value allows all of the different tissue types to return to their equilibrium magnetization between successive excitations and

results in a stronger signal. This also results in a longer total scan time. If a short *TR* value is used, tissues with short T_1 are still able to recover most of their equilibrium magnetization while tissues with longer T_1 are not. In this case, tissue with short T_1 will appear brighter than tissue with long T_1. Such images are called T_1-weighted. Additionally, shorter *TR* allows for a shorter scan time. Typical *TR* values range from a few milliseconds to about a second.

1.4.2. T_2: Spin-Spin Relaxation

It is tempting to assume that the rate at which the transverse magnetization decays is the same as the rate at which the longitudinal magnetization grows—i.e., that the relaxation of spins to their equilibrium state accounts for the decay of the transverse magnetization. Although it is true that each spin that returns to the spin up state results in a reduction of the transverse magnetization, the overall decay of the transverse magnetization is dominated by other processes and generally occurs much faster than T_1 relaxation.

Recall that the magnetization vector is actually a sum of a large number of magnetic dipoles. It retains its magnitude only to the extent that all of the dipoles precess exactly in phase. Under perfect conditions—i.e., in the presence of a perfectly uniform, static background field—all of the precessing dipoles would remain exactly in phase, and the signal would decay due to relaxation alone. However, due to random thermal motion on a microscopic scale of all the particles in the sample, which themselves have charge and spin, the actual field in the sample fluctuates non-uniformly. As a result, the precessing spins experience varying fields

and their orientation undergoes a random walk akin to Brownian motion. Thus, they are no longer perfectly aligned, having been dephased randomly. This effect is termed spin-spin relaxation because it involves the interaction of the spins with the magnetic fields of surrounding spins. Such random dephasing results in exponential decay, the time constant for which is denoted T_2. After a single excitation, the remaining transverse magnetization is given by

$$M_{\perp}(t) = M_0 e^{-t/T_2}$$

Eq. 1.17

To get as strong a signal as possible, the signal should be sampled immediately after excitation, as close to $t = 0$ as possible. The time after excitation at which the signal is acquired is called the echo time and is denoted *TE*. If a short *TE* value is used, very little decay occurs and signals from all tissues are near their initial maximum values. Thus, the difference in T_2 for different tissues will have no effect on their relative brightness in the image. However, if a longer *TE* value is used—specifically, long enough for tissues with short T_2 values to decay significantly but short enough that tissues with long T_2 values do not decay much—then tissues with short T_2 values will appear dark while those with long T_2 values will appear bright. This is a T_2-weighted image. Some anatomical features of interest will be more visible on a T_2-weighted image than on a T_1-weighted image.

Combining the previous two equations, the signal at time *TE* after excitation (when repeated excitations are used) is given by

$$S(TR, TE) = M_0\left(1 - e^{-TR/T_1}\right)e^{-TE/T_2}$$

Eq. 1.18

In summary, a strong signal (i.e., a bright image) that is weighted by neither T_1 nor T_2 but shows only spin density is obtained by using long *TR* (in order to allow the longitudinal magnetization to recover fully before tipping it again) with short *TE* (to sample the signal immediately after excitation, before it has time to decay). To obtain a T_1-weighted image, a short *TR* value is used (so that some tissues have time to recover but others don't) with a short *TE* value (so there is minimal decay and no T_2 weighting). In order to obtain a T_2-weighted image, a long *TR* value is used with long *TE*. If a short *TR* were used with a long *TE*, the result would be a faint image with mixed T_1 and T_2 dependence; this is usually not desirable.[9]

1.4.3. T_2*: Dispersion Due to Intravoxel Field Inhomogeneity

The dephasing effect described above is a result of time-varying fluctuations of the magnetic field inside the sample on a microscopic scale. Even apart from thermal fluctuations, there is still static field inhomogeneity due to the internal structure and chemical properties of the sample. Different molecules distort the magnetic field around themselves in different ways. These inhomogeneities result in further dephasing in addition to that described above. This effect, combined with T_2 decay, results in a net decay with a time constant that is denoted T_2* ("tee two star").

There is a significant difference between these two types of dephasing, however. Dephasing to due static inhomogeneities can be reversed if the spins can

be reflected across a line in the transverse plane. Indeed, this is achieved by applying a 180° RF pulse. Spins that were spreading out begin to get closer together again after the reflection. Such a pulse is typically applied at time $TE/2$ so that at time TE, the spins have maximally rephased, with a net decay due only to T_2 rather than T_2^*. The signal spike that occurs at the time of maximal rephasing is called a "spin echo," and the acquisition of an image in this manner is called spin echo imaging. Traditionally, one spin echo is generated for each line in k-space. In gradient echo imaging, it is T_2^* that determines the signal strength, while in spin echo imaging it is T_2 alone. Spin echo imaging allows longer TE values to be used with less signal loss, resulting in higher quality images.[9]

1.4.4. Contrast Mechanisms in MRI

The numerical values acquired in an MRI scan are only known to be *proportional* to the spin density; the numbers themselves do not correspond directly to any precise physical property of the tissue such as density. Compared to other modalities such as CT or PET, in which real physical properties (e.g., attenuation coefficient or fractional uptake of a radionuclide) are directly measured, MRI would appear to be an inferior modality. However, due to the contrast mechanisms discussed above and many others, including chemical shift, temperature, magnetic susceptibility, and diffusion, MRI can provide a vast amount of quantitative information and sensitive contrast that are not possible with other modalities. A major theme in current MRI research is the refinement of quantitative contrast via these different mechanisms.[12]

Chapter 2

Fat-Water Separation and the Dixon Technique

2.1. The Significance of Fat-Water Separation

The ability to suppress or separate the signal from fat in an MR image is often critical in clinical applications. There are two main reasons for this.[2] First, the signal from fat is usually very strong and tends to overpower the signal from other tissue types, making it difficult to spot important anatomical features that do not contain fat (such as a cancerous lesion). In such situations, suppressing or subtracting out the fat component can greatly enhance the diagnostic utility of an image. Figure 2.1 shows an example[3] of a breast image with different degrees of fat suppression or subtraction. In the bottom left frame, the subtraction of the fat signal and the presence of a contrast agent have made the presence of a cancerous tumor (indicated by the white arrow) significantly more apparent.

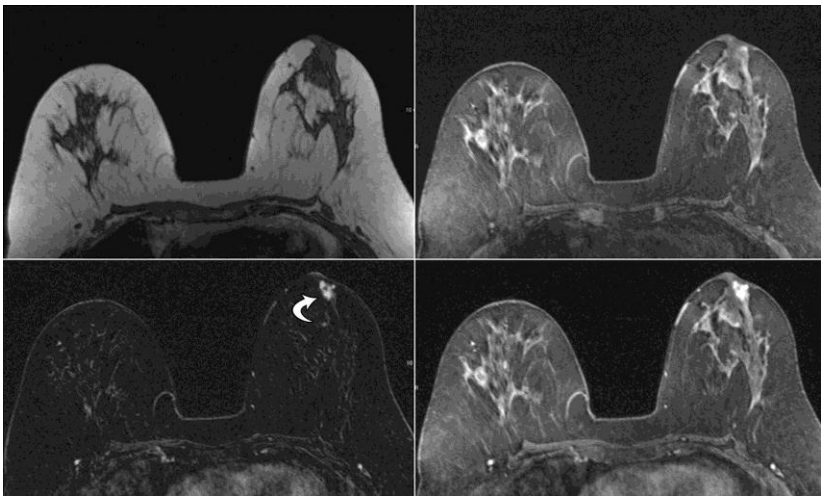

Figure 2.1. 55-year-old woman with newly diagnosed recurrent ductal carcinoma in situ in the right breast. MRI was performed before surgery. Clockwise from top left: Axial T_1-weighted unenhanced, axial T_1-weighted fat-saturated, axial T_1-weighted fat-saturated contrast-enhanced, and axial T_1-weighted contrast-enhanced with subtraction images show clumped enhancement in the superficial subareolar region and a subtle focus of hypoenhancement (arrow) in the center that is best appreciated on subtraction. (Reproduced from "Variable Appearances of Fat Necrosis on Breast MRI," by Daly et al.[3])

Second, once an unknown tissue mass has been detected, the nature of the mass must be determined—specifically, whether or not it is cancerous. Separating an image into fat and non-fat ("water") enables the identification of fatty masses such as benign lipomas. An example[4] of a cardiac MRI exam in which a suspicious mass can be seen is shown in Figure 2.2. Resolution of the image into fat and water components reveals the mass to be a lipoma (fatty deposit).

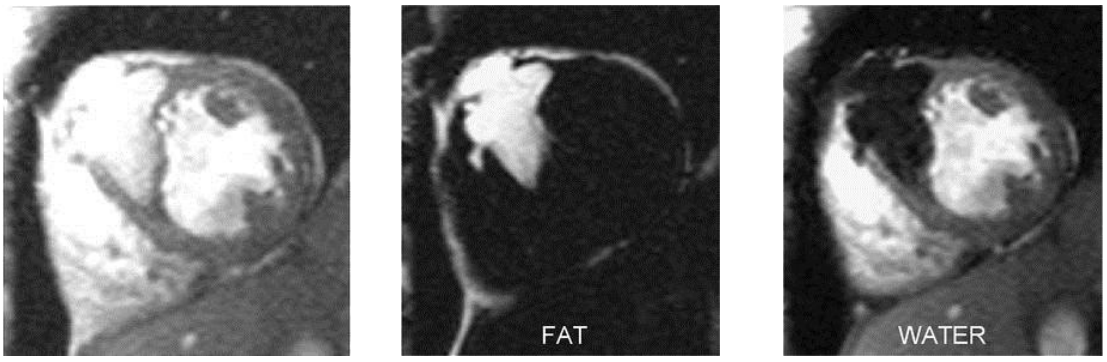

Figure 2.2. The image on the far left is a cardiac scan in which a suspicious mass can be seen in the middle. After fat-water separation, the mass was identified as a benign lipoma (non-cancerous fatty tumor). (Reproduced from "Myocardial Fat Imaging," by Kellman et al.[4])

In addition to the above reasons, fat-water separation techniques have also been the focus of much research over the past decade due to the increasing prevalence of obesity, diabetes, fatty liver disease, and other conditions to which the identification and quantification of fat is clinically relevant.[13] Currently, there are three main methods of fat suppression, each of which has various advantages and disadvantages in different applications.[2] These methods include short-tau inversion recovery (STIR),[14] fat saturation,[15,16] and the Dixon technique[1,8] (which is sometimes also called opposed-phase imaging or chemical shift imaging).

STIR takes advantage of the fact that fat has a shorter T_1 value than water. In this method, a 180° pulse is applied at the beginning of the sequence, turning the tissue magnetization anti-parallel to the background field. Since fat and water relax at different rates, at the instant when the magnetization of fat becomes zero, the magnetization of water still has a non-zero component anti-parallel to the field. A

90° excitation pulse is applied at precisely this moment, tipping the magnetization vector of water into the transverse plane and thereby generating a resonance signal from water only. Thus, fat will not show up in the final image.

This method has several disadvantages, however. First, tissues with T_1 values similar to that of fat will also be suppressed. Second, it is difficult to use contrast agents effectively in conjunction with STIR since contrast agents work by shortening T_1 values. Third, different types of fat and deposits of fat in different tissue types have different T_1 values and will not be suppressed uniformly. Furthermore, since the excitation pulse is applied before the tissue has fully relaxed, there is significant signal loss, resulting in low SNR.[2]

The method of fat saturation involves first exciting fat tissue only by applying an RF pulse at precisely the resonance frequency of fat. The resulting transverse magnetization is then dephased ("spoiled") by the application of a magnetic field gradient. When a standard pulse sequence is then applied, only protons in water have longitudinal magnetization available to be tipped into the transverse plane to produce a signal. A pure water image can then be obtained. This method is very unreliable, however, because the saturation pulse must have a very precise frequency and must be perfectly uniform. Small errors and non-uniformities in both the background field and the RF field can result in not only incomplete fat suppression but regions in which the water signal is nulled.[2]

We focus here on techniques that have evolved from the method first proposed by W. T. Dixon in 1984.[1] Such methods are referred to as "Dixon imaging,"

"Dixon techniques," or "Dixon methods." Unlike STIR and fat saturation, Dixon techniques are independent of relaxation rates, immune to field inhomogeneity, and compatible with contrast agents. Dixon pulse sequences are also quite fast, resulting in less patient discomfort and fewer motion artifacts.[2] The main disadvantage of Dixon techniques is the requirement of complex phase correction algorithms to identify pixels as either fat-dominant or water-dominant. When these algorithms fail, fat and water values can be swapped in the separated images.[8] The bulk of the work presented in this thesis is aimed at minimizing such errors in fat-water separation using the Dixon technique.

2.2. The Traditional Dixon Technique

Dixon methods rely on the well-established fact that protons in fat molecules have a slightly different resonance frequency compared to protons in water. The vast majority of protons in the human body are in either water molecules or fat molecules, so we conveniently divide the entire body into only two tissue categories: water and fat. Protons in fat are partly shielded from the external magnetic field by the electrons in the fat molecule such that the effective field experienced by a fat proton is about 3.35 ppm smaller than that experienced by a water proton.[9] Since a particle's nuclear resonance frequency is proportional to the magnitude of the field into which the particle is placed, this means that a fat proton's resonance frequency is lower than that of a water proton by 3.35 ppm. This is called the "chemical shift" of fat.

When a volume of tissue is excited by an RF pulse, all of the protons initially resonate in phase. Because of the slight difference in precession frequency between fat and water protons, however, the signals from fat and water gradually acquire a relative phase as time passes. The net signal from the tissue volume can then be expressed as[8]

$$S(t) = \left(W + e^{i\gamma\sigma B_0 t}F\right)p \qquad \textit{Eq. 2.1}$$

where W is the amount of water, F is the amount of fat, γ is the Larmor frequency, σ is the chemical shift of –3.35 ppm, B_0 is the static magnetic field, and $p = e^{i\varphi}$ is a background phasor that is dependent on position and arises from the magnetic field inhomogeneity that exists due to the electromagnetic properties of the tissue.

The complex coefficient $e^{i\gamma\sigma B_0 t}$ is the phase of the fat signal relative to water as a function of time; for brevity, we shall denote it by the letter b. We control the value of this relative phase by selecting the time at which the signal is measured (the echo time, *TE*). At a field strength of 1.5 T, b has a period of 4.6 ms. Thus, if we acquire images at echo times of 0 ms and 2.3 ms, we get one image in which water and fat are in phase ($b = 1$) and another image in which they are exactly out of phase ($b = -1$). The two signals acquired in this way from a single voxel in the sample are given by:

$$\begin{aligned} S_1 &= (W + F)p_1 \\ S_2 &= (W - F)p_2 \end{aligned} \qquad \textit{Eq. 2.2}$$

The background phasors p_1 and p_2 are unknown, so we eliminate them by taking the absolute value of both equations. This then introduces some ambiguity into the problem because $|W - F| = W - F$ if W is greater than F, but $|W - F| = F - W$ if W is less than F. The equations are then

$$|S_1| = W + F$$

$$|S_2| = \begin{cases} W - F, & W > F \\ F - W, & W < F \end{cases}$$

Eq. 2.3

By adding or subtracting these two equations, we get two possible sets of solutions for W and F:

$$W = \frac{1}{2}(|S_1| + |S_2|) \text{ and } F = \frac{1}{2}(|S_1| - |S_2|)$$
$$W = \frac{1}{2}(|S_1| - |S_2|) \text{ and } F = \frac{1}{2}(|S_1| + |S_2|)$$

Eq. 2.4

Put another way, for each voxel we can define the dominant component as $A = \frac{1}{2}(|S_1| + |S_2|)$ and the subordinate component as $B = \frac{1}{2}(|S_1| - |S_2|)$. All that remains to be determined is whether the pixel is fat-dominant or water-dominant.

One way to proceed is to plug the two possible solutions back into the signal equations and solve for the phasors p_1 and p_2. One then has pairs of possible phasors for each pixel in the image. Physically, we expect the tissue properties that give rise to the field inhomogeneity to vary continuously; therefore, the relative phase $p_{rel} = p_2/p_1$ should also be continuous. Seed pixels which are known to be either pure

water or pure fat (as determined by anatomical information in the image) can then be chosen, and regions can be grown around these seeds, whereby for each neighboring pixel the phasor value is chosen that results in a smoother relative phase map.[17]

Alternatively, the problem can be formulated as a global optimization problem.[18,19] In either case, a significant amount of effort must go into phase selection, and various approaches have been explored over the past two decades. Choosing the incorrect phasor value for a given pixel results in a swapping of the water value with the fat value for that pixel. Figure 2.3 shows an example in which all of the pixel values in one region (the far left) have been swapped due to inaccurate echo time calibration. Figure 2.4 shows the correctly separated images with no swapping.

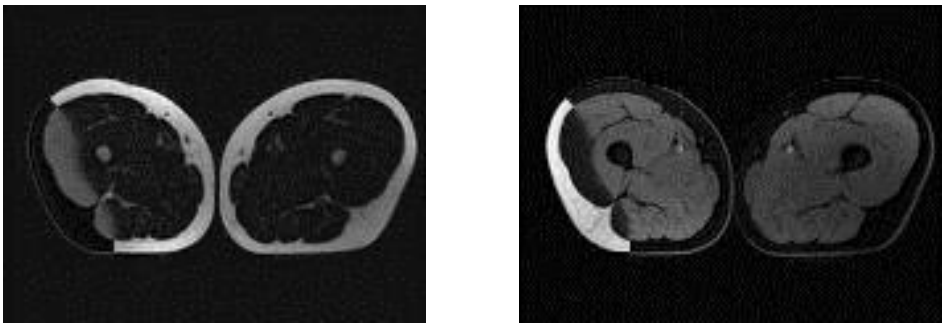

Figure 2.3. Separated fat (left) and water (right) images from a leg scan. Pixels have been swapped between the two images in a region on the far left. In this case, the swapping was caused by inaccurate echo time calibration; however, swapping can also occur due to other factors such as noise, inaccuracies in the model, and failure of the phasor selection algorithm.

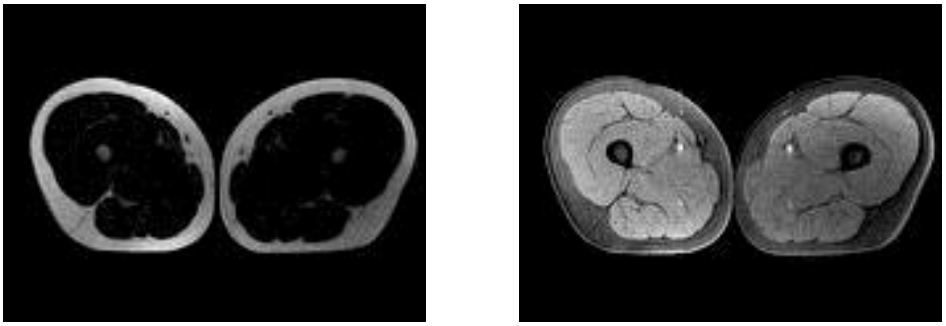

Figure 2.4. Separated fat (left) and water (right) images from the same leg scan with correct echo time values.

Several variations on Dixon's original method have been implemented, including single-point[20-22] and three-point[23] methods. The number of "points" refers to the number of images that are acquired at different echo times. In single-point methods, the echo time is chosen so that the relative phase between fat and water is 90°. The real component of the signal is assumed to be water, and the imaginary component is assumed to be fat. The single-point method is faster (since only one image needs to be acquired), but it requires highly favorable conditions that are difficult to achieve in practice (namely, a uniform background phase).[8]

In three-point methods, the extra information available in a third image makes it possible to calculate the relative background phase or incorporate signal decay into the model, thereby achieving more accurate fat and water values.[23,24] However, the phase can still be swapped for rapidly varying phase maps. Moreover, this technique takes more time since a third image must be acquired. For these reasons, the two-point Dixon method is still the most widely used and will be the focus of our investigation.[8]

2.3. The Two-Point Dixon Technique with Flexible Echo Times

In 2011, Holger Eggers and Johan Berglund independently published techniques for two-point Dixon imaging with arbitrary echo times,[5,6] further extending the partially flexible method previously demonstrated by Xiang.[25] In principle, this makes it possible to reduce scan times significantly since echo times much shorter than the traditional opposed-phase (2.3 ms) and in-phase (4.6 ms) times can be used. With flexible echo times, the signal equations become

$$S_1 = (W + b_1 F)p_1$$
$$S_2 = (W + b_2 F)p_2$$

Eq. 2.5

where b_1 and b_2 are no longer restricted to ±1 but can now take on complex values. Both Berglund and Eggers eliminate the background phasors by taking the square of the modulus of the two equations, yielding

$$|S_1|^2 = W^2 + 2b_{1R}FW + |b_1|^2F^2$$
$$|S_2|^2 = W^2 + 2b_{2R}FW + |b_2|^2F^2$$

Eq. 2.6

where b_{1R} and b_{2R} represent the real parts of b_1 and b_2. The problem is then a matter of solving this system of equations and determining by phase selection which solution is correct for each voxel. In the following, we present Berglund's and Eggers' methods with some slight modifications.

2.3.1. Berglund's Method

Berglund solves these equations indirectly by first defining the variable $Q = F/(F + W)$, or "fat fraction," thereby reducing the system to a single quadratic equation in Q. This equation yields two possible values for Q which correspond to the two possible solutions for W and F described in the previous section. With knowledge of Q, we can determine the two possible values for the relative background phasor p_{rel} without knowing W and F. Solving for Q yields

$$Q = \frac{c_1 \pm \sqrt{c_3}}{c_1 + c_2}$$

Eq. 2.7

where, using subscripts R and I to represent real and imaginary parts, respectively,

$$c_1 = |S_1|^2(1 - b_{2R}) - |S_2|^2(1 - b_{1R})$$

$$c_2 = |S_1|^2(|b_2|^2 - b_{2R}) - |S_2|^2(|b_1|^2 - b_{1R})$$

$$c_3 = |S_1|^2|S_2|^2|b_1 - b_2|^2 - (b_{1I}|S_2|^2 - b_{2I}|S_1|^2)^2$$

Eq. 2.8

The two values for Q yield two possible values for the relative background phasor, which are given by

$$p_{rel} = \frac{S_2[1 + (b_1 - 1)Q]}{S_1[1 + (b_2 - 1)Q]}$$

Eq. 2.9

As in the traditional two-point Dixon method, the requirement that p_{rel} be smooth can be used to select the correct value of p_{rel}. Then the phasors p_1 and p_2 for each voxel can be determined as follows:

$$p_1 = \exp\left\{i \cdot \text{angle}\left[\frac{S_1(1-b_2) - S_2(1-b_1)/p_{rel}}{b_1 - b_2}\right]\right\}$$

$$p_2 = p_1 \cdot p_{rel}$$

Eq. 2.10

Once the phasors are known, the correct values of *W* and *F* can be found directly from the signal equations. However, Berglund recommends first smoothing the phase map and then solving the following over-determined system of linear equations for *W* and *F*:

$$\begin{bmatrix} Re(S_1/p_1) \\ Im(S_1/p_1) \\ Re(S_2/p_2) \\ Im(S_2/p_2) \end{bmatrix} = \begin{bmatrix} 1 & Re(b_1) \\ 0 & Im(b_1) \\ 1 & Re(b_2) \\ 0 & Im(b_2) \end{bmatrix} \begin{bmatrix} W \\ F \end{bmatrix}$$

Eq. 2.11

The least-squares solution is found by multiplying the vector on the left-hand side by the Moore-Penrose pseudoinverse of the matrix on the right-hand side. Using the smoothed phase in this way removes some noise from the image in a way that is physically motivated.[5]

2.3.2. Eggers' Method

Eggers' approach is to solve the modulus-squared signal equations directly for *W* and *F*. He then calculates the phasors that correspond to each possible solution and applies a selection algorithm just as Berglund does. At this point, his results are identical to Berglund's. After smoothing the relative background phasor, however, he presents a slightly different method for re-estimating *W* and *F*.

Solving first for *F* yields

$$F = \pm\sqrt{-\frac{c_2}{2c_1} \pm \sqrt{\left(\frac{c_2}{2c_1}\right)^2 - \frac{c_3}{c_1}}}$$

Eq. 2.12

The constants c_1, c_2, and c_3, which are different from those in the previous section, are given by

$$c_1 = 4(b_{2\mathrm{R}} - b_{1\mathrm{R}}) \cdot (|b_1|^2 b_{2\mathrm{R}} - |b_2|^2 b_{1\mathrm{R}}) + (|b_2|^2 - |b_1|^2)^2$$

$$c_2 = -4(b_{2\mathrm{R}} - b_{1\mathrm{R}}) \cdot (|S_1|^2 b_{2\mathrm{R}} - |S_2|^2 b_{1\mathrm{R}}) + 2(|b_2|^2 - |b_1|^2) \cdot (|S_1|^2 - |S_2|^2)$$

$$c_3 = (|S_1|^2 - |S_2|^2)^2$$

Eq. 2.13

Plugging these values for *F* back into the (squared) first signal equation and solving for *W*, we get

$$W = -b_{1R}F \pm \sqrt{|S_1|^2 - (b_{1I}F)^2}$$

Eq. 2.14

Each value for *F* thus yields two values for *W*; the correct value is the one that also satisfies the second signal equation.

Typically, four distinct solutions exist, but only two are non-negative. In Eggers' original work,[6] the negative *F* values are discarded from the beginning. However, we note that because of the effects of noise, the negative solutions could actually be correct and should therefore not be discarded. For example, the signal from a pure water voxel, which should have a fat value of exactly zero, may yield a slightly negative fat value due to noise. To account for such circumstances, we propose retaining only the two solution pairs (*W*,*F*) for which $W + F > 0$. (By symmetry, there can only be two such pairs.)

Once the two possible solution pairs (*W*,*F*) are known, the corresponding background phasors p_{rel} can be calculated. In Eggers' scheme, they are given by

$$p_{rel} = \frac{S_1^* S_2}{(W + b_1^* F)(W + b_2 F)}$$

Eq. 2.15

where the * indicates the complex conjugate operation.

Once again, the smoothness criterion is used to select the correct phasor value for each voxel. When the correct phasor has been selected, the corresponding (*W*,*F*) values are known for that voxel and the problem is completely solved.

However, Eggers also recommends smoothing p_{rel} and re-estimating W and F in the following way.

First we absorb the background phasor p_1 into the water and fat variables to get $W' = Wp_1$ and $F' = Fp_1$. Then the signal equations become, in matrix form,

$$\begin{bmatrix} S_1 \\ S_2/p_{rel} \end{bmatrix} = \begin{bmatrix} 1 & b_1 \\ 1 & b_2 \end{bmatrix} \begin{bmatrix} W' \\ F' \end{bmatrix}$$

Eq. 2.16

This is easily solved for W' and F', after which the real W and F values can be determined by taking the absolute value. The disadvantage of this method is that the sign of W and F is forced to be positive. We will show in a later section that allowing W and F to be negative is crucial for identifying voxels as water-dominant or fat-dominant without applying a phasor selection algorithm.

2.4. The Multi-Peak Fat Model

Traditional Dixon methods assume that fat protons have a single resonance frequency 3.35 ppm less than that of water. In fact, due to the complex structure of the typical fat molecule (a triglyceride), fat has several different resonance frequencies. This is because the degree of shielding experienced by an individual hydrogen nucleus within a fat molecule depends on, for example, whether it is at the end of the molecule or whether it is next to a carbon-carbon double bond. As shown in Figure 2.5, recent experiments have identified at least ten distinct peaks in the

spectrum of fat, corresponding to hydrogen nuclei located at positions labeled A through J in the diagram.[7]

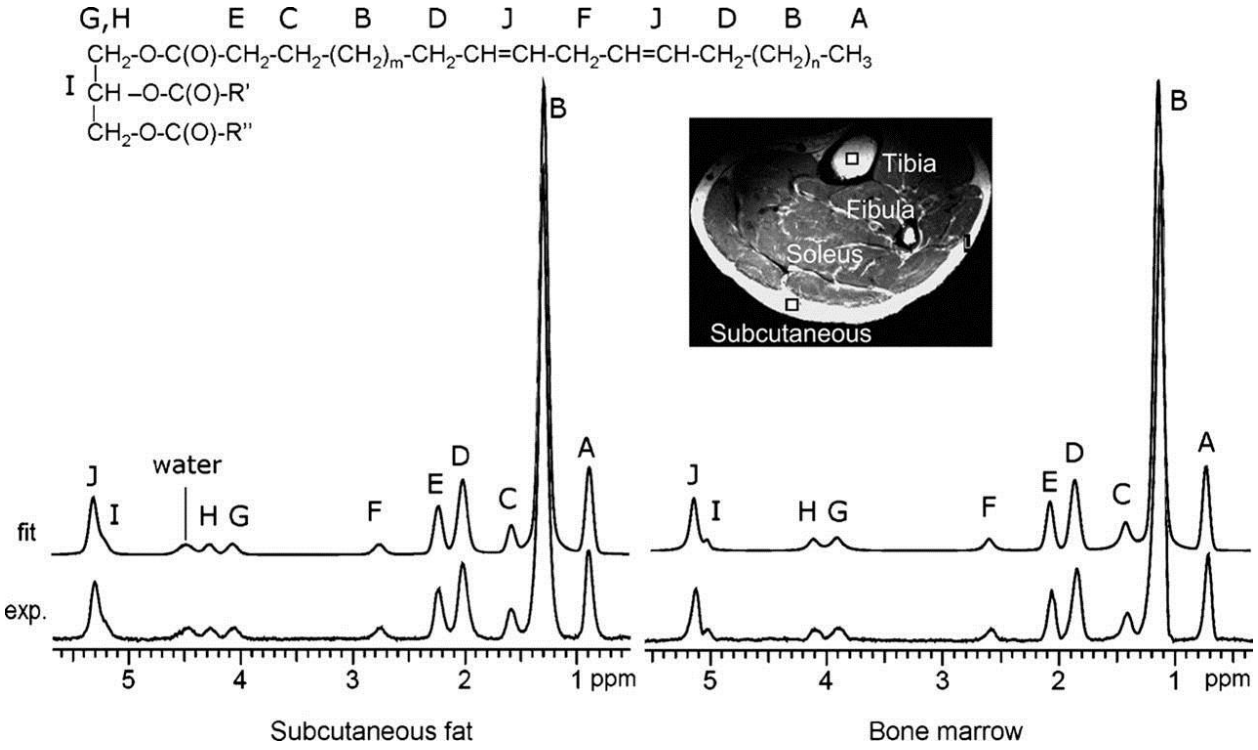

Figure 2.5. The spectra of subcutaneous fat and bone marrow as measured by Ren et al. at 7 T in vivo*. The letters labeling the peaks indicate the locations within the fat molecule, as shown at the top, of the hydrogen nuclei that generate the corresponding peak. (Reproduced from "Composition of Adipose Tissue and Marrow Fat in Humans by 1H NMR at 7 Tesla," by Ren et al.[7])*

For the multi-peak fat model used throughout this work, we have taken the resonance frequency and peak area values for positions A, B, C, D, E, F, and J, for a seven-peak model. Thus, in the signal equation, the coefficient in front of F is no longer the phasor $e^{i\gamma\sigma B_0 t}$, but a sum of phasors, weighted by the sizes of the corresponding spectral peaks. As a result, the fat coefficient b (as defined previously) becomes

$$b = \sum_{k=1}^{7} A_k e^{i\omega_k t}$$

Eq. 2.17

where $\omega_k = \gamma\sigma_k B_0$ is the angular frequency, relative to water, of a proton in position k, and A_k is the normalized area under the k^{th} spectral peak. For the values of A_k and σ_k in our model, we have taken the average of the values measured for subcutaneous fat and bone marrow fat, as presented in Table 1.

Table 1

Spectral Peaks of Fat		
k	σ_k (ppm)	A_k
1	-3.60	0.0847
2	-3.20	0.6257
3	-2.91	0.0707
4	-2.47	0.0952
5	-2.25	0.0662
6	-1.73	0.0158
7	0.81	0.0418

The multi-peak model has been shown to yield more accurate fat-water separation than the single peak model.[6] Its applicability depends on the assumption that the relative abundances of the seven different "types" of hydrogen atoms are constant for all fat in all patients. If the relative abundances were not known *a priori*, two image acquisitions would not be sufficient to separate water and fat; one acquisition for each fat peak plus another acquisition for water would be needed. Experiment shows, however, that the assumption of constant relative abundances is valid, and the above model produces results that match direct measurements of

both the amplitude and phase of the fat signal as a function of echo time in different patients.[26]

Chapter 3

A Generalized Solution with a Geometric Interpretation

In this chapter, we generalize the solutions presented by Berglund[5] and Eggers[6] to allow for independent dispersion or decay rates of two chemical species denoted *W* and *F* (though in this context the species are not necessarily water and fat) and we present a geometric interpretation of the problem, which will be a useful tool for analyzing the effects of noise and identifying water and fat without phase correction.

3.1. The Generalized Problem

To generalize the problem for two chemical species with independent dispersion and decay rates, we rewrite the signal equations as

$$S_1 = (a_1 W + b_1 F)p_1$$
$$S_2 = (a_2 W + b_2 F)p_2$$

Eq. 3.1

The coefficients a_n and b_n can be arbitrary complex numbers, so this formulation allows for multi-peak natures and independent decay rates of both species. Taking the square of the modulus of both signal equations, we now get

$$|S_1|^2 = |a_1|^2 W^2 + 2(a_{1R} b_{1R} + a_{1I} b_{1I})FW + |b_1|^2 F^2$$
$$|S_2|^2 = |a_2|^2 W^2 + 2(a_{2R} b_{2R} + a_{2I} b_{2I})FW + |b_2|^2 F^2$$

Eq. 3.2

where the subscripts *R* and *I* denote the real part and imaginary part, respectively. In the following two sections, we show how both Berglund's and Eggers' solutions are altered by this generalization.

3.2. Generalization of Berglund's Solution

The generalized version of Berglund's solution takes the same form as before:

$$Q = \frac{c_1 \pm \sqrt{c_3}}{c_1 + c_2}$$

Eq. 3.3

However, the constants c_1, c_2, and c_3 must be redefined as follows.

$$c_1 = |S_1|^2[|a_2|^2 - Re(a_2^* b_2)] - |S_2|^2[|a_1|^2 - Re(a_1^* b_1)]$$
$$c_2 = |S_1|^2[|b_2|^2 - Re(a_2^* b_2)] - |S_2|^2[|b_1|^2 - Re(a_1^* b_1)]$$
$$c_3 = |a_1 a_2 S_1 S_2|^2 \left|\frac{b_1}{a_1} - \frac{b_2}{a_2}\right|^2 - [|S_2|^2 Im(a_1^* b_1) - |S_1|^2 Im(a_2^* b_2)]^2$$

Eq. 3.4

The formulas for the relative background phasor p_{rel} and phasors p_1 and p_2 then become

$$p_{rel} = \frac{S_2[a_1 + (b_1 - a_1)Q]}{S_1[a_2 + (b_2 - a_2)Q]}$$

$$p_1 = \exp\left\{i \cdot \text{angle}\left[\frac{S_1(a_2 - a_1 b_2) - S_2(a_1 - a_2 b_1)/p_{rel}}{a_2 b_1 - a_1 b_2}\right]\right\}$$

$$p_2 = p_1 \cdot p_{rel}$$

Eq. 3.5

and the generalized version of the least-squares matrix equation becomes

$$\begin{bmatrix} Re(S_1/p_1) \\ Im(S_1/p_1) \\ Re(S_2/p_2) \\ Im(S_2/p_2) \end{bmatrix} = \begin{bmatrix} Re(a_1) & Re(b_1) \\ Im(a_1) & Im(b_1) \\ Re(a_2) & Re(b_2) \\ Im(a_2) & Im(b_2) \end{bmatrix} \begin{bmatrix} W \\ F \end{bmatrix}$$

Eq. 3.6

which is again solved using the Moore-Penrose pseudoinverse. In all of these equations, when the constants a_1 and a_2 are replaced by 1, Berglund's original solutions are recovered.

As was mentioned previously, once the fat fraction Q has been found using Berglund's method, the W and F values can then be calculated without first

calculating the phasors. From the definition of fat fraction, the solution pair (*W*,*F*) must satisfy $F = \left(\frac{Q}{1-Q}\right) W$. Substituting this expression into the squared signal equations, we obtain the following expressions for *F* and *W*.

$$F = \pm\sqrt{\frac{|S_1|^2 Q^2}{|a_1|^2(1-Q)^2 + 2(a_{1\mathrm{R}}b_{1\mathrm{R}} + a_{1\mathrm{I}}b_{1\mathrm{I}})Q(1-Q) + |b_1|^2 Q^2}}$$

$$W = \pm\sqrt{\frac{|S_1|^2 (1-Q)^2}{|a_1|^2(1-Q)^2 + 2(a_{1R}b_{1R} + a_{1I}b_{1I})Q(1-Q) + |b_1|^2 Q^2}}$$

Eq. 3.7

Again, negative solutions must be taken into account, and the two solutions that are retained should be those for which $W + F > 0$.

3.3. Generalization of Eggers' solution

In the generalized version of Eggers' solution, the possible fat values also take the same form as before:

$$F = \pm\sqrt{-\frac{c_2}{2c_1} \pm \sqrt{\frac{{c_2}^2}{4{c_1}^2} - \frac{c_3}{c_1}}}$$

Eq. 3.8

The constants c_1, c_2, and c_3 become

$$c_1 = 4(|a_1|^2\beta_2 - |a_2|^2\beta_1) \cdot (|b_1|^2\beta_2 - |b_2|^2\beta_1) + (|a_1 b_2|^2 - |a_2 b_1|^2)^2$$

$$c_2 = -4(|a_1|^2\beta_2 - |a_2|^2\beta_1) \cdot (|S_1|^2\beta_2 - |S_2|^2\beta_1) + 2(|a_1 b_2|^2 - |a_2 b_1|^2) \cdot (|S_1 a_2|^2 - |S_2 a_1|^2)$$

$$c_3 = (|S_1 a_2|^2 - |S_2 a_1|^2)^2$$

Eq. 3.9

where $\beta_1 = a_{1R} b_{1R} + a_{1I} b_{1I}$ and $\beta_2 = a_{2R} b_{2R} + a_{2I} b_{2I}$.

The new *W* values are

$$W = -\frac{(a_{R1} b_{1R} + a_{1I} b_{1I})}{|a_1|^2} F \pm \frac{\sqrt{|a_1|^2 |S_1|^2 + [(a_{R1} b_{1R} + a_{1I} b_{1I})^2 - |a_1|^2 |b_1|^2] F^2}}{|a_1|^2}$$

Eq. 3.10

As before, only those values that also satisfy the second signal equation should be retained, and of the four solutions, the two that satisfy $W + F > 0$ should be kept.

The relative phasor p_{rel} is then given by

$$p_{rel} = \frac{S_1^* S_2}{(a_1^* W + b_1^* F)(a_2 W + b_2 F)}$$

Eq. 3.11

Traditional phasor selection and smoothing algorithms can still be applied, and the *W* and *F* values can be re-estimated using the smoothed phasor map. The matrix equation to be solved becomes

$$\begin{bmatrix} S_1 \\ S_2 / p_{rel} \end{bmatrix} = \begin{bmatrix} a_1 & b_1 \\ a_2 & b_2 \end{bmatrix} \begin{bmatrix} W' \\ F' \end{bmatrix}$$

Eq. 3.12

As with the generalization of Berglund's method, all of the above equations reduce to the previous versions when a_1 and a_2 are replaced by 1.

3.4. A Geometric Interpretation

Significant insight into the two-point Dixon problem can be gained by considering the signal equations from a geometric perspective. In this section, we present a geometric interpretation that will aid our analysis in later sections when we consider the effects of signal noise and the identification of fat and water without phasor selection algorithms.

Recall that all of the results described thus far are derived from the square of the modulus of the signal:

$$|S|^2 = |a|^2 W^2 + 2(a_R b_R + a_I b_I) FW + |b|^2 F^2 \qquad \textit{Eq. 3.13}$$

The value of S is what we physically measure, while the values of a and b are calculated as functions of echo time according to our signal model for the chemical species under consideration. For water, $a = 1$, and for fat, b is the weighted sum of phasors given by the multi-peak model. Thus, the only unknown variables in this equation are W and F.

In the W-F plane, Equation 3.13 represents an ellipse centered at the origin. The geometric properties of the ellipse, namely the orientation, eccentricity, and scale, are determined by the values of S, a, and b. Since these values depend on the time at which the signal is sampled (echo time TE), the ellipse can be considered to be evolving in time. According to the model being used, any water-fat combination (W,F) that lies on this ellipse would give rise to a signal of magnitude $|S|$ and is

therefore a potential solution. In the two-point Dixon problem, the signal is sampled at two different echo times, so we are in essence taking two snapshots of this evolving ellipse at different times—i.e., we end up with two ellipses. The solution (*W*,*F*) that we ultimately seek is an intersection point of these two ellipses, as shown in Figure 3.1.

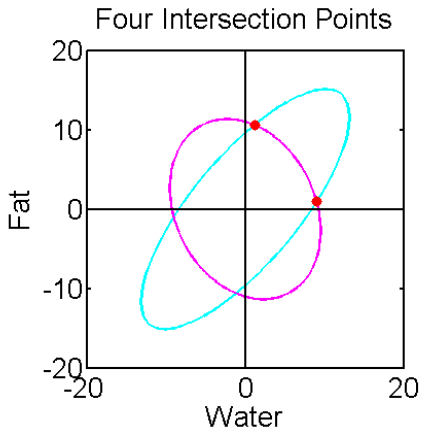

Figure 3.1. Two ellipses corresponding to two signals measured at different times. In this case, there are four intersection points. We expect the correct solution to be non-negative, so we consider only the two solutions that are in the first quadrant.

There are three cases to be considered. In the most common case, the ellipses will have four intersection points as in Figure 3.1. Usually, two of those intersection points will be in the first quadrant, which contains all physically allowable solutions (since *W* and *F* must be non-negative). The existence of these two non-negative solutions is the ambiguity that must be resolved using phasor selection algorithms.

In the second case, the ellipses will touch at exactly two points. Statistically, this is unlikely ever to occur exactly, but we consider the possibility for completeness. In this case, there is only one physical solution since by symmetry

one of the two solutions must be negative. This happens when $W = F$ for the single-peak fat model and when W is close to F for the multi-peak fat model. This case is shown in Figure 3.2.

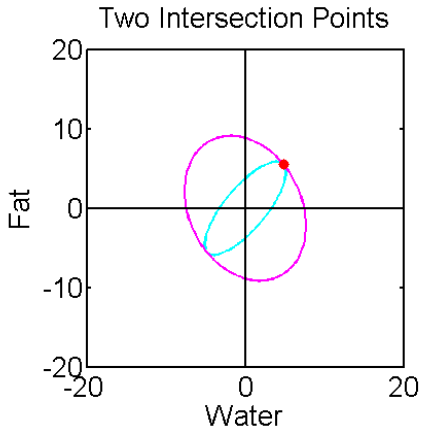

Figure 3.2. In extremely rare cases, the two ellipses might just barely touch at only two points rather than four. When this happens, only one of the solutions will be in the first quadrant, and we can discard the other.

In the third case, the ellipses do not touch at all, as shown in Figure 3.3. This can only happen due to noise in the signal or to some inaccuracy in our model. When this occurs, we may choose as our solution a point between the two ellipses, near the midpoint of the line segment that joins the ellipses at their closest approach. To do this, we find the intersection points of the line $F = \left(\frac{Re(Q)}{1-Re(Q)}\right) W$ with the two ellipses and then calculate their midpoint.

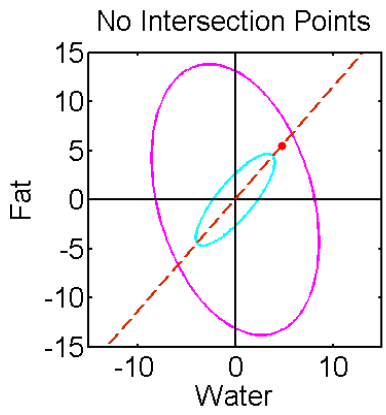

Figure 3.3. Due to noise or inaccuracies in our model, we may encounter situations in which the two ellipses do not intersect. We then choose as our solution a point between the ellipses where they come closest to touching.

There is actually a fourth possibility: the ellipses may coincide at every point. However, this will only happen if $TE_1 = TE_2$ (and if there is no signal noise), and we will never choose our echo times this way. Due to the constraints of the problem, there are no cases in which the ellipses intersect at exactly one or exactly three points.

The locations of the solutions (W,F), the degree of ambiguity, and noise performance all depend to some extent on the orientations, eccentricities, and sizes of these ellipses. We therefore examine the dependence of these properties on S, a, and b, and hence on the echo time. To describe the orientation of the ellipse, we define the ellipse's "tilt angle" ψ as the angle between the semimajor axis and the positive W axis, as shown in Figure 3.4.

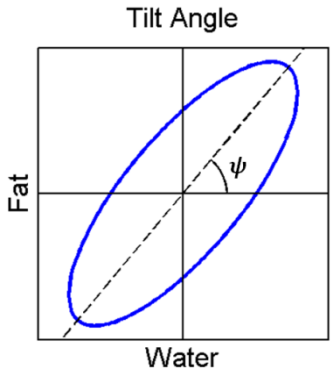

Figure 3.4. We define tilt angle ψ to be the angle between the major axis of the ellipse and the positive W axis.

In terms of c, ψ is given by the formula

$$\psi = 90° + \frac{1}{2} cot^{-1}\left(\frac{|a|^2 - |b|^2}{2(a_R b_R + a_I b_I)}\right)$$

Eq. 3.14

For the case of water and fat, $a = 1$, and this simplifies to

$$\psi = 90° + \frac{1}{2} cot^{-1}\left(\frac{1 - |b|^2}{2b_R}\right)$$

Eq. 3.15

When the single-peak fat model is used, it simplifies even further to

$$\psi = 90° + 45° \times \text{sign}(b_R)$$

Eq. 3.16

Figure 3.5 shows the tilt angle as a function of time for $B_0 = 1.5$ T for both the single-peak model and the multi-peak fat model.

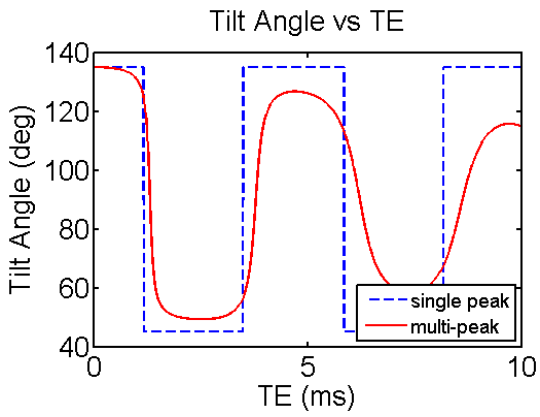

Figure 3.5. Tilt angle as a function of time at B_0 = 1.5 T for the single-peak model (blue dashed line) and the multi-peak model (red solid line).

The most important consequence of the dependence of tilt angle on echo time is that for any model in which both water and fat have only one resonance peak and have the same decay rate, the argument of the inverse cotangent function is zero ($|a|^2 - |b|^2 = 0$). Thus, the tilt angle will always be either 45° or 135°. In either case, both ellipses will be symmetric across the line $F = W$, and if (A,B) is a solution then (B,A) is the other possible solution. Note also that the tilt angle depends only on a and b, which depend on TE_1 and TE_2 (and on what model we are using). This means that noise in the signal will not affect the tilt angle.

The second characteristic of interest is the eccentricity of the ellipse, which is given by

$$e = \sqrt{1 - \frac{|a|^2 + |b|^2 - \sqrt{(|a|^2 - |b|^2)^2 + 4(a_R b_R + a_I b_I)^2}}{|a|^2 + |b|^2 + \sqrt{(|a|^2 - |b|^2)^2 + 4(a_R b_R + a_I b_I)^2}}}$$

Eq. 3.17

The important thing to note here is that the eccentricity, like the tilt angle, only depends on a and b. Therefore, signal noise does not affect the eccentricity of the ellipse either. For fat and water, this formula simplifies to

$$e = \sqrt{\frac{2\sqrt{1 - |b|^2 + 4b_R^2}}{1 + |b|^2 + \sqrt{1 - |b|^2 + 4b_R^2}}}$$

Eq. 3.18

In the single-peak fat model, letting θ represent the phase of the complex coefficient b, this simplifies even further to

$$e = \sqrt{\frac{2|cos\,\theta|}{1 + |cos\,\theta|}}$$

Eq. 3.19

Figure 3.6 shows eccentricity as a function of time for both single- and multi-peak models at $B_0 = 1.5$ T.

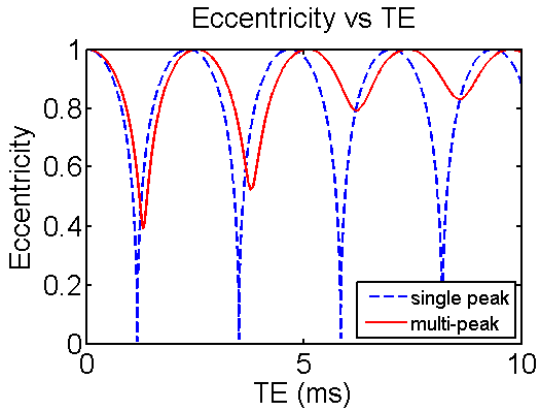

Figure 3.6. Eccentricity as a function of time for both single- and multi-peak models at B_0 = 1.5 T.

The third characteristic of interest is the scale of the ellipse, which is associated with the size of the semimajor and semiminor axes. They are given by

$$R_{major} = |S| \sqrt{\frac{2}{|a|^2 + |b|^2 - \sqrt{(|a|^2 - |b|^2)^2 + 4(a_R b_R + a_I b_I)^2}}}$$

$$R_{minor} = |S| \sqrt{\frac{2}{|a|^2 + |b|^2 + \sqrt{(|a|^2 - |b|^2)^2 + 4(a_R b_R + a_I b_I)^2}}}$$

Eq. 3.20

For water and fat, these formulas simplify to

$$R_{major} = |S| \sqrt{\frac{2}{1 + |b|^2 - \sqrt{(1 - |b|^2)^2 + 4b_R^2}}}$$

$$R_{minor} = |S| \sqrt{\frac{2}{1 + |b|^2 + \sqrt{(1 - |b|^2)^2 + 4b_R^2}}}$$

Eq. 3.21

Both axes are proportional to the magnitude of the signal. Thus, signal noise will affect the scale of the ellipse, and this is in fact the only effect that noise has. Noise that makes the magnitude of the signal smaller will shrink the ellipse, and noise that makes the signal larger will expand the ellipse. Figure 3.7 shows the effect of noise on an ellipse at a given echo time.

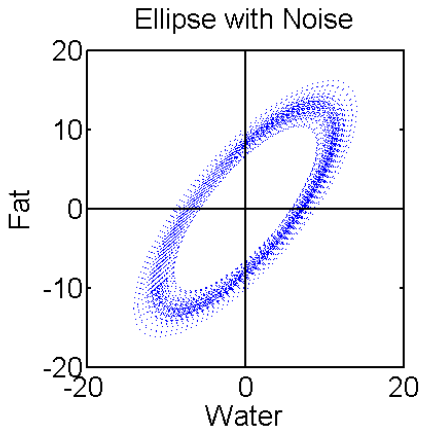

Figure 3.7. Noise of SNR = 10. The tilt angle and eccentricity are unaffected. Only the scale of the ellipse is affected.

In the following chapters, we will refer frequently to this geometric interpretation of the two-point Dixon problem to aid our understanding of the effects of noise and the resolution of the ambiguity of solutions. In closing, we note that this model could be generalized to separate *n* chemical species. To do so, we would need to acquire images at *n* different echo times and find the intersection points of *n n*-dimensional hyper-ellipsoids. The formulas would be significantly more complicated, but once derived, their implementation would be quite practical with the aid of computers.

Chapter 4

Error Due to Signal Noise

Given the ability to choose arbitrary echo times and the desire to acquire images as quickly as possible (with the ultimate goal being to acquire dynamic, movie-like sequences), we would like to choose the shortest possible echo times that will still yield accurate fat-water separation. It is therefore important to investigate noise performance as a function of the echo times TE_1 and TE_2 in order to determine what values would be ideal for dynamic imaging applications. In particular, we address the following three questions.

For given TE_1 and TE_2 values at a given noise level (in the signal),

1. What will be the resulting error in the calculated water and fat values in the separated images?

2. What will be the resulting error in the calculated relative background phasor (which is used to determine whether each pixel is water-dominant or fat-dominant)?

3. What will be the magnitude of the difference between the two possible background phasor values, and how does that difference compare to the magnitude of the error in the two values?

Noise performance as a function of echo times has been explored previously by simulation for water values in the single-peak model.[5,6] We extend these investigations to include the multi-peak behavior of fat and to find the error in both the fat value and the background phasor as well. Furthermore, we present a comparison of analytically calculated error values with simulation and experiment. The results will aid in selecting echo times that will yield smaller error in the water and fat values and more accurate identification of voxels as water-dominant or fat-dominant.

4.1. Signal Noise in the Geometric Interpretation

Before presenting any quantitative results, we first discuss the noise performance qualitatively in the context of our geometric interpretation of the two-point Dixon problem. Visualizing the ellipses that correspond to the two signal equations helps one to develop an intuitive feel for how noise performance depends on the echo times. This is best illustrated by considering an example.

Figure 4.1 shows two possible ellipse configurations for arbitrarily chosen values of $W = 3$ and $F = 7$. In the first configuration, the echo times are 0.50 ms and 2.35 ms, and in the second the echo times are 1.18 ms and 3.50 ms. Without noise, the correct solutions ($W = 3$ and $F = 7$) are easily recovered in both cases. When noise is added to the signals, however, the ellipses will be rescaled slightly by an unknown amount. One can see that in the first configuration, a slight alteration in the scale of the ellipses will change the solutions by only a small amount; but in the second configuration, a small rescaling of the ellipses might change the solutions dramatically.

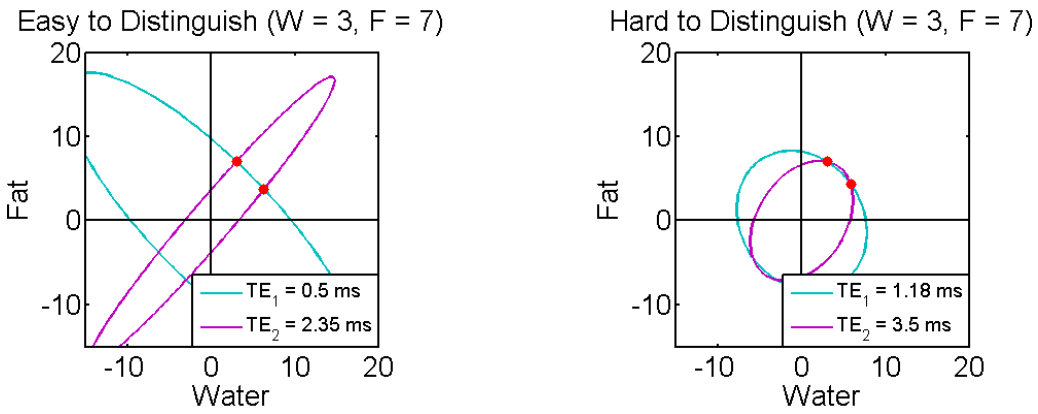

Figure 4.1. Intersecting ellipses corresponding to the signal equations for true values of water and fat of 3 and 7, respectively. The ellipses in the plot on the left correspond to echo times of 0.50 ms and 2.35 ms. Note that the crossings are near-perpendicular and that a slight change in the scale of either ellipse would have a small effect on the locations of the two solutions. In the plot on the right, the echo times are 1.18 ms and 3.50 ms. In this case, the ellipses cross at very shallow angles; as a result, a slight change in the scale of either ellipse is likely to change the locations of the solutions dramatically.

Figure 4.2 shows the same configurations with noise added ($SNR = 20$). The solutions obtained on the left have changed very little compared to those in Figure

4.1 and are still reasonably accurate. However, the solutions obtained on the right cover almost the full range of possible fat fractions from $Q = 0$ to $Q = 1$. Thus, for these echo times, little useful information can be recovered at this noise level, and we conclude that the echo time combination of 1.18 ms and 3.50 ms should be avoided.

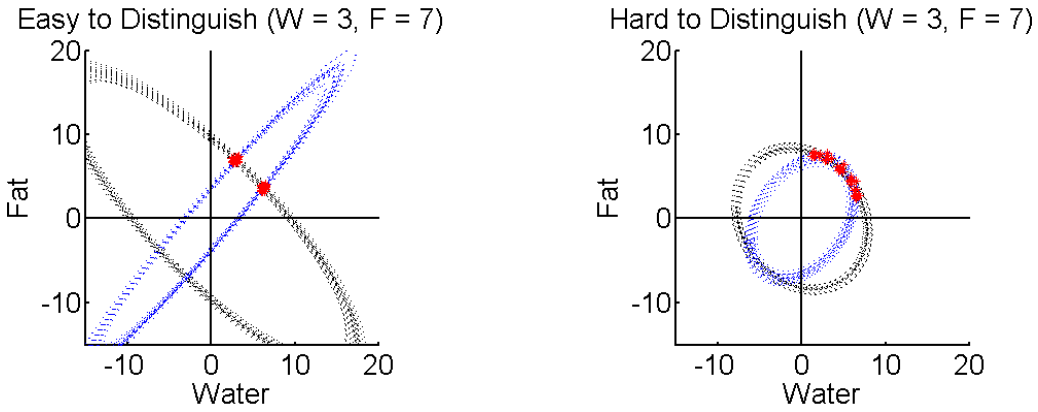

Figure 4.2. The same plots as in the previous figure, but with Gaussian noise added to the corresponding signals in order to show how the solutions are affected. Note that in the plot on the left, for echo times of 0.50 ms and 2.35 ms, the solutions change very little; in the plot on the right, for echo times of 1.18 ms and 3.50 ms, the possible solutions spread out significantly.

This example makes it clear that noise performance depends on the relative orientation and eccentricity of the ellipses. As a general rule, better noise performance will be obtained when the ellipses are tilted in opposite directions and when they have relatively high eccentricities. In order to facilitate the choice of appropriate echo times, it is therefore worthwhile to examine the behavior of tilt angle and eccentricity as functions of echo time as determined by Eq. 3.14 and Eq. 3.17.

For the traditional single-peak model, both tilt angle and eccentricity exhibit simple behavior. Figure 4.3 again shows tilt angle and eccentricity as functions of time (blue dashed line for the single-peak model), for *TE* up to 10 ms at $B_0 = 1.5$ T. Both functions have the same periodicity as the phase of fat, with a period of 4.6 ms. The tilt angle alternates between 135° and 45°, with the transition occurring when the fat phase (the phase angle of b) is an odd multiple of 90°, at which time the ellipse becomes a circle and the change in orientation corresponds to the swapping of major and minor axes. The eccentricity of the ellipse approaches 1 when the fat-water phase is a multiple of 180°, at which point the ellipse becomes a pair of parallel lines given by $F = -W \pm |S|$ or $F = W \pm |S|$.

Neglecting signal decay and dispersion due to multiple resonances, this cycle will continue forever. Since optimal noise performance is achieved with oppositely oriented ellipses with high eccentricity, we can predict from this that the best performance will be achieved if the echo times are chosen such that the fat phase is an odd multiple of 180° at one echo time and an even multiple of 180° at the other echo time. This is consistent with previously published results regarding noise performance for the single-peak model.[6]

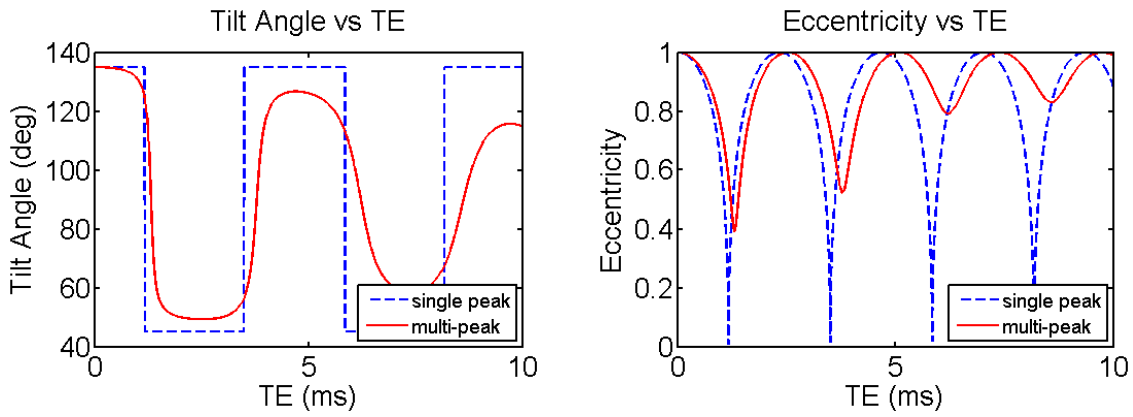

Figure 4.3. Tilt angle (left) and eccentricity (right) as functions of echo time for single-peak (blue dashed line) and multi-peak (red solid line) fat models.

When a multi-peak fat model is used, the behavior will change slightly. The red solid lines in Figure 4.3 show the tilt angle and eccentricity for the multi-peak model. There are a few important differences compared to the single-peak model. First, the period becomes slightly longer, close to 5.1 ms as opposed to 4.6 ms. Second, the tilt angle becomes a continuous function of time, and as the multiple peaks of fat disperse, it never quite reaches 45° or 135° for $TE > 0$. Similarly, the eccentricity never returns to zero, which means that the ellipses never become circular. Despite these differences, the overall trends are the same as in the single-peak model, and from this we expect the best noise performance to be achievable with echo times corresponding to the same relative fat-water phases as in the single-peak model, with the only important difference being that the period has changed from 4.6 ms to 5.1 ms at 1.5 T.

4.2. The Effect of Noise on Water and Fat Values

In this section, we present an analysis of the error in the calculated water and fat values due to signal noise, and we compare analytically calculated results with simulation and experiment. We are most interested in error as a function of echo times, and we focus primarily on the pure water and pure fat cases since most voxels in human tissue tend to be either fat or water. Mixtures do occur, however, and we also consider error as a function of fat fraction.

4.2.1. Analytical Calculation

To calculate error analytically, we first note that at each echo time, the signal has both real and imaginary parts, and the noise is Gaussian with the same standard deviation in both parts. Letting σ_S represent the standard deviation of the signal noise in one channel, the resulting standard deviation in the calculated water value, σ_W, can then be expected to be given by

$$\sigma_W = \sqrt{\left|\frac{\partial W}{\partial S_{1R}}\right|^2 + \left|\frac{\partial W}{\partial S_{1I}}\right|^2 + \left|\frac{\partial W}{\partial S_{2R}}\right|^2 + \left|\frac{\partial W}{\partial S_{2I}}\right|^2}\,\sigma_S \qquad \textit{Eq. 4.1}$$

where S_1 and S_2 are the signals at the two echo times and W is the calculated value of water (or fat, if we replace W with F) in the voxel of interest as given by the generalized solution to the two-point Dixon problem using either of Eggers' or Berglund's approaches. In all of the following, as a way of checking our own work and verifying that the two approaches are indeed equivalent, all calculations and

simulations were carried out using both approaches. No differences were found. The evaluation of the above expression is rather tedious, and even with multiple variable substitutions the final expression is far from compact. Details are provided in Appendix A.

The echo times of interest for a two-point Dixon scan are on the order of a few milliseconds. To investigate error dependence on echo times, we evaluated Eq. 4.1 for every possible combination of echo times between 0 ms and 8 ms, with the only restriction being $TE_2 > TE_1$. In actual dual echo scans, the second echo time must be at least about 1 ms greater that TE_1 because this is about how much time it takes to sample a line in k-space, and the sampling of the first echo must be completed before the sampling of the second echo is begun.

Figure 4.4 shows the percent error in the water value for pure water voxels ($Q = 0$). The plot on the left is for the single-peak fat model, and the plot on the right for the multi-peak model. The main difference between the two is that the multi-peak nature of fat breaks the periodicity in TE_2. The conclusions based on our geometric interpretation of the problem, namely that error is minimized if one echo time corresponds to when fat and water are in phase and the other echo time to when they are opposed in phase, are confirmed. For the single-peak model, this means that one echo time should be an odd multiple of 2.3 ms and the other should be an even multiple of 2.3 ms (for B_0 = 1.5 T). For the multi-peak model, these times are changed to even and odd multiples of approximately 2.5 ms.

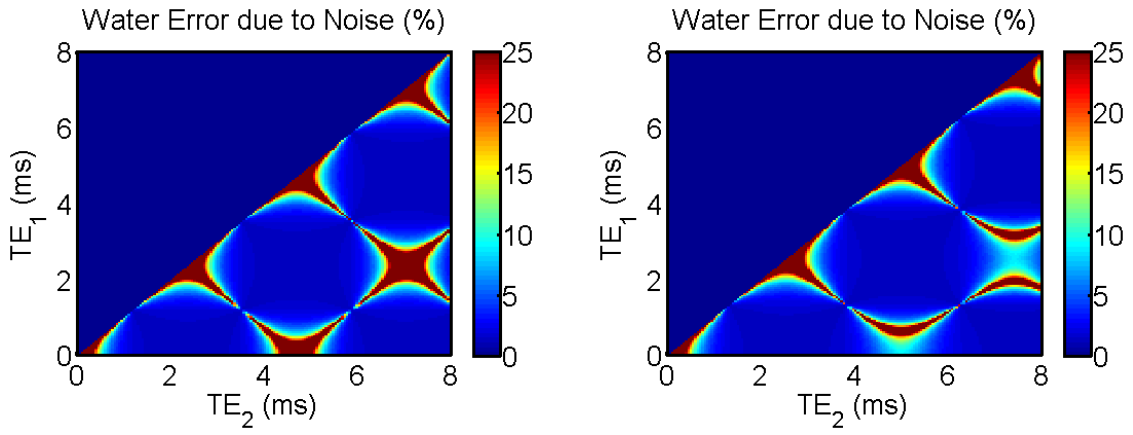

Figure 4.4. Percent error in W due to signal noise. The plot on the left is for the single-peak model, while the plot on the right is for the multi-peak model. In both cases, an SNR of 50 was assumed, with a background field of 1.5 T and a fat fraction of 0.

Figure 4.5 shows the percent error in the fat value for pure fat voxels ($Q = 1$). For the single-peak model, the results for fat are exactly the same as those for water. For the multi-peak model, the results are similar to those for water but with different symmetry. The major differences occur in regions where the error is high. The minimal error is still achieved at the same echo times, specifically one odd multiple and one even multiple of about 2.5 ms for the multi-peak model.

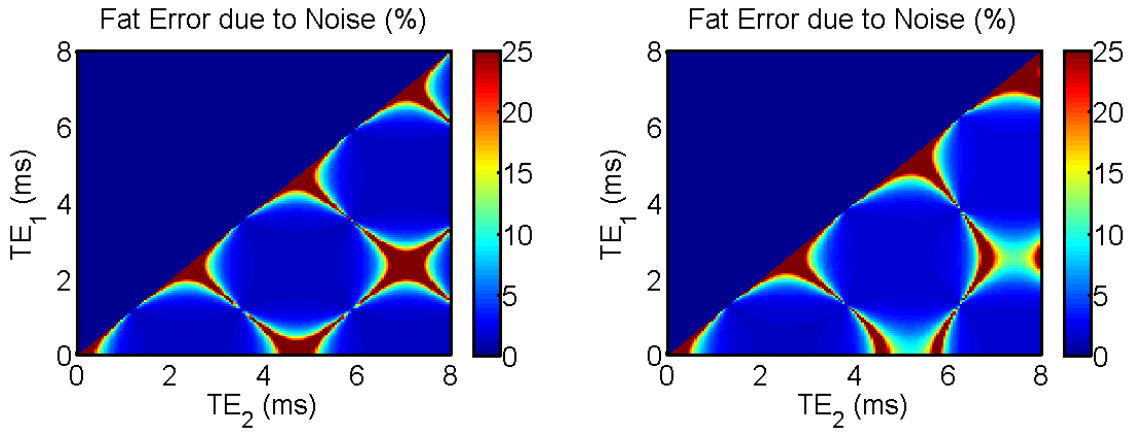

Figure 4.5. Percent error in F due to signal noise. The plot on the left is for the single-peak model, while the plot on the right is for the multi-peak model. In both cases, an SNR of 50 was assumed, with a background field of 1.5 T and a fat fraction of 1.

We now consider cases in which the voxel of interest contains a mixture of water and fat. Geometrically, a 50% mixture corresponds to the case in which the ellipses just barely touch at a single point in the single-peak model. In this case, a slight rescaling of either ellipse due to noise could cause the ellipses no longer to intersect at all or cause the single intersection point to become two very different intersection points. With this qualitative understanding of the problem, we expect the error to increase for fat fractions near 0.5. Calculation of error for a fat fraction of 0.6 does indeed show this to be the case, as shown in Figure 4.6. The regions in the TE_1-TE_2 plane where error is low are much smaller than for pure water or fat. However, the minimal error still occurs at the same echo times for both fat and water.

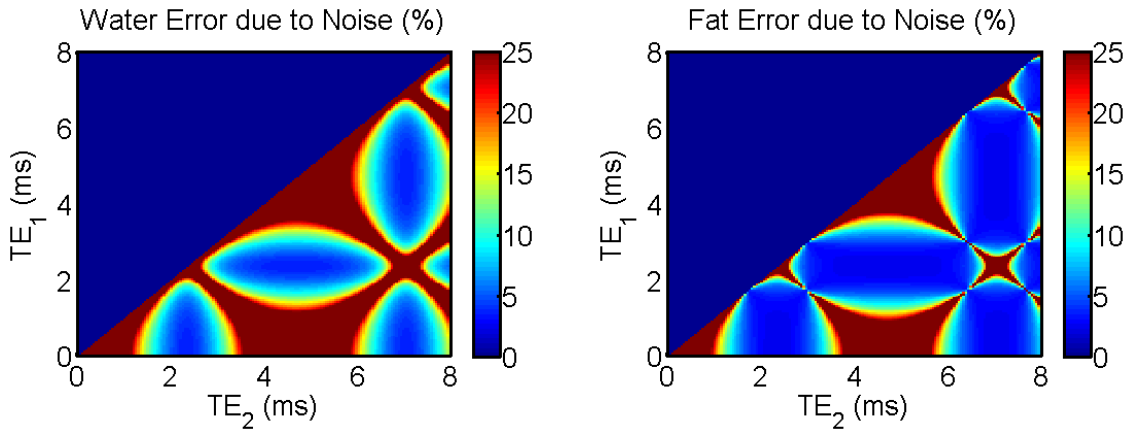

Figure 4.6. Percent error as a function of echo times for water (left) and fat (right) at a fat fraction of Q = 0.6 using the multi-peak model at SNR = 50 and B_0 = 1.5 T.

To examine more closely how error depends on fat fraction, we calculated error at different fat fractions for fixed echo times. Figure 4.7 shows plots of error versus fat fraction in both water values (top) and fat values (bottom). On the left is the result for the single-peak model, and on the right the result for the multi-peak model. The behavior for both models is almost exactly the same except that due to the dispersion of fat, the fat fraction for which the ellipses intersect at only one point in the first quadrant is no longer $Q = 0.5$. In fact, this varies with echo time but it tends to be close to 0.5.

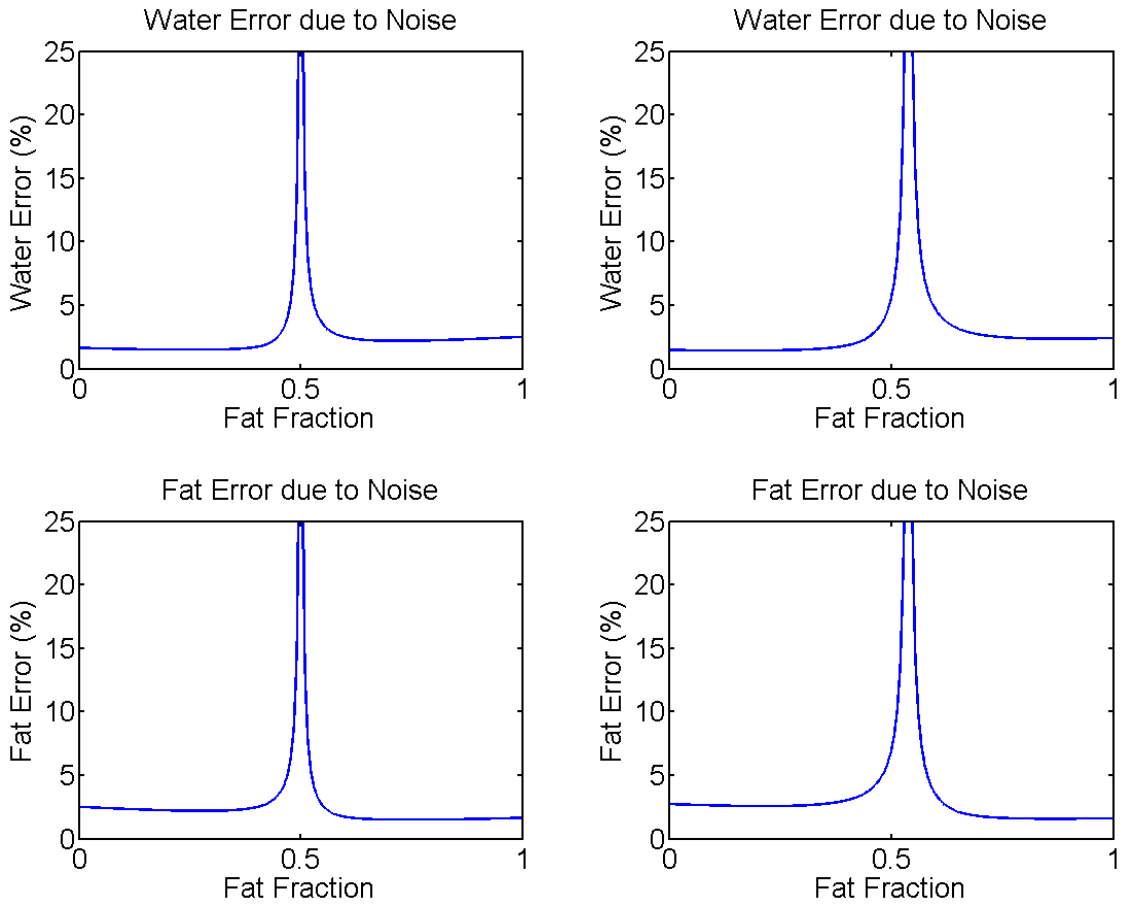

Figure 4.7. As a function of fat fraction, percent error in water values (top) and fat values (bottom) for the single-peak model (left) and multi-peak model (right). All

values correspond to SNR = 50 and B_0 = 1.5 at echo times of TE_1 = 1.0 ms and TE_2 = 2.0 ms.

4.2.2. Simulation Results

We now examine the same cases by simulation rather than analytical calculation. Our reason for doing so is that analytical error estimation by means of the method described in the previous section gives biased results, particularly where the function under consideration has large curvature.

To determine error by simulation, we generated signals using the Dixon signal equations with chosen values for W and F and echo times. We then added Gaussian noise with a specified standard deviation σ_S to both the real and imaginary parts of the signals to obtain 1000 noisy signal values for each TE combination. Water and fat values were calculated from these noisy signal values, and their standard deviations σ_W and σ_F were then taken to be the error in these values. This procedure was carried out for all possible combinations of echo times between 0 and 8 ms.

Figure 4.8 shows the simulation results that correspond to the analytical results given in Figure 4.4 through Figure 4.6. The plots are very similar to the analytical results, with the main difference being that for the multi-peak model, in some of the high-error regions (specifically, near TE_1/TE_2=0/5 ms and TE_1/TE_2=2.5/7.5 ms), the standard deviations generated in simulation are not as

high as the error predicted analytically. Since these are *TE* combinations to be avoided anyway, we are not concerned about these differences.

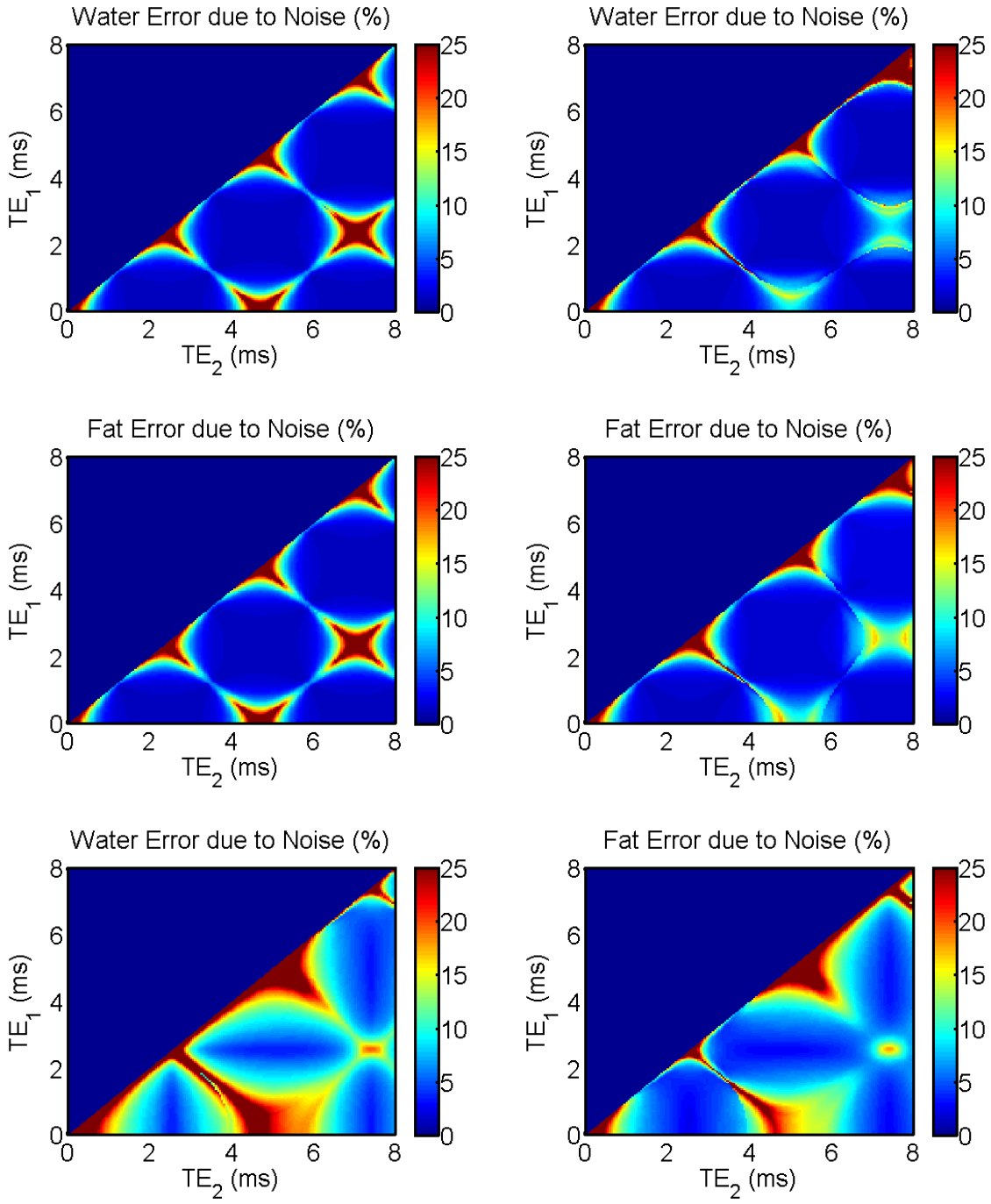

Figure 4.8. Simulated results corresponding to the analytical results presented in Figure 4.4 through Figure 4.6. In the first and second rows, the plots on the left correspond to the single-peak model while the plots on the right correspond to the

multi-peak model. In the third row, both plots correspond to the multi-peak model for a fat fraction of Q = 0.6. In all plots, SNR = 50 and B_0 = 1.5 T.

Figure 4.9 shows the simulation results for error versus fat fraction, again with the single-peak model on the left and the multi-peak model on the right. The blue data points are the simulated data, while the dashed red line shows the analytical results from the previous section. In practice (and in simulation), the error cannot really blow up to infinity even at a fat fraction of $Q = 0.5$. What actually happens when noise is added is that the ellipses either fail to touch, in which case there is no solution, or the single solution splits into two solutions which are different but, of course, finite. Therefore, in this region, the simulation breaks down. For all other fat fractions, however, the simulation results match the analytical results quite well.

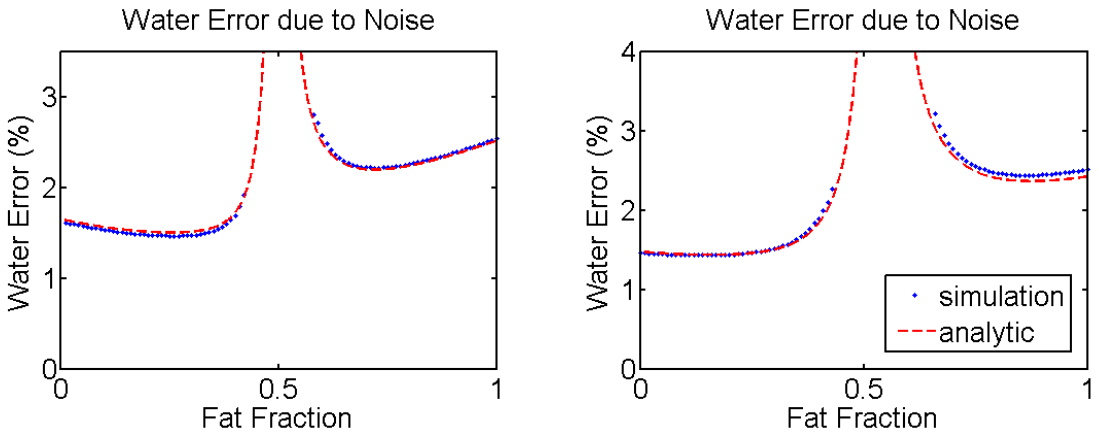

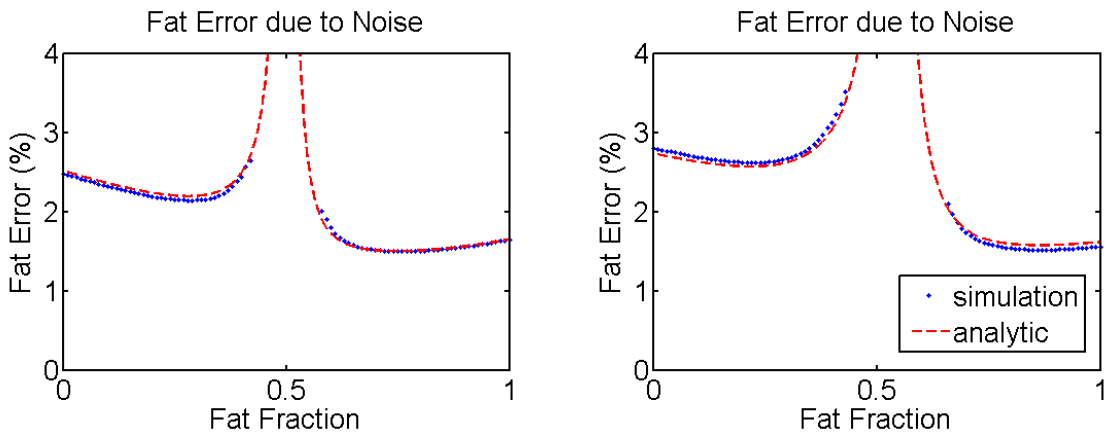

Figure 4.9. Error versus fat fraction as determined by simulation (blue data points) overlaid atop the analytical results from Figure 4.7. Single-peak results are on the left, and multi-peak on the right. All values correspond to SNR = 50 and B_0 = 1.5 at echo times of TE_1 = 1.0 ms and TE_2 = 2.0 ms.

4.2.3. Experimental Results

The following experiment was performed to quantify error as a function of echo times using actual MRI data. A fat-water phantom consisting of a bottle half-filled with water and half-filled with vegetable oil was scanned using a dual-echo GRE sequence with echo times ranging from 1.2 ms to 8.0 ms in intervals of 0.2 ms in a GE whole-body scanner at 1.5 T. Obtaining all echo time combinations was impractical (and impossible for cases in which TE_1 and TE_2 are within 1 ms of each other), so we verified that a first-echo acquisition at a given *TE* value is indistinguishable, apart from noise, from a second-echo acquisition at the same *TE* value. In post-processing, all *TE* combinations were then possible. A sample image is shown in Figure 4.10.

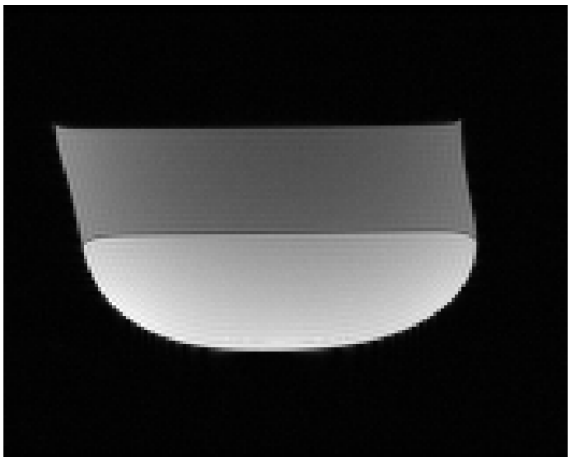

Figure 4.10. The oil-water phantom used for experimental determination of error due to signal noise.

For each echo time combination, separate fat and water images were generated using the Dixon signal equations. The standard deviations of the calculated fat and water values were then determined in a homogeneous water region and a homogeneous fat region by comparing the pixel intensities in the unaltered noisy images to those in a smoothed image obtained by convolution with a 5×5 window. This process was necessary to account for intensity differences due to coil sensitivity variations.

The results are shown in Figure 4.11. The error values compare favorably with both the analytical calculations and the simulation results. The symmetry difference between the error in water values and the error in fat values is readily apparent. Most importantly, the regions of minimal error are confirmed to be near echo time combinations that consist of one odd multiple of 2.5 ms and one even multiple of 2.5 ms.

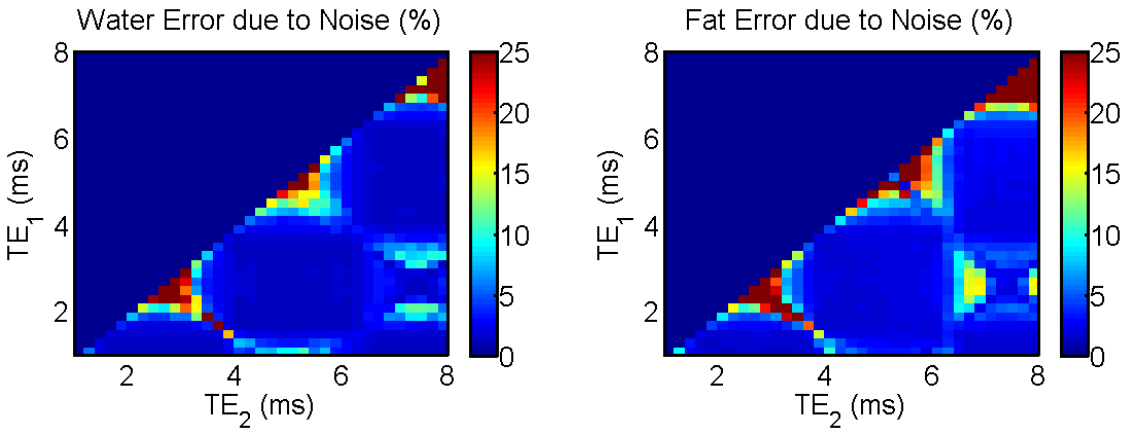

Figure 4.11. Experimental measurements of standard deviation of water values (left) and fat values (right) in an oil-water phantom scanned at 1.5 T. SNR in the water region was approximately 50, and SNR in the fat region was approximately 25.

4.3. The Effect of Noise on the Background Phasor

4.3.1. Analytical Calculation

The same analytic, simulated, and experimental investigations as in the previous section were also carried out to investigate error in the background phasor defined by $p_{rel} = e^{i(\varphi_2 - \varphi_1)}$, where $p_1 = e^{i\varphi_1}$ and $p_2 = e^{i\varphi_2}$. Defining $\alpha = \varphi_2 - \varphi_1$, the analytical equation for error in the relative background phase angle is

$$\sigma_\alpha = \sqrt{\left|\frac{\partial \alpha}{\partial S_{1R}}\right|^2 + \left|\frac{\partial \alpha}{\partial S_{1I}}\right|^2 + \left|\frac{\partial \alpha}{\partial S_{2R}}\right|^2 + \left|\frac{\partial \alpha}{\partial S_{2I}}\right|^2}\,\sigma_S$$

Eq. 4.2

The details of the calculation are given in Appendix A for both Berglund's and Eggers' methods.

Figure 4.12 shows phase angle error as a function of echo times for both single-peak (left) and multi-peak (right) models in water regions (top) and fat regions (bottom). As with error in water and fat values, the phasor error is the same in both water and fat regions under the single-peak fat model. In the multi-peak fat model, however, the same symmetry change occurs between water regions and fat regions (bottom right plot versus top right).

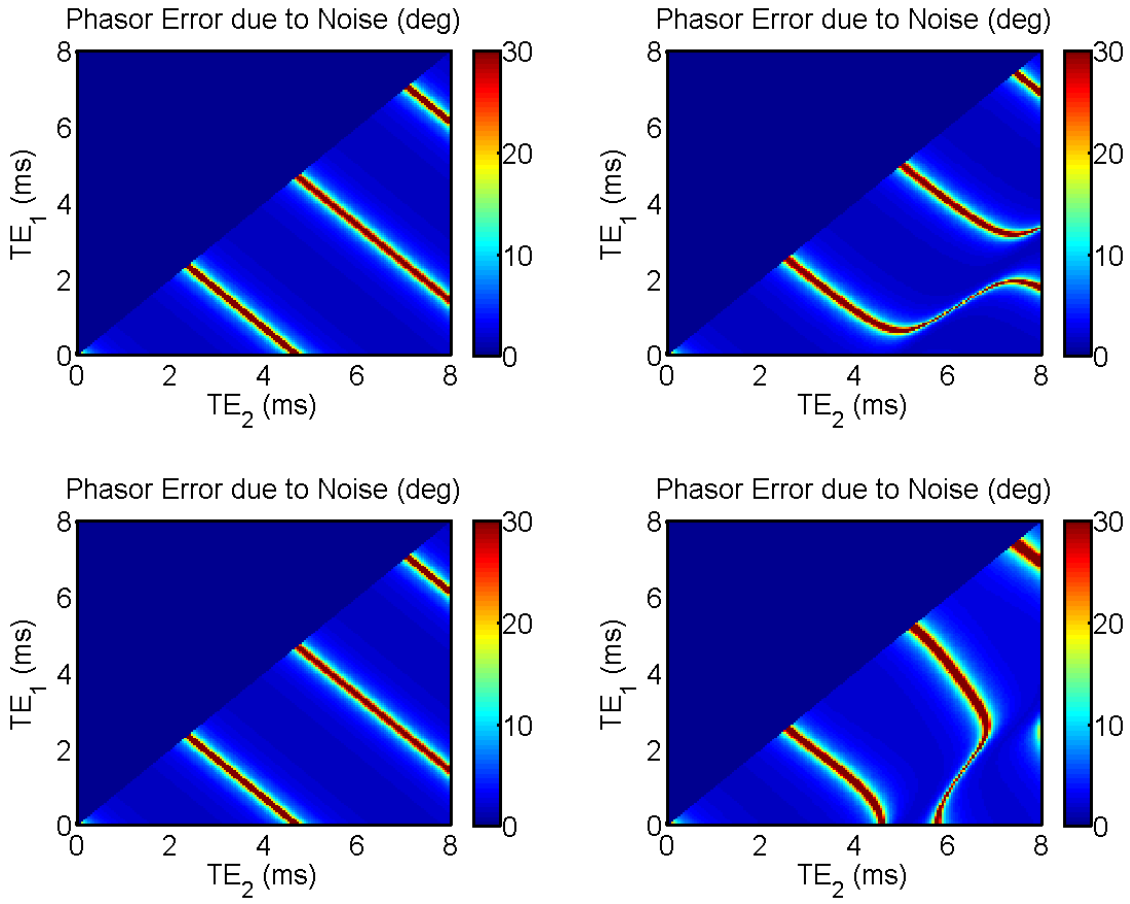

Figure 4.12. Error in relative background phase angle as a function of echo times for the single-peak model (left) and multi-peak model (right). The top plots correspond to pure water (Q = 0) and the bottom correspond to pure fat (Q = 1). In all cases, SNR = 50 and B_0 = 1.5 T.

As with fat and water error, the phasor error is higher for mixtures of fat and water than for pure fat or pure water. Figure 4.13 shows phasor error for $Q = 0.3$ and $Q = 0.6$ for the multi-peak model as examples.

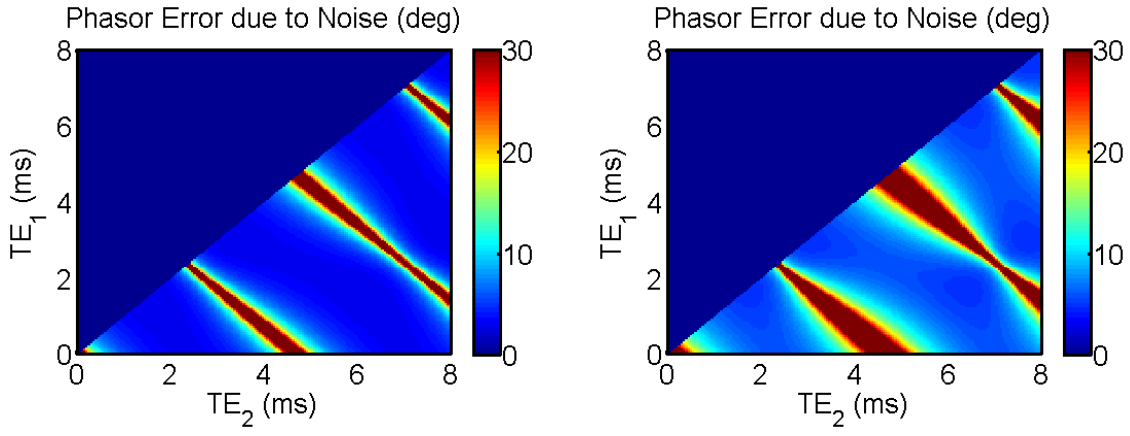

Figure 4.13. Phasor error versus echo times using the multi-peak fat model for fat fraction of Q = 0.3 (left) and Q = 0.6 (right). In both plots, SNR = 50 and B_0 = 1.5 T.

Figure 4.14 shows plots of phasor error versus fat fraction at selected *TE* values of 1.0 ms and 2.0 ms for the single-peak model (left) and multi-peak model (right). The behavior is almost identical to that of fat and water error, with a singularity occurring at the fat fraction for which the signals from the water and fat components have exactly the same magnitude.

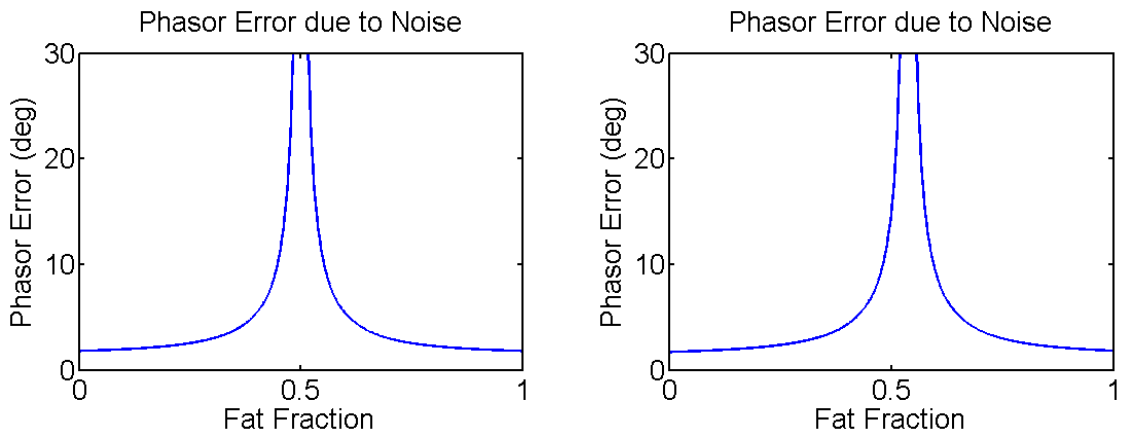

Figure 4.14. Phasor error due to noise (SNR = 50) for the single-peak model (left) and multi-peak model (right) for a selected TE combination of TE_1 = 1.0 ms and TE_2 = 2.0 ms at B_0 = 1.5 T.

4.3.2. Simulation Results

As was done for *W* and *F*, simulations were also performed to calculate standard deviation of the relative background phasor as a function of the echo times for a given noise level. Simulated signals were generated for both pure water and pure fat voxels, and Gaussian noise was added to both the real and imaginary channels, after which the background phasor was calculated using Eq. 2.9 and Eq. 2.15. The standard deviations of the resulting phase angles were then calculated. The results are shown in Figure 4.15.

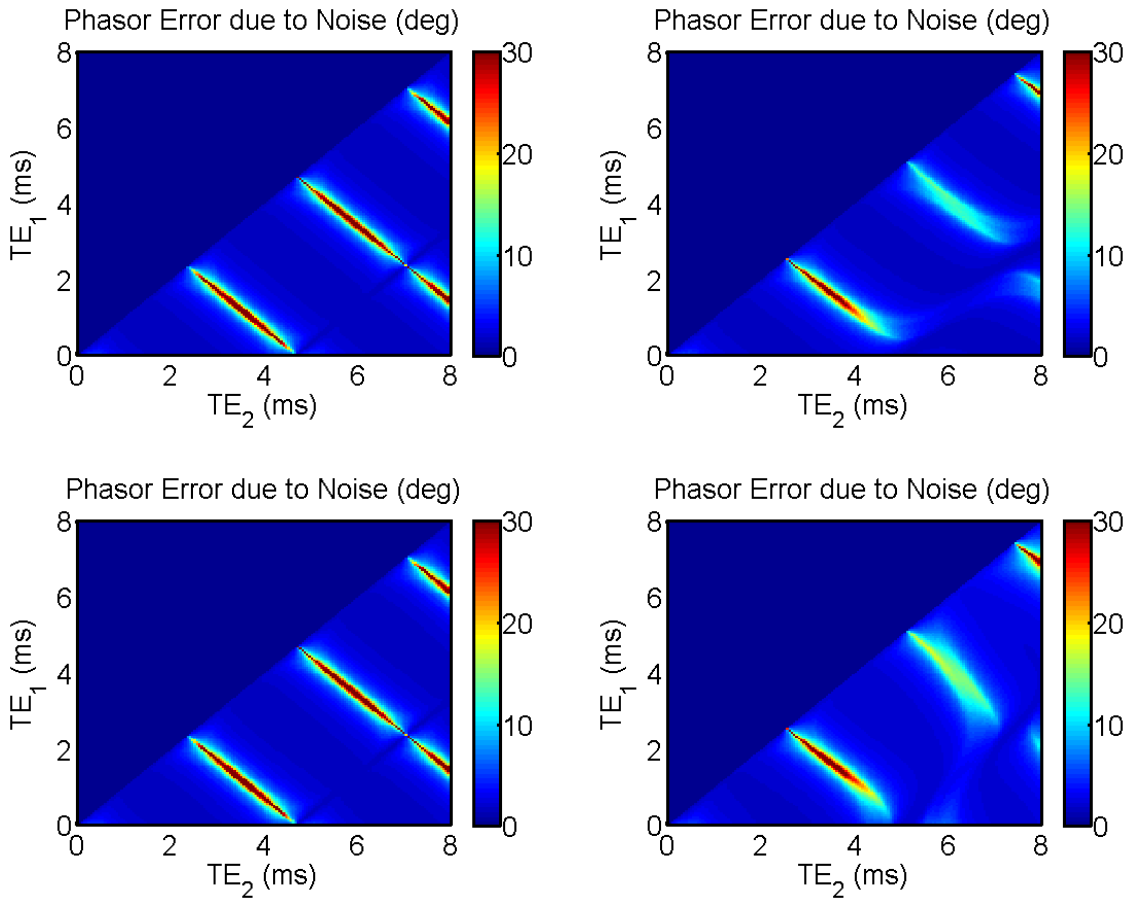

Figure 4.15. Simulation results for phasor error as a function of TE values using both the single-peak model (left) and multi-peak model (right) for pure water (top) and pure fat (bottom), corresponding to the analytical results shown in Figure 4.12. In all plots, SNR = 50 and B_0 = 1.5 T.

The simulation results match the analytical calculations closely. As with the error in W and F, for the single-peak model, the phasor error is the same in both water-dominant and fat-dominant pixels. However, the multi-peak fat model breaks this symmetry, and the resulting pattern in the phasor error is similar to the pattern in water and fat error. There is, however, one significant difference between the phasor error and W/F error. For W and F, the error becomes large when the fat

phase angles corresponding to the two echo times have a difference that is equal to a multiple of 360°. For the phasor error, this feature disappears.

Simulation was also carried out to calculate error as a function of fat fraction for a given *TE* combination. The results, for TE_1 = 1.0 ms and TE_2 = 2.0 ms, are shown in Figure 4.16. Just as for *W* and *F*, the error becomes large at fat fractions near 0.5, when the magnitudes of the fat and water components of the signal are equal. The simulated results agree quite well with the analytical calculations.

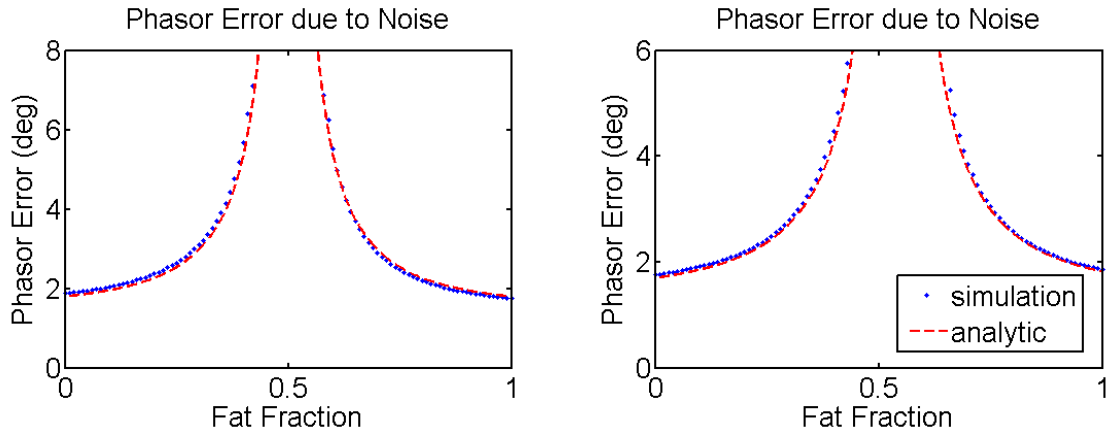

Figure 4.16. Phasor error as a function of fat fraction for the single-peak (left) and multi-peak (right) models, for SNR = 50, B_0 = 1.5 T, TE_1 = 1.0 ms, and TE_2 = 2.0 ms. The simulated values are plotted with a blue dotted line, while analytical values are plotted with the red dashed line.

4.3.3. Experimental Results

Finally, standard deviation of the phase angle was determined experimentally from the same data set that was used to determine *W* and *F* error. The background phasor was calculated for all pixels, and the standard deviation was

determined by comparing values in the noisy image to values in a smoothed image as before. The results are shown in Figure 4.17.

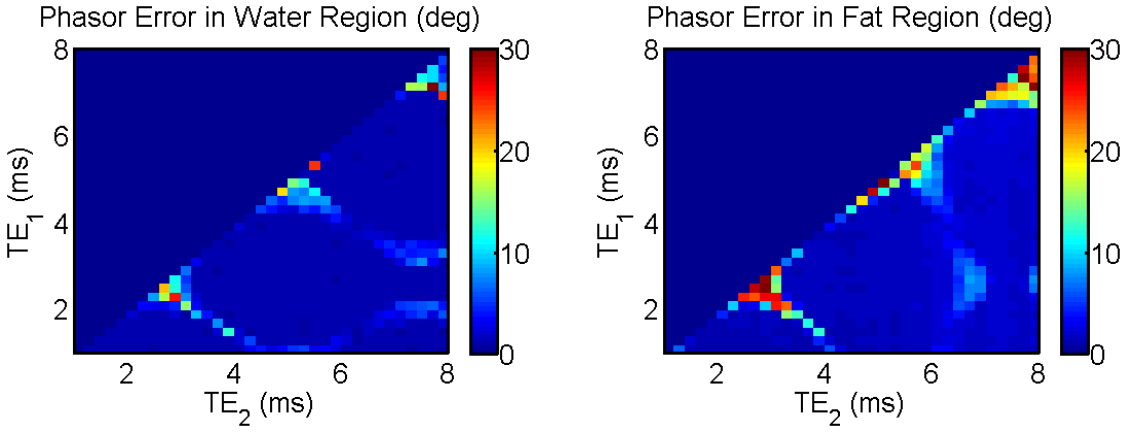

Figure 4.17. Experimentally determined phasor error in the water-only region of a phantom (left) and fat-only (right). In the water region, SNR was approximately 50, while in the fat region it was approximately 25.

In most regions, the error is quite small. Unlike the analytical calculations and simulation results, a large amount of error does occur near the line $TE_1 = TE_2$. The reason for this is unclear. The major difference between simulation and experiment was that the experimental data required a smoothed image for comparison to calculate standard deviation. It is possible that additional error was introduced during this process.

4.4. Difference between Possible Phasor Values

The information given in the previous section is still not sufficient to determine which TE_1 and TE_2 values are best for resolving the phasor ambiguity. We need to know not only the uncertainty in the possible phasor values but also the

magnitude of the difference between the two possible values that are obtained from the ambiguous solutions for *W* and *F*. For example, if the uncertainty is only 5 degrees but the two possible phasor values differ by only 3 degrees, then we will almost certainly be unable to choose the correct phasor. With this in mind, we have investigated the difference in phasor values as a function of fat fraction, TE_1, and TE_2. This was accomplished in both simulation and experiment by calculating the two phasor values from the two possible fat fractions and then finding the angular difference between them. The results are shown in Figure 4.18.

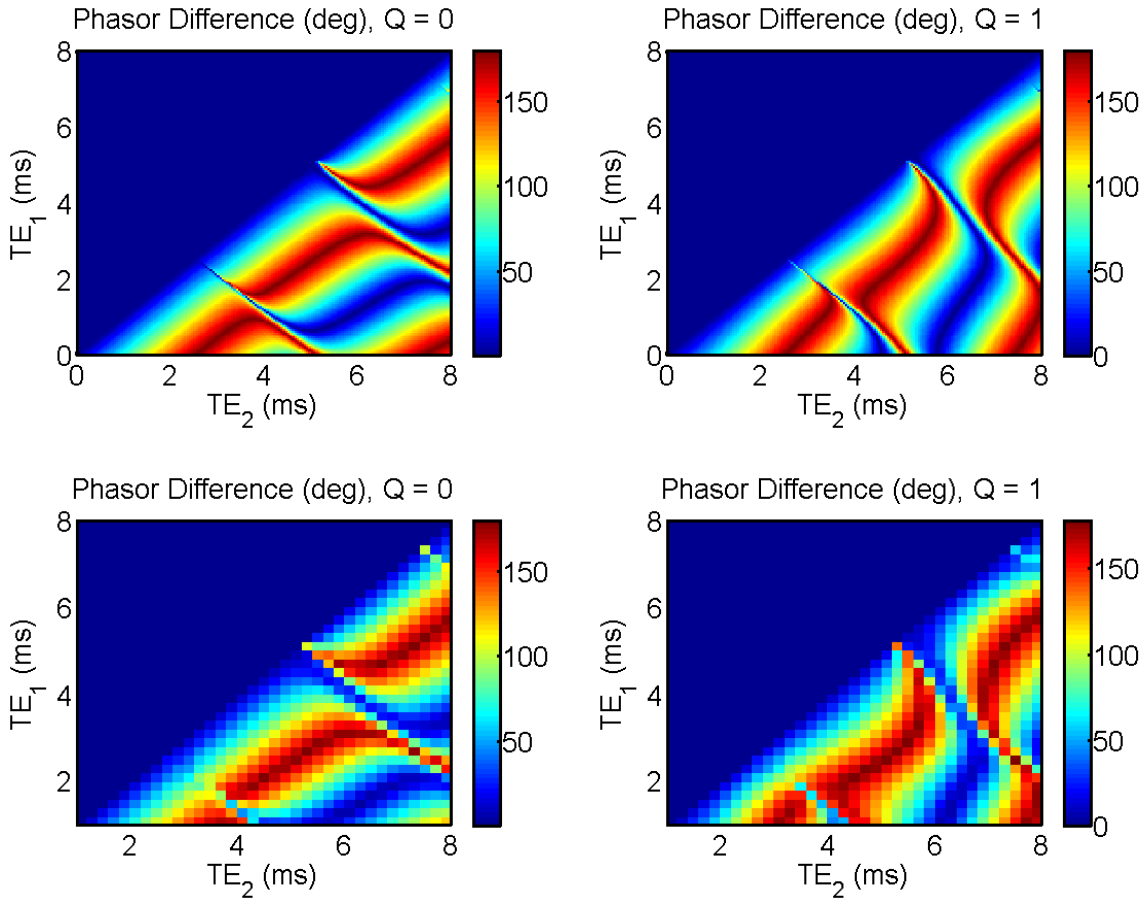

Figure 4.18. Simulated (top) and experimental (bottom) difference between the two possible background phasors as a function of the echo times for water-only (left) and fat-only (right) pixels. The simulation was carried out without noise, and the

experimental values are the result of averaging over a 200-pixel region in the phantom image.

Note that in this context, we want high values, so unlike in the previous section, the red regions are good and the blue regions are bad. The regions where the difference is highest, as is desired, are mostly aligned with the regions in which noise performance is highest. Thus, choosing echo times that yield good noise performance will automatically also result in a large difference between the two possible background phasor values, which makes phase correction algorithms more reliable. We also note that the difference between the two possible phase angles tends to be quite large (on the order of 100°) compared to error due to noise, which is typically on the order of a few degrees. Therefore, the difference between the possible phase angles will not be a significant concern when choosing scan parameters.

Chapter 5

Error Due to T_2* Decay

5.1. Introduction

Error can arise in our calculated values of water, fat, and background phasor not just due to noise in the signals S_1 and S_2, but also as a result of inaccuracies in the signal model. One such inaccuracy of which we are aware is that the signal equations neglect the exponential decay of the resonance signal—specifically, T_2* decay, which is due to intravoxel field inhomogeneity. Since T_2* is an unknown parameter that depends on tissue composition and position, including it in our model would render the problem unsolvable because we only have two equations in the two-point Dixon technique.

One way to deal with this problem is to acquire a third echo (i.e., perform a three-point Dixon technique); however, this increases scan time by roughly 50%. Another option is to ignore the decay. Since typical T_2* values are on the order of

tens of milliseconds, ignoring the signal decay is quite reasonable when the echo times are less than about five milliseconds. However, some error is still inevitable, especially for tissue types with extremely short T_2^* values. As with signal noise, error due to T_2^* decay will depend on the echo times that are used. If we can characterize this dependence, then we can establish guidelines for choosing echo times that will result in minimal error caused by T_2^* decay. This criterion can then be balanced with the goal of minimizing error due to signal noise.

With the above reasoning in mind, we present in this section an analysis of the dependence of error due to T_2^* decay on the echo times as well as on T_2^* itself. Simulations were carried out in which we first generated signals for known F, W, and T_2^* values using a model that includes T_2^* decay and then solved for W and relative background phasor using the model that neglects T_2^* decay. The difference between the initial values that were used to generate the signals and the calculated values was taken to be the error due to T_2^*. We validated our simulation results experimentally by scanning a fat-water phantom at various echo times and comparing the calculated values to the "true" values, which were taken to be the absolute values of the signal at the first echo time.

5.2. Methods

As described in Chapter 2, the traditional two-point Dixon signal equations, which ignore T_2^* decay, are

$$S_n = \left(W + \delta_n e^{i\theta_n} F\right) p_n$$

Eq. 5.1

where $n = 1,2$; the complex coefficient b_n has been written explicitly in terms of the phase θ_n and amplitude δ_n of fat relative to the initial values as determined from the seven-peak model; and p_n is an unknown background phasor. This model neglects the exponential decay of the signal, and solving the problem in the traditional way described in Chapter 2 will clearly result in a certain amount of error.

Taking T_2* decay into account, the signal equations become

$$S_1 = \left(W + \delta_1 e^{i\theta_1} F\right) p_1$$

$$S_2 = e^{-\Delta TE/T2^*} \left(W + \delta_2 e^{i\theta_2} F\right) p_2$$

Eq. 5.2

where the variables *W* and *F* now incorporate all decay that occurs before the first echo. The decay time T_2* is an additional unknown variable, rendering the system of equations unsolvable. In clinical practice, we therefore have no choice but to neglect T_2* or acquire a third echo. However, in simulation and phantom experiments, we already know *W* and *F* and therefore have enough information to apply both models and compare the results to gain an understanding of the error that is caused by neglecting T_2*.

To investigate this error by means of simulation, values were chosen for *W*, *F*, p_1, p_2, and T_2*, and Eq. 5.2 was used to generate simulated signals. Eq. 5.1 was then used to calculate the estimated values $\widehat{W}$ and $\hat{p}_{rel}$, which were compared to the

initially selected values to determine the error. This procedure was carried out for various echo time combinations with *TE* values ranging from 1.0 ms to 8.6 ms and for T_2^* values of 140 ms and 20 ms for a background field of 1.5 T in order to investigate error dependence on the *TE* values. To characterize error as a function of T_2^*, error was also determined at fixed *TE* combinations of 1.2/2.4 ms and 1.8/3.0 ms for T_2^* values ranging from 5 ms to 150 ms.

To measure the error experimentally, scans were performed using the same oil-water phantom described in the previous chapter in a 1.5 T GE full body scanner. The phantom had two sections, which were known to be pure fat and pure water. The "true" *W* values were assumed to be equal to the absolute value of the signal at the first echo, and T_2^* was determined from the amount of decay between echoes. As in the simulation, values of $\widehat{W}$ and $\hat{p}_{rel}$ were calculated using Eq. 5.1. The error caused by T_2^* was determined by taking the difference between these calculated values and the "true" values as determined directly from the images. This procedure was carried out for all possible *TE* combinations with *TE* values ranging from 1.0 to 8.6 ms in increments of 0.2 ms.

The water region in the unaltered phantom was perfectly homogeneous, resulting in a large T_2^* value (approximately 140 ms, which is why this is the value that was used in simulation). In order to investigate effects at shorter T_2^*, the scans were performed a second time with a paper clip taped to the phantom in order to introduce field inhomogeneities. Since the field variations introduced in this way were macroscopic with respect to voxel size, they did not result in true exponential

T_2* decay. However, the distortions still resulted in much faster decay with a measured effective T_2* of approximately 20 ms (the other value used in simulation).

Because the phantom contained vegetable oil rather than human fat and was at room temperature rather than body temperature, a calibrated fat model was used for the phantom experiment instead of the seven-peak model for human fat. Therefore, only error in W and p_{rel} was considered, since calibrated values of the fat signal necessarily include any T_2* decay. In practice, it is usually the water-only images that are diagnostically useful, and therefore we are more interested in the error in W than in F anyway.

5.3. Results

5.3.1. Simulation

The simulation results for phasor error (left, in degrees) and water error (right, percent) are shown in Figure 5.1. The error in both the relative background phasor and the calculated water value is much greater for T_2* = 20 ms than for T_2* = 140 ms, in agreement with the expectation that faster decay (i.e., smaller T_2*) should result in greater error. The dependence of the error on the echo times, however, is more complicated. The general behavior is similar to that of error caused by signal noise, which tends to be large at TE combinations for which $\theta_1 \pm \theta_2$ is an integer multiple of 360° (the diagonal high-error regions in the figure). The departure from an exact linear relationship at larger echo spacings is due to the multi-peak nature of fat.

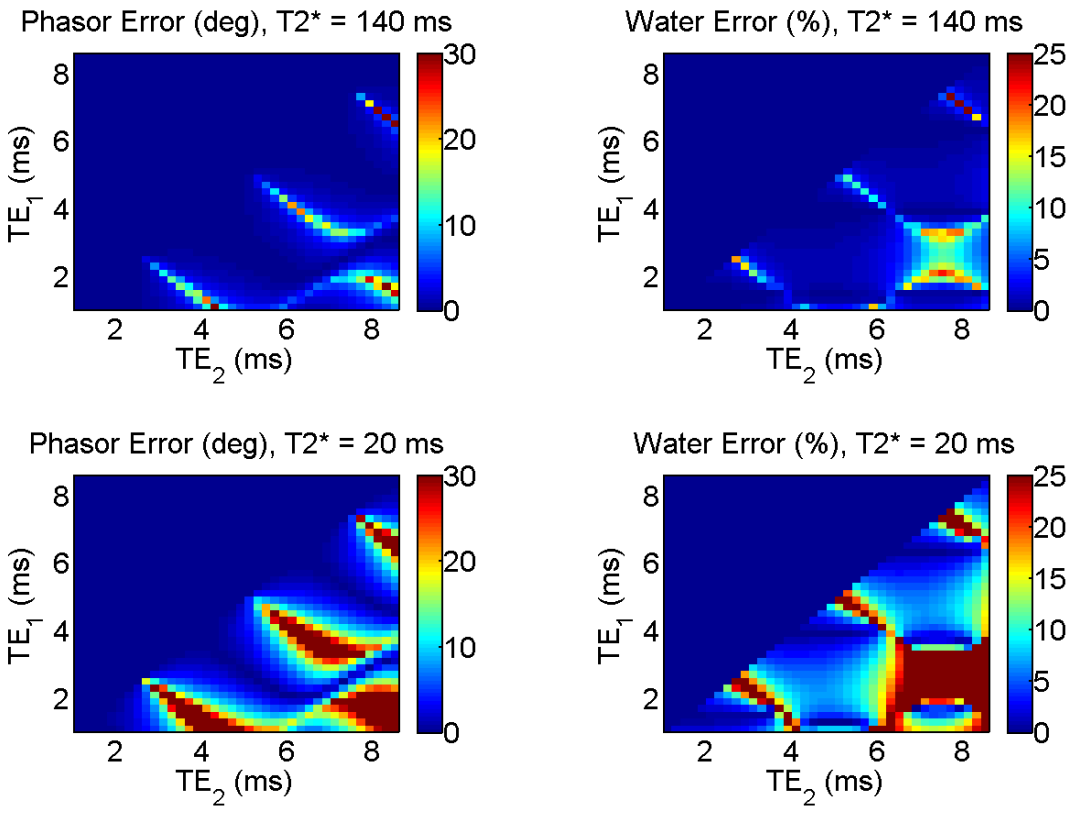

Figure 5.1. Simulated error due to T_2 decay in the background phasor (left) and water values (right) for T_2* values of 140 ms (top) and 20 ms (bottom).*

Figure 5.2 shows graphs of phasor and water error versus T_2* for selected TE combinations of 1.2/2.4 ms and 1.8/3.0 ms as determined by simulation. In all cases, the error decreases monotonically as $1/T_2$*. However, the error for TE_1/TE_2 = 1.8/3.0 ms is approximately ten times that for TE_1/TE_2 = 1.2/2.4 ms, demonstrating how sensitively the magnitude of the error can depend on the echo times. For TE_1/TE_2 = 1.2/2.4 ms, the error is quite small even for relatively short T_2* values (about 10 ms), whereas for TE_1/TE_2 = 1.8/3.0 ms, the error becomes unacceptably large for T_2* values below 50 ms.

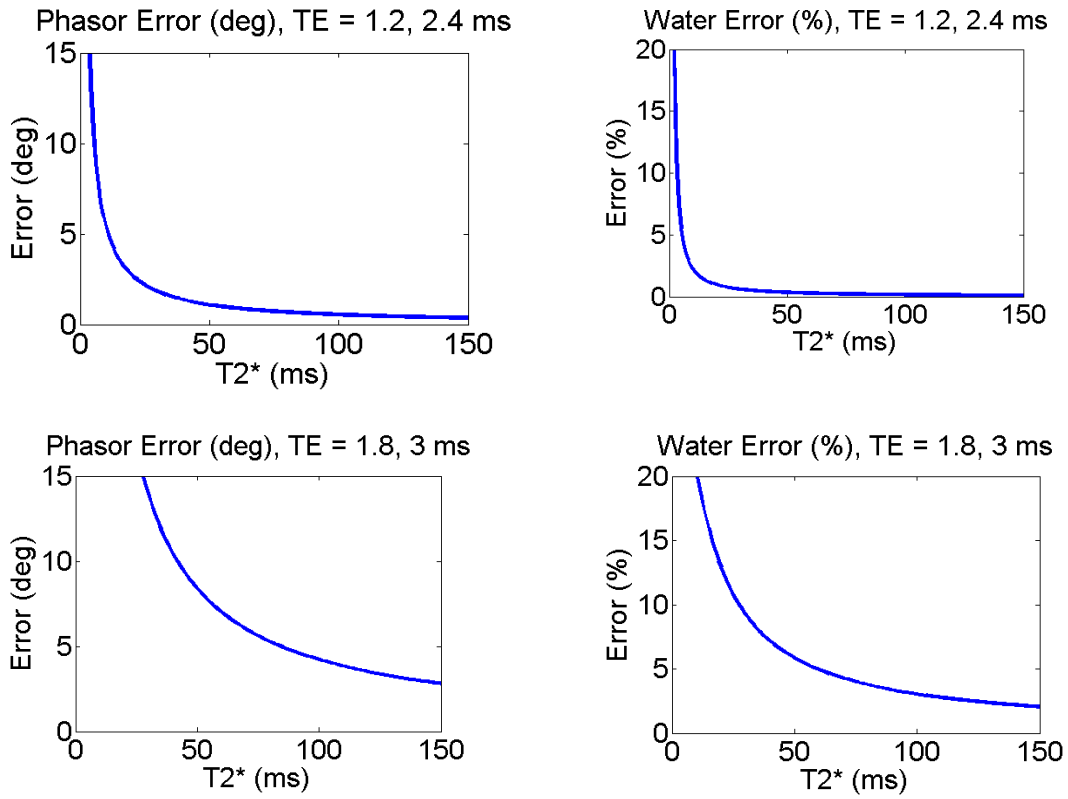

Figure 5.2. Phasor error (left) and water error (right) for echo time combinations of TE_1/TE_2 = 1.2/2.4 ms (top) and 1.8/3.0 ms (bottom). The magnitude of the error at TE_1/TE_2 = 1.8/3.0 ms is approximately ten times the error at TE_1/TE_2 = 1.2/2.4 ms, demonstrating how sensitively the error depends on the echo times.

5.3.2. Experiment

The corresponding experimental results are shown in Figure 5.3. Qualitatively, they match the simulation results well. One difference, which can be seen most easily in the T_2* = 140 ms data set, is that the experimental data include error due to both T_2* and signal noise. The error due to signal noise is easiest to see in the small, equally spaced triangular-shaped regions of high error close to the line $TE_1 = TE_2$. The same features are clearly visible when water error is plotted as a function of signal noise only (see Figure 5.4).

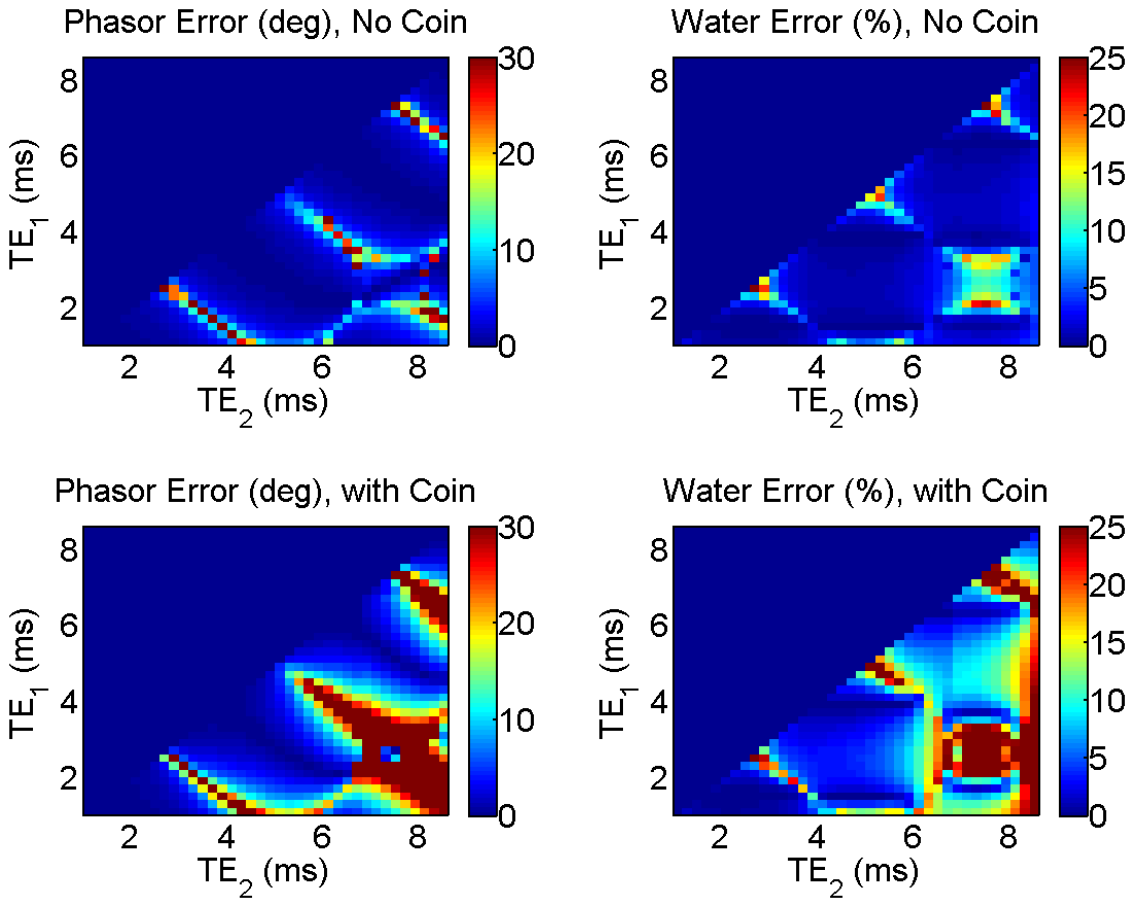

Figure 5.3. Experimental error in background phasor (left) and water (right) for T_2 values of approximately 140 ms (top) and 20 ms (bottom).*

The experimental plot for T_2* = 20 ms also matches the simulation results well. In addition to noise, the small differences are likely due to the fact that the field inhomogeneity introduced by the presence of a paper clip is macroscopic compared to the voxel size, resulting in a smooth field variation across individual voxels. As a result, the signal decay is not truly exponential and should not be expected to match simulation perfectly. Nevertheless, the regions of minimal error in the experimental plot match those in the simulation plot.

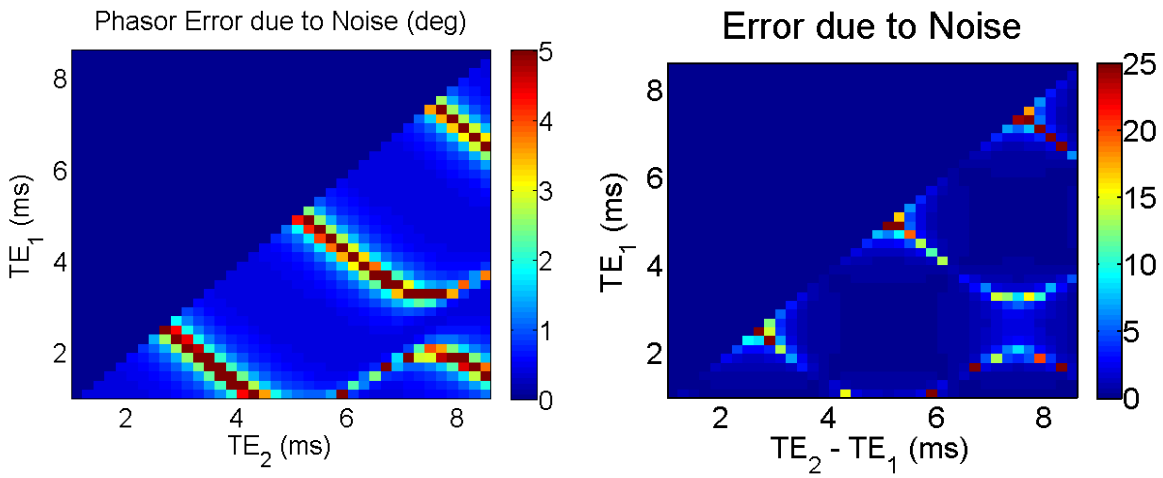

Figure 5.4. Error in background phasor (left) and water (right) due to signal noise for SNR = 100. The plot of water error in Figure 5.3 is apparently a combination of error due to signal noise and error due to T_2 decay.*

5.4. Discussion

As mentioned above, the dependence of error due to T_2* decay on the echo times is similar to that of error due to signal noise. There is one major difference, however. Error due to signal noise alone is minimized at *TE* combinations for which $\theta_1 + \theta_2$ and $\theta_1 - \theta_2$ are both odd multiples of 180°. The error due to T_2* decay, on the other hand, is skewed since the symmetry is broken by the fact that T_2* decay can only result in a *reduction* in signal magnitude, whereas noise is equally likely to increase or decrease the signal magnitude. Furthermore, since we are absorbing T_2* decay that occurs before the first echo time into the values of *W* and *F*, it is only the second signal that is reduced in magnitude. As a result, whereas the opposed-phase/in-phase echo times of 2.53/5.09 ms result in minimal error due to noise, they do not minimize error due to T_2*.

According to the simulation results, error in W is minimized for any value of T_2^* along certain lines of constant TE_1, specifically TE_1 values of 1.3, 3.8, and 6.2 ms (for 1.5 T). Theoretically, a TE_2 value as close to TE_1 as possible minimizes the error due to T_2^* decay at these TE_1 values, but when TE_2 is close to TE_1, error due to noise dominates the error due to T_2^*. Furthermore, in a dual echo scan, a realistic TE_2 value must be at least about a millisecond larger than TE_1. Reasonable echo time combinations for minimizing error due to T_2^* decay are therefore TE_1/TE_2 = 1.3/2.3 or 3.8/4.8 ms.

Overall, the experimental results confirm the simulation results. The magnitude of the error depends strongly on T_2^* and increases as T_2^* decreases, and the dependence on the echo times is similar to that of error caused by signal noise. The same difference between signal noise error and T_2^* decay error is evident in the experimental data as in simulation. In particular, minimum error in the water value is achieved for TE_1 = 1.4, 3.8, 6.2 ms, which match the values found in simulation. Since the experimental data include noise, the TE_2 values that minimize error are not those closest to TE_1, but TE_2 = 2.6, 5.0, 7.6 ms, respectively.

The background phasor error behaves differently from that of the water values. Minimum error in the phasor is achieved along lines at which $\theta_1 + \theta_2$ is equal to an odd multiple of 180° (as long as $TE_2 - TE_1$ is less than about 5 ms). This is the same as the rule for minimizing error due to signal noise. Thus, if the goal is to minimize phasor error due to T_2^* decay, echo times should be chosen in the same way as to minimize error due to signal noise. Since large phasor error can result in

fat-water swapping, this criterion may be more important than reducing error in the water values themselves.

5.5. Conclusions

Our simulation and phantom studies show that T_2^* decay due to field inhomogeneity leads to error both in the relative background phasor, potentially resulting in water-fat swapping, and in the values of water. These errors increase when T_2^* decreases and are dependent on echo times. Judicious selection of the echo times, which are subject to other scan considerations, can minimize these errors. If choosing echo times in order to minimize error, one must take into account whether the error is expected to be dominated by signal noise or by T_2^* decay. If signal noise is expected to be the dominant error source, then one should choose the traditional in-phase/opposed-phase echo times. If T_2^* decay is expected to dominate, then the echo times that minimize error due to T_2^* as shown by our simulation results should be used.

Chapter 6

Fat-Water Determination without Phase Correction

The development of the multi-peak model of fat and the ability to choose flexible echo times make possible a significant advancement in the process of resolving the inherent ambiguity of solutions in the two-point Dixon problem. The multi-peak model breaks the symmetry between the water-dominant and fat-dominant solutions so that under certain circumstances only one of the solutions is physically allowable, rendering the ambiguity immediately resolved; and the ability to choose flexible echo times enables us to create precisely those circumstances under which only one physical solution exists.

In this chapter, we present an analysis of the feasibility of this method of direct fat and water determination without phase correction. We first discuss the underlying theory in the context of our geometric interpretation of the Dixon problem, and we then present results from simulation, phantom, and *in vivo*

experiments to demonstrate the degree of accuracy that is achievable without phase correction when noise and other non-ideal conditions are present.

6.1. Theory

Recall that in our geometric interpretation of the two-point Dixon problem, the tilt angle of the ellipse given by the square of the modulus of the signal equation for the multi-peak fat model is

$$\psi = 90° + \frac{1}{2} cot^{-1}\left(\frac{1 - |b|^2}{2b_R}\right)$$

Eq. 6.1

For the single-peak model, $|b| = 1$, and this simplifies to

$$\psi = 90° + 45° \times \text{sign}(b_R)$$

Eq. 6.2

Thus, when the traditional single-peak model is used, the tilt angles of both ellipses are fixed at either 135° or 45°. In either case, both ellipses are symmetric across the line $F = W$. Consequently, their intersection points are also symmetric across the line $F = W$, with the result that as long as one solution exists in the first quadrant, then another solution—the reflection of the first—also exists in the first quadrant. Since the correct solution is expected to be in the first quadrant because W and F should be non-negative, the other possible solution must also be in the first quadrant. The only way to determine which one is correct is by application of a phase correction algorithm. This situation is depicted in Figure 6.1.

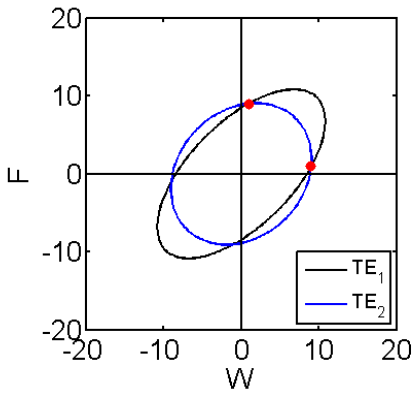

Figure 6.1. Ellipses generated using a single-peak model with B_0 = 1.5 T, TE_1 = 3 ms, TE_2 = 6 ms, W = 1, and F = 9 (in arbitrary units). Because both ellipses are symmetric across F = W, the first quadrant contains two solutions. Traditionally, a phase correction algorithm would be necessary to determine which one is correct.

When the multi-peak nature of fat is taken into account, the coefficient *b* no longer has unit modulus, and the tilt angle can take on any value between about 49° and 135°. The exact value of the tilt angle depends on the echo time that is chosen. As a result of the change in tilt angle, it is possible for the incorrect solution, which would be in the first quadrant under the single-peak model, to be rotated out of the first quadrant under the multi-peak model. An example is shown in Figure 6.2, using the same parameters as in Figure 6.1. The signal ellipses for *TE* = 3 ms and *TE* = 6 ms have tilt angles of 50° and 106°, respectively, so that the symmetry across the line *F* = *W* is broken.

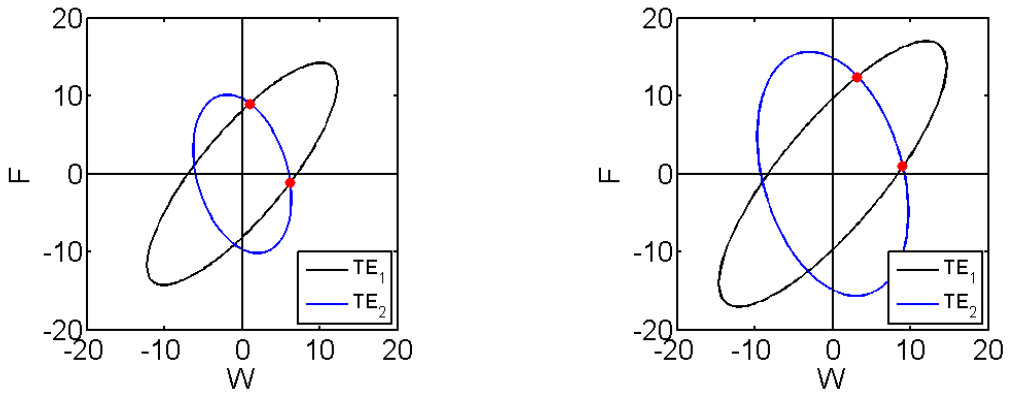

Figure 6.2. Ellipses generated using a multi-peak model with B_0 = 1.5 T, TE_1 = 3 ms, TE_2 = 6 ms. On the left, W = 1 and F = 9. The tilt angles of the ellipses have changed so that the water-dominant solution has been rotated outside of the first quadrant. This solution can now be discarded because it is unphysical. On the right, the water and fat values have been swapped to W = 9 and F = 1; in this case, the solutions are still ambiguous.

Interestingly, this break in symmetry affects fat-dominant and water-dominant pixels differently. For these echo times, a fat-dominant pixel has only one physical solution, as shown on the left in Figure 6.2, whereas a water-dominant pixel still has two physical solutions, as shown on the right. The difference is due to the dispersion of the fat signal caused by its multi-peak nature. For a fat-dominant pixel, this dispersion results in a weaker signal at TE_2, and hence a smaller ellipse that crosses the TE_1 ellipse below the *W* axis. For a water-dominant pixel on the other hand, the signal remains strong at TE_2 since there is no dispersion, and the corresponding ellipse is much larger, intersecting the TE_1 ellipse above the *W* axis.

In general, whether it is the fat-dominant pixels or the water-dominant pixels that have only one solution depends on the *TE* values. In fact, for a given *TE* combination, it is possible that either water-dominant pixels or fat-dominant pixels,

(or both or none) will have only one physical solution. Figure 6.3 shows simulated results for which tissue type (fat, water, both, or none) yields only one physical solution at different *TE* combinations. The blue (yellow) regions correspond to the *TE* combinations for which water-only (fat-only) pixels have only one physical solution but fat-only (water-only) voxels have two possible solutions; and the green regions correspond to the *TE* combinations at which both water-only and fat-only pixels yield only one physical solution.

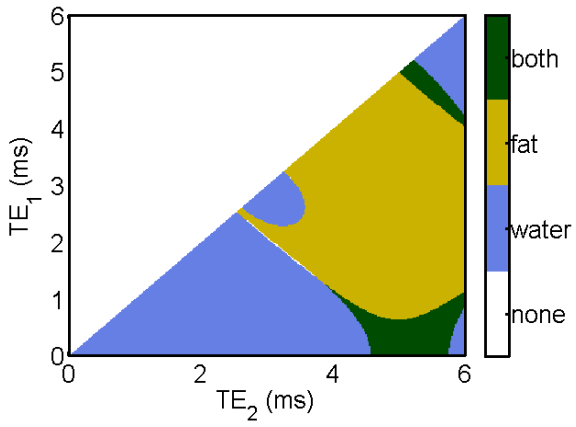

Figure 6.3. Tissue types (fat or water) that yield only one solution at various TE combinations for 1.5 T. This is consistent with results presented by Eggers.[27]

We might expect *TE* combinations in the green region to be ideal since both fat- and water-dominant pixels have only one feasible solution. However, noise performance in these regions is prohibitively poor, and we find that correct identification of both fat and water pixels can still be achieved for *TE* combinations that are in the blue or yellow regions. If, for example, we are using a *TE* combination

for which water-only voxels yield only one solution, then all voxels with two possible physical solutions must be fat-dominant.

The above analysis depends on the assumption that all voxels are either pure water or pure fat. However, while most voxels in human tissue do tend to be nearly all water or nearly all fat, mixing does occur, and voxels that contain a mixture will generally have two solutions in the interior of the first quadrant, in which case a high degree of rotation is needed in order to move the incorrect solution out of the first quadrant. The following example demonstrates a case in which the ambiguity can still be resolved even with a substantial amount of mixing. With TE_1 = 3.4 ms and TE_2 = 6.2 ms at B_0 = 1.5 T, a voxel that is 80% fat and 20% water still yields only one physical solution, as shown in Figure 6.4.

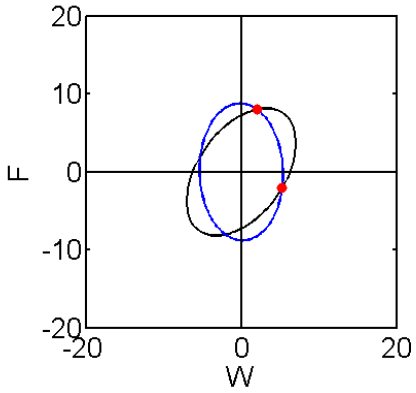

Figure 6.4. Possible solutions for Q = 0.8 with TE_1 = 3.4 ms and TE_2 = 6.2 ms at 1.5 T.

The results in Figure 6.3 also ignore the effects of noise and other potential deviations from our ideal signal model. The presence of noise causes fluctuations in the measured values of $|S_n|$ and thus in the sizes of the corresponding signal ellipses.

Figure 6.5 shows the consequences under the same imaging conditions as those in Figure 6.2 when different levels of random noise are added to the measured signal. At a relatively high SNR of 50, as shown on the left, the deviation is small and the solution remains unambiguous. However, when SNR decreases to 15, as shown on the right, the fluctuation in the size of the signal ellipses becomes large enough that the correct solution can be moved into the unphysical second quadrant while in some cases the false solution is moved into the physical first quadrant.

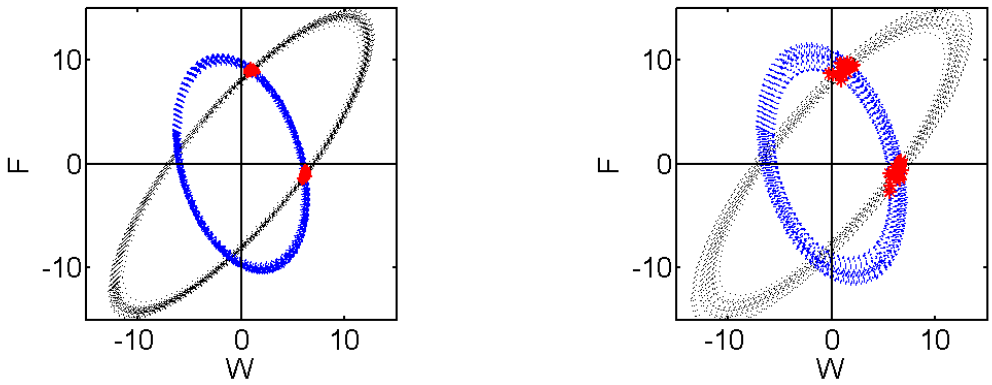

Figure 6.5. The effect of noise on the physicality of possible solutions. At a low noise level corresponding to SNR = 50, the solutions change by only a small amount and can still be accurately identified as physical or unphysical (left). At higher noise levels (SNR = 15), physical solutions can appear unphysical and vice versa (right).

In light of the above considerations, direct fat-water separation without phase correction is possible in theory. In cases where the majority of voxels in the anatomy to be imaged are either nearly all water or nearly all fat, echo times can be chosen such that water-dominant voxels will yield only one possible solution while fat-dominant voxels will yield two, or vice versa. Due to the effects of noise, a suitable threshold must be chosen such that solutions that are negative by more

than this threshold can be discarded. In the following sections, we describe the application of such a method in both simulation and experiment.

6.2. Methods

The feasibility of the method described above was investigated by computer simulation and experiment at different *TE* combinations and noise levels. The simulations were performed at SNR levels of 10, 25, and 50 at B_0 of 1.5 T and at all *TE* combinations for TE_1 and TE_2 between 0 and 6 ms in increments of 0.2 ms. Since most *in vivo* tissues are either water-dominant or fat-dominant, we generated signal values S_1 and S_2 for water-only and fat-only pixels according to Eq. 2.1 for each *TE* combination. The coefficient *b* was based on Eq. 2.17 for the seven-peak fat model. A total of 1000 Gaussian-distributed noise values were added to S_1 and S_2 for each pixel at each noise level studied.

For *TE* combinations at which water-only pixels are theoretically unambiguous, all pixels with only one non-negative solution were assumed to be water-dominant while all pixels with two physical solutions were assumed to be fat-dominant. For *TE* combinations at which fat-only pixels are expected to be unambiguous, all pixels with only one physical solution were assumed to be fat-dominant while all pixels with two physical solutions were assumed to be water-dominant. The results were then compared to the known pixel water and fat designation to determine the percentage of pixels that had been correctly identified using the physicality requirement.

For phantom experiments, we modified a commercially available 3D dual echo fast spoiled gradient echo sequence to make the echo times operator-adjustable, subject to the pulse sequence's physical timing constraints. We then used the modified pulse sequence to acquire raw data from a water and fat phantom that consisted of approximately half soybean oil to simulate fat, and half distilled water mixed with 0.75 mM of Magnevist gadolinium contrast agent (Bayer HealthCare, Wayne, NJ). As with the computer simulation, different sets of raw data were acquired with echo times ranging from 1.0 ms to 6.0 ms in increments of 0.2 ms. All phantom experiments were conducted on a GE 1.5 Tesla whole-body scanner (GE Healthcare, Waukesha, WI) using an 8-channel phased array head coil. Because the chemical composition of the soybean oil is different from human adipose tissue, the fat signal model as a function of echo time for the phantom was determined by using a previously published image-based calibration method[26] rather than using the seven-peak model based on MR spectroscopy.

For *in vivo* validation, the same modified 3D dual-echo fast spoiled gradient echo sequence was used to image the legs of a healthy subject in the axial plane using an 8-channel torso phased array receiver coil on a 1.5 Tesla GE whole body MRI scanner. The echo times were varied in the same range as that for the phantom experiments. Other scan parameters were: field of view = 40 cm, slice thickness = 5 mm, receiver bandwidth = ±125 kHz, acquisition matrix = 160×160, excitation flip angle = 15°, total number of slices = 38, repetition time = minimum. We verified that the signal difference between the first-echo and second-echo images that were acquired at the same echo time but from two different scans was negligible. Thus, fat

signal can be assumed to vary only as a function of *TE*, independent of the dual-echo acquisition. In order to establish the reference standard of water and fat identification for the *in vivo* images, we implemented a phase correction algorithm similar to that proposed by Xiang[25] and used the water and fat separation results after applying the algorithm to the two acquired images. We then compared the results to determine the percentage of the pixels that were correctly identified on the basis of physicality alone.

6.3. Results

For a simulated phantom with equal numbers of water-dominant and fat-dominant pixels, Figure 6.6 shows the probability of correct pixel identification as a function of *TE* combination at three different SNR levels. The highest probabilities at the SNR levels of 10, 25, and 50 were approximately 85%, 99%, and 100%, respectively. At all SNR levels, the probability was highly dependent on the *TE* values. Except at some singular TE_1/TE_2 combinations, the lowest probability of identifying the correct solution was approximately 50%, which is equivalent to randomly selecting a solution. Figure 6.6 further shows that TE_1/TE_2 combinations near 3/6 ms (for B_0 = 1.5 T) yield the highest probability of the correct identification for water and fat solutions.

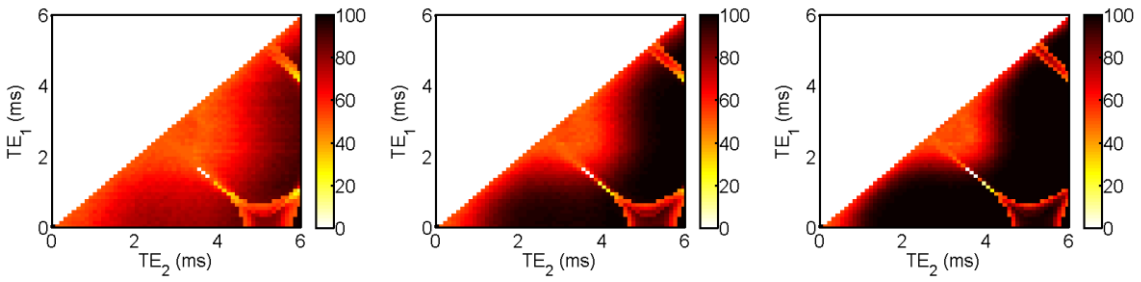

(a) (b) (c)

Figure 6.6. Percentage of correctly identified pixels as a function of echo times.

Figure 6.7 shows the results of the water and fat separation technique based on the physicality requirement alone when applied to the images acquired of a water-fat phantom at 1.5 T and at a TE_1/TE_2 combination of 3/6 ms. Figure 6.7(a) is the magnitude image of the phantom from the first echo at 3 ms. With relatively high SNR and a proper choice of the TE_1/TE_2 combination, the fat-only image (b) and the water-only image (c) show excellent water-fat separation (except for a few isolated pixels near the water-fat or container boundaries).

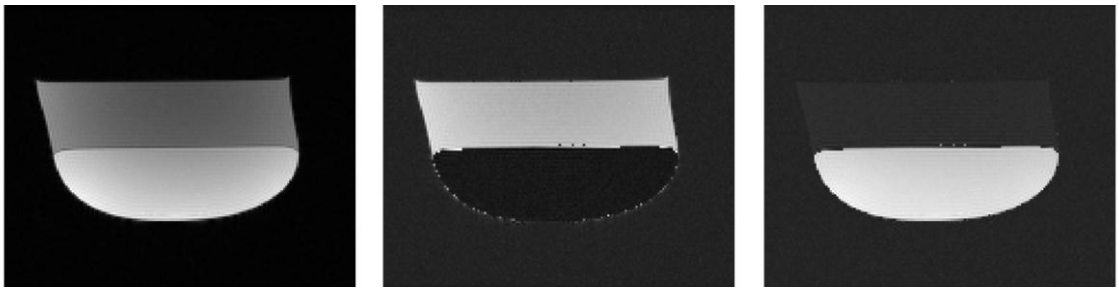

(a) (b) (c)

Figure 6.7. First-echo image, unseparated. (b) Oil only. (c) Water only.

Figure 6.8 shows the percentage of the pixels that were correctly separated for *in vivo* images acquired at different TE_1/TE_2 combinations using the water-fat separation results from the phase correction-based method as the reference

standard. Comparison with Figure 6.6 indicates that the overall behavior matches the computer simulation well. In particular, *TE* combinations that yielded better water-fat separation in computer simulation (e.g., near TE_1/TE_2 of 3/6 ms) also yielded better water-fat separation *in vivo* than at other TE_1/TE_2 combinations. The maximum percentage of correctly identified pixels *in vivo* was noted to be approximately 95% and was achieved at a TE_1/TE_2 combination of 3/6 ms. This maximum percentage is slightly lower than that found in computer simulation, and the difference is likely due to the fact that that most voxels in real human tissue are neither 100% pure water nor 100% pure fat, as assumed in simulation. The less pure a voxel is, the closer its two possible solutions are to the line $F = W$, and the less likely it is that one of the solutions will be moved outside of the first quadrant by the breaking of symmetry. Further error could be a result of deviations from the ideal signal model in addition to noise (e.g., T_2^* relaxation) for some pixels near tissue-tissue or tissue-air interfaces.

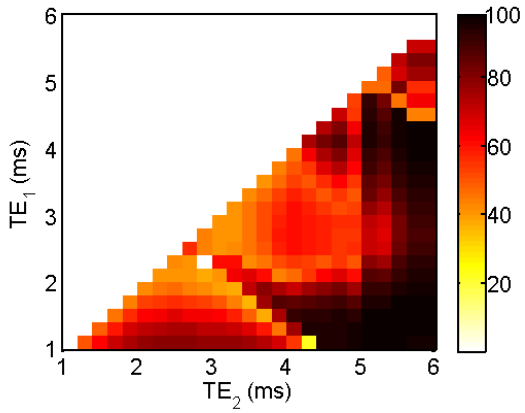

Figure 6.8. Percentage of correctly identified pixels as a function of echo times for in vivo data.

Figure 6.9 shows *in vivo* separated water and fat images obtained using the proposed physicality requirement alone at various *TE* combinations along with reference images generated using a traditional phase correction method based on Xiang's Regional Iterative Phasor Extraction (RIPE) algorithm.[25] The fat and water reference images are shown in (a) and (b), respectively. In (c) and (d) are shown the results for TE_1/TE_2 values of 3/6 ms, for which approximately 95% of the pixels were identified correctly; in (e) and (f), 3/5.4 ms, for which 85% accuracy was achieved; and in (g) and (h) 1.4/2.8 ms, with only 63% accuracy. The best of these *TE* combinations was 3/6 ms, in which case misidentification of the water and fat pixels tended to occur most often at tissue boundaries where SNR was low and other factors that cause additional signal deviation from the ideal model may have been present, such as T_2* decay.

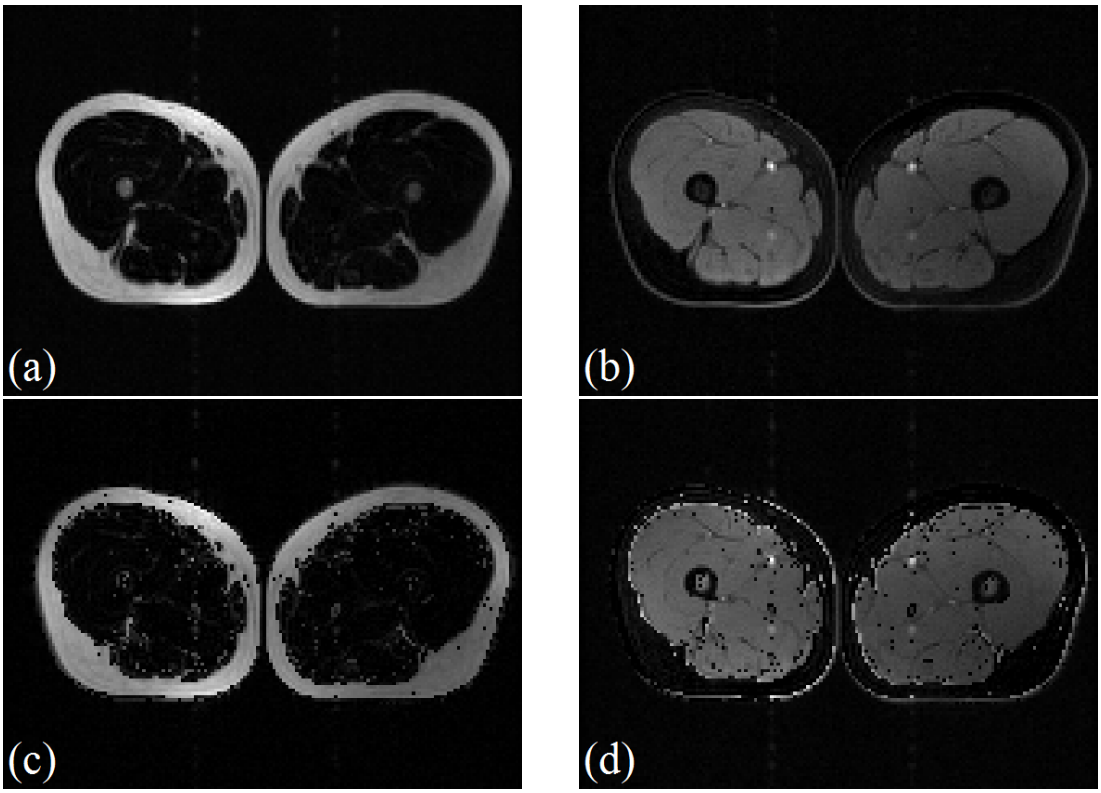

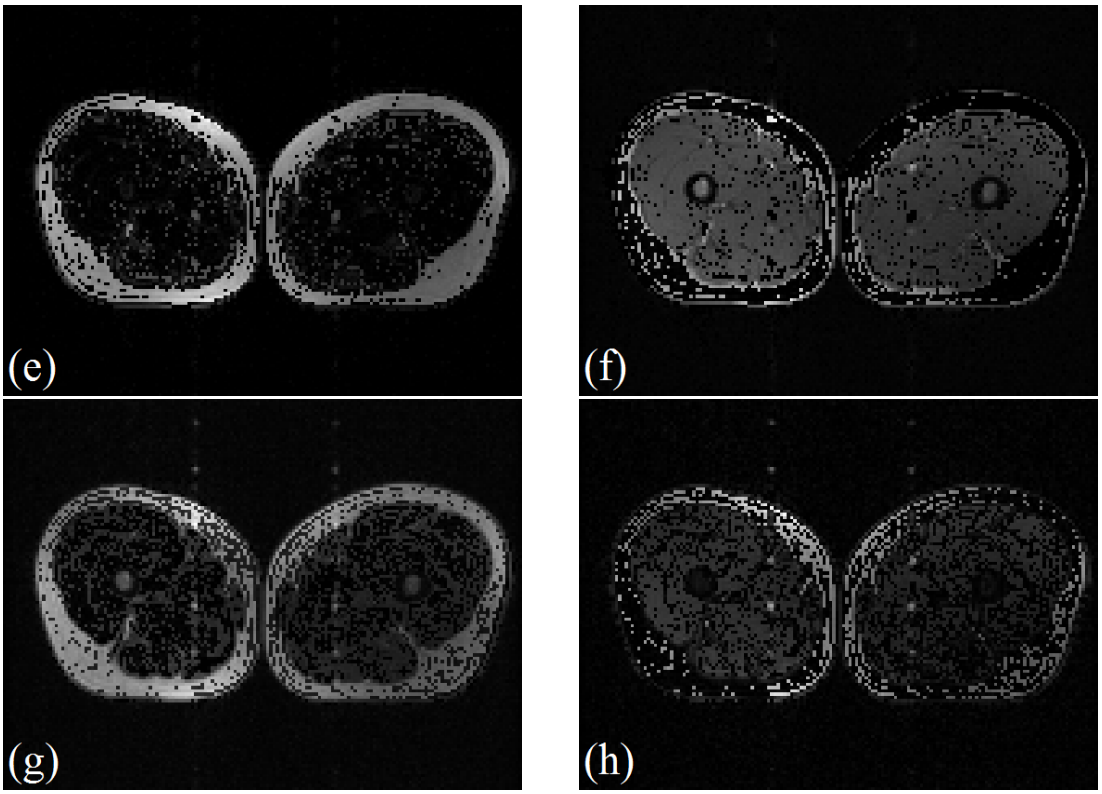

Figure 6.9. (a) Fat and (b) water images obtained by conventional phase correction for reference. (c) Fat and (d) water for 3/6 ms; 95% correct. (e) Fat and (f) water for 3/5.4 ms; 85% correct. (f) Fat and (g) water for 1.4/2.8 ms; 63% correct.

6.4. Discussion and Conclusions

Correct water and fat separation by the multi-point Dixon techniques has mostly relied on the success of phase correction and in general has been a challenge. For the two-point Dixon approach, flexible echo times and inclusion of the multiple-peak fat model open the possibility of correctly separating water and fat using the physicality requirement alone without phase correction. The advantage of this approach is that the selection of the correct solution is based on the magnitudes of the measured signals, and therefore local magnetic field inhomogeneity and other factors contributing to the signal phase (such as eddy currents) do not need to be considered.

It should be noted, however, that any factors affecting the signal magnitude will impact the reliability of fat and water identification. For example, random noise will cause variation in the size of the signal ellipses and can move the correct solution into an unphysical region or move the incorrect solution into a physical region. Therefore, some care needs to be taken when selecting a threshold for what is considered the "unphysical" region. One approach is to obtain an estimate of the expected error in W and F values based on the noise levels in the acquired images and to reject as unphysical all solutions that are negative by more than some specified multiple of the magnitude of this error. Another approach is to calculate how negative the unphysical solutions are expected to be for pure water or pure fat pixels and then set the threshold equal to some specified fraction of this amount. We found that either approach produced similar results.

Another factor that can impact the magnitude of the signal is the T_2* decay due to magnetic field inhomogeneity. For gradient echo sequences, T_2* causes an exponential decay of the signal magnitude as a function of TE and is not accounted for in the signal equations. The error in water, fat, and phasor values due to T_2* decay was explored in Chapter 5; the exact impact of this error on the ability to identify fat and water based on physicality alone warrants further study. We note, however, that the presence of a substantial T_2* signal decay is expected to directly change how this method can be applied.

Several approaches have previously been reported for resolving the ambiguity in water and fat separation in multi-point Dixon techniques without relying on the spatial smoothness of the background phase or phase correction. Xiang showed that the two complex solutions for water and fat from an asymmetrically sampled three-point Dixon

technique can be discriminated based on their relative phase angle and by exploiting the fact that the resonance frequency of fat is known to be lower than that of water.[28] Unfortunately, such an approach based on the relative phase angle of the two solutions is not applicable to symmetrically acquired images; and even for asymmetrically acquired images, it is only applicable *in vivo* to a small number of pixels with a substantial amount of both water and fat.

In a symmetrically sampled two-point Dixon technique, Ahmad et al. showed that the histogram of the magnitude images which reflects the different *TE*-dependence of the water and fat signals can be used to make a statistically correct water and fat identification.[29] Recently, Eggers showed that for two-point Dixon imaging with flexible echo times, water and fat identification can be made by considering a total of four sets of possible solutions involving only the magnitude of the acquired signals.[27] The basic idea of our method is similar, but we base our analysis on a geometric interpretation of the problem and consider a total of only two solutions.

Our phantom and *in vivo* images indicate that even at the best echo time combinations and a relatively high SNR, there are still pixels for which erroneous water-fat identification occurs when using the physicality requirement alone. However, our results also show that a reliability of over 80% is readily achievable for a large range of *TE* combinations at a reasonable SNR. These results can be combined with other processing methods to improve the overall performance in the final water and fat separation. The challenges of the various phase correction approaches can be reduced and their performance can be improved when a first-pass solution with correct water and fat separation in a majority of pixels is available.

In summary, we have presented in this chapter a method for direct fat and water determination based on our intuitive geometric interpretation of the two-point Dixon problem. This interpretation was used to help understand the conditions under which it is possible to identify water and fat with no need for phase correction. In particular, we identified with systematic computer simulation and confirmed with phantom and *in vivo* experiments a range of TE_1/TE_2 combinations and of SNR levels under which water and fat can be correctly separated using the physicality requirement alone. These results are expected to be useful for guiding the selection of an optimal set of imaging parameters for data acquisition and as a first-pass solution to help improve the overall performance in water and fat separation by other properly-designed post-processing methods.

Chapter 7

General Discussion

In the preceding chapters, we have presented the following:

- a generalized solution to the two-point Dixon problem for two arbitrary chemical species with independent dispersion and decay rates
- a geometric interpretation that facilitates an intuitive understanding of noise performance and direct fat-water identification
- an analysis of the error due to signal noise in the W, F, and p_{rel} values, as well as the dependence of this error on both the TE values and fat fraction
- an analysis of the error due to T_2^* signal decay in the same quantities
- an analysis of the ability to identify fat and water without phase correction based on physicality of possible solutions

Although the generalized solution has no obvious applications in the context of water-fat imaging, we have presented it nevertheless for the sake of completeness and in hopes that it may find some unforeseen use perhaps in another context.

The geometric interpretation, on the other hand, is quite useful in all aspects of two-point Dixon imaging. Recognizing that the scale of the signal ellipse is proportional to the magnitude of the corresponding signal, we immediately have a way to visualize the effects of noise (which changes the magnitude of the signal slightly) and T_2^* decay (which reduces the magnitude). The eccentricities of the ellipses and their relative orientation enable us to visualize the amount by which the possible solutions will be moved when the ellipses are both rescaled by noise. Intuitively, oppositely oriented ellipses with high eccentricity will yield the best noise performance; this condition corresponds to one image with water and fat in phase and one image with water and fat 180° out of phase. Furthermore, the symmetry of the ellipses under the single-peak model ensures the ambiguity of solutions, while the broken symmetry of the multi-peak model enables us to eliminate unphysical solutions by discarding intersection points that are outside of the first quadrant.

In our investigation of error due to signal noise, we found that within the *TE* ranges of interest (i.e., a few ms), there is little difference between the single-peak and multi-peak models. The most important difference is that, at 1.5 T, the opposed-phase echo time becomes 2.53 ms instead of the traditional 2.3 ms, while the in-phase echo time becomes 5.09 ms instead of the traditional 4.6 ms. Echo times close

to these values yield the best noise performance, though acceptable results are still achievable with echo times that deviate substantially from these values. Important restrictions remain that neither the sum nor the difference of the fat-water phases corresponding to the two echo times can add to an integer multiple of 360°.

Due to the fact that T_2^* decay also causes a slight rescaling of the ellipses, we found that the effects of T_2^* are similar to those of noise. Most importantly, the same *TE* combinations that should be avoided due to poor noise performance must also be avoided in order to prevent large error due to T_2^*. The echo times at which error due to T_2^* is minimized, however, are not the same as those at which error due to signal noise is minimized. This is a result of the fact that, unlike noise, T_2^* error systematically results in only the reduction of the second signal relative to the first. Thus, the signal ellipse corresponding to the second echo time is always slightly smaller than it would be in the absence of signal decay. We found that error in the water values due to T_2^* is minimized for certain TE_1 values, specifically 1.3 and 3.8 ms (at 1.5 T). Phasor error due to T_2^* is still minimized at *TE* combination of 2.53 ms and 5.09 ms.

The broken symmetry due to the multi-peak nature of fat makes it possible in principle to identify pixels as water-dominant or fat-dominant without phase correction for nearly any *TE* combination. This is because the incorrect solution is rotated outside of the first quadrant and can be discarded as unphysical. Under realistic conditions, however, we encounter two problems. First, for pixels that contain mixtures of fat and water, both possible solutions lie in the interior of the

first quadrant, far from the *W* and *F* axes. As a result, the rotation that occurs due to the break in symmetry is insufficient to move either solution outside of the first quadrant, and the ambiguity remains. To ensure that as many mixed pixels as possible are accurately identified, we therefore wish to choose echo times for which the incorrect solution is rotated as far as possible outside of the first quadrant. This only happens for certain *TE* combinations, and they tend to have relatively poor noise performance. As a result, care must be taken to balance the objectives of good noise performance and accurate direct fat-water identification. The second problem is that noise can cause correct (incorrect) solutions to be moved to the unphysical (physical) region. Again, to avoid this, we must choose echo times for which the amount by which the incorrect solutions are outside of the first quadrant is greater than the magnitude of error due to noise. Furthermore, thresholds must be chosen carefully for determining whether a solution counts as physical or unphysical.

The separate investigations described above all have implications for how the echo times should be chosen when performing the two-point Dixon technique. In the first investigation, we found the error due to signal noise at different *TE* combinations. In the second, we examined error due to T_2^* decay. And in the third, we quantified the accuracy of fat-water identification without phase correction at different *TE* combinations. The two objectives of minimizing error and optimizing the accuracy of fat-water determination must be balanced with each other and with the objective of shortening scan time. In the following, we present an example of how one might go about balancing these objectives using concrete numbers.

Given an expected SNR value in the images we plan to acquire, we may begin by requiring that the error in water values due to signal noise be less than 10%. (Since it is the water image that is most often examined for diagnostic purposes, it is natural to set limits on the error in this image. Limits may, of course, be placed on fat error as well.) This then eliminates certain echo time combinations, leaving only those shown in black in Figure 7.1(a). If we plan to use a phasor selection algorithm to resolve the ambiguity of solutions, we may also wish to ensure that the difference between the two possible phasors is larger than the expected phasor error. For example, we may require that the difference be at least four times the expected error magnitude. The *TE* combinations shown in black in Figure 7.1(b) satisfy this criterion. Similarly, given an expected T_2^* value for the tissue that we plan to image, we may wish to use only those *TE* combinations for which error due to T_2^* decay is less than 10%, shown in Figure 7.1(c). If we wish to attempt direct determination of water and fat by physicality alone, we may wish to restrict ourselves to *TE* combinations for which simulation tells us we can achieve an accuracy of 90% or better, as shown in Figure 7.1(d).

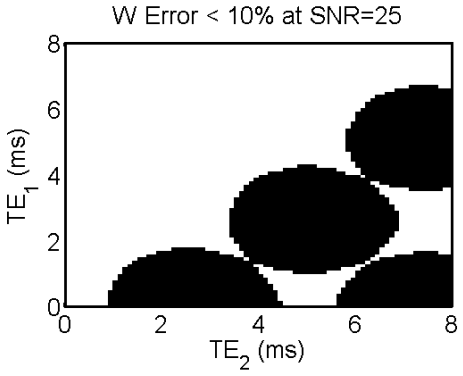

(a)

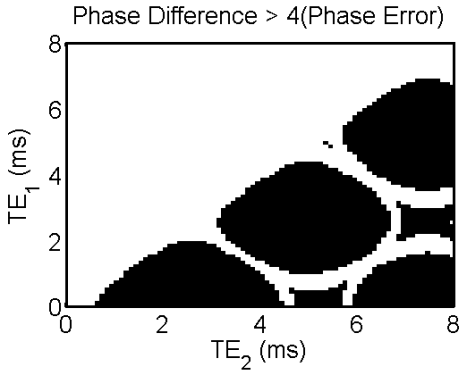

(b)

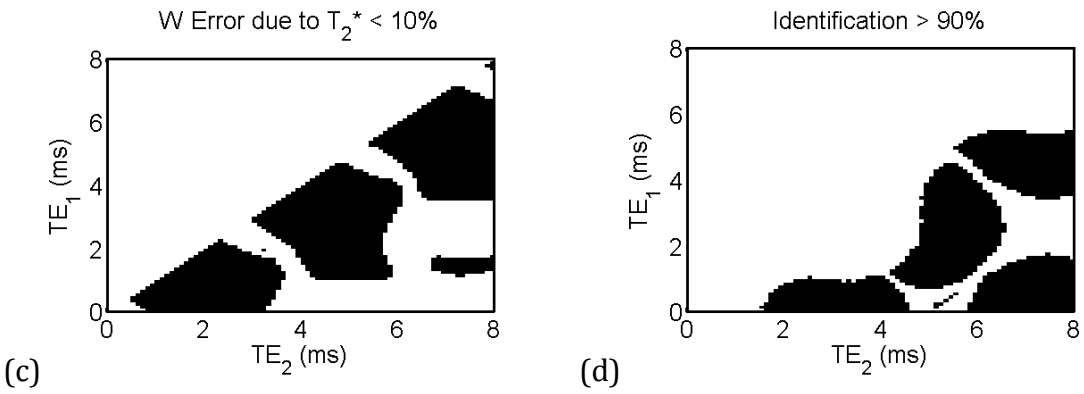

Figure 7.1. The black regions indicate TE combinations that satisfy the stated criteria. (a) W error due to signal noise is less than 10%. (b) The difference between the two possible background phase angles is more than four times the error due to noise. (c) W error due to T_2 is less than 10%. (d) At least 90% of pixels can be correctly identified without phase correction.*

Putting all of these requirements together will give us a final set of *TE* combinations from which to choose, as shown in Figure 7.2. Such an algorithm could be incorporated into existing Dixon imaging scan protocols in commercial scanners either to automatically select optimal echo times or to restrict *TE* values that are available for technicians to choose.

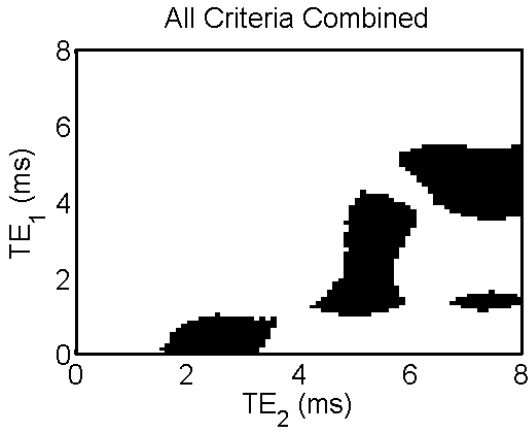

Figure 7.2. TE combinations for which all of the criteria described are satisfied.

In the years since the Dixon technique was first conceived, much effort has been invested in developing phase correction algorithms to ensure accurate fat-water separation. Besides a novel geometric interpretation of the two-point Dixon problem, the primary significance of the present work is the demonstration that the multi-peak nature of fat may be taken advantage of to achieve accurate fat-water separation either with no phase correction at all or with a phase correction algorithm made more robust by the inclusion of the physicality requirement. Since the reliability of this method of fat-water determination depends heavily on echo times, the recent development of flexible echo times is instrumental to this advancement. Furthermore, accurate quantification of noise performance and other sources of error such as T_2^* decay is essential to determine thresholds for rejecting solutions as unphysical. It is only by combining the advancements of flexible echo times and the multi-peak fat model with a thorough understanding of noise performance and other limitations of the signal model that this method of direct water and fat determination has been made possible.

Chapter 8

Conclusions

- For a voxel that contains unknown amounts of water (*W*) and fat (*F*), the equation for the magnitude of the emitted MR signal at a given echo time represents an ellipse in the *W*-*F* plane. In two-point Dixon imaging, where separate signals are acquired at two different echo times, the fat-water separation problem amounts to finding the intersection points of two such ellipses and then applying further assumptions, such as smoothness of the relative background phasor or non-negativity of *W* and *F*, to determine which intersection point corresponds to the true solution.

- For any model in which fat is assumed to have only one resonance peak (traditionally 3.35 ppm below that of water) and the water and fat signals are assumed to decay at the same rate (or not at all), the ellipses represented by the signal equations will be symmetric across the line $F = W$. Due to this symmetry, both the correct solution (which must be non-negative apart from

the effects of noise or inaccuracies in our model) and its reflection across the line $F = W$ will lie in the physically allowable first quadrant. To determine which of these two points is the correct solution, a phase correction algorithm must be applied which assumes a spatially smooth relative background phasor.

- When a multi-peak fat model is used, the symmetry of the signal ellipse across the line $F = W$ is broken. The angle by which the ellipse tilts away from this line is a function of the magnitude of the fat signal relative to its initial value, which is in turn a function of the echo time. For a two-point Dixon acquisition, it then becomes possible for the signal ellipses to be tilted in such a way that only one intersection point remains in the first quadrant. When this occurs, the ambiguity is directly resolved without phase correction.

- The freedom to choose flexible echo times, as opposed to the traditional in-phase and opposed-phase times, allows us to independently tune the degree to which the two ellipses are tilted. It then becomes possible to create conditions under which only water-dominant pixels have a unique physical solution, only fat-dominant pixels have a unique physical solution, both water- and fat-dominant pixels have a unique physical solution, or neither water- nor fat-dominant pixels have a unique physical solution. Furthermore, we can control to some extent the amount by which the unphysical solution falls outside of the physical region.

- The effects of noise can cause the correct solution to fall slightly outside of the first quadrant. Therefore, we cannot reject outright all unphysical solutions. Instead, based on the noise level, we must specify a threshold such that solutions that are negative by more than a certain amount can be assumed to be incorrect. Furthermore, the echo times must be chosen so that the amount by which the incorrect solutions fall outside of the first quadrant is greater than the error due to signal noise.

- In light of the above considerations, attention to noise performance as a function of echo times is important for several reasons. First, we wish to choose echo times for which the effects of noise will be relatively small. This will not only minimize the error in our final *W* and *F* values, but it will also reduce the frequency of instances in which correct (incorrect) solutions are rejected (retained) because they have been moved by noise out of (into) the first quadrant. Second, we must be able to estimate the error due to noise in order to choose appropriate thresholds for rejecting unphysical solutions. Third, we must be sure that the error due to noise is smaller than the amount by which incorrect solutions fall outside of the first quadrant.

- Accurate quantification of error in *W*, *F*, and phasor values due to signal noise is possible both by analytic calculation and by simulation. Good agreement with experimental results indicates that our model is accurate and that the error estimates can be used reliably for setting appropriate thresholds and choosing echo times to minimize the error due to noise.

- The effect of signal noise on the corresponding ellipse is to change its scale slightly. Neither the tilt angle nor the eccentricity is affected by noise. The effects of noise are minimized when the two ellipses are oppositely oriented and have high eccentricity. This corresponds to the traditional in-phase and opposed-phase echo times.

- Noise performance as a function of echo times for the multi-peak fat model is very similar to that for the traditional single-peak model. The primary difference is that the periodicity of the error as a function of echo time is broken by the dispersion of the fat signal (since the signal never exactly rephases to its original value). However, the broken periodicity is not a problem since, in the context of fast imaging, we are generally only interested in short echo times that fall within the first period anyway.

- Since our signal model neglects T_2^* decay, we know that there is some inherent error in all of our results. The decay of the signal results in a smaller signal magnitude, and hence a smaller ellipse. The resulting error is therefore similar to that caused by signal noise (which also rescales the ellipses). However, signal decay can only cause the ellipses to shrink, and the amount by which the ellipses shrink will be greater for longer echo times. Error caused by T_2^* decay is therefore systematic and is not exactly the same as error caused by noise. Nevertheless, it can be estimated, and echo times can be identified at which T_2^* error is relatively small.

- Ultimately, echo times should be chosen to balance the objectives of minimizing error due to noise and T_2^* decay while optimizing the ability to identify fat and water. At 1.5 T, echo times in the vicinity of TE_1 = 3 ms and TE_2 = 6 ms yield satisfactory results.

- The geometric interpretation of the two-point Dixon problem can be generalized for any two chemical species with multiple peaks and independent decay rates. In fact, we suggest that it can be further generalized for *n* chemical species, in which case the equations give *n* *n*-dimensional hyper-ellipsoids, the intersections of which are the possible solutions.

Appendix A:
Analytical Calculation of Error Due to Signal Noise

We want to find the standard deviation of W, F, and α (the phase angle of p_{rel}) for a given level of noise in the signal. Since signal noise is Gaussian with the same standard deviation σ_S in both the real and imaginary parts, the net effect can be expressed as follows:

$$\sigma_W = \sqrt{\left|\frac{\partial W}{\partial S_{1R}}\right|^2 + \left|\frac{\partial W}{\partial S_{1I}}\right|^2 + \left|\frac{\partial W}{\partial S_{2R}}\right|^2 + \left|\frac{\partial W}{\partial S_{2I}}\right|^2}\,\sigma_S$$

$$\sigma_F = \sqrt{\left|\frac{\partial F}{\partial S_{1R}}\right|^2 + \left|\frac{\partial F}{\partial S_{1I}}\right|^2 + \left|\frac{\partial F}{\partial S_{2R}}\right|^2 + \left|\frac{\partial F}{\partial S_{2I}}\right|^2}\,\sigma_S$$

$$\sigma_\alpha = \sqrt{\left|\frac{\partial \alpha}{\partial S_{1R}}\right|^2 + \left|\frac{\partial \alpha}{\partial S_{1I}}\right|^2 + \left|\frac{\partial \alpha}{\partial S_{2R}}\right|^2 + \left|\frac{\partial \alpha}{\partial S_{2I}}\right|^2}\,\sigma_S$$

Berglund's Method

The derivatives of W are given by

$$\frac{\partial W}{\partial S_{1R,I}} = \frac{1}{|S_1| Z_W^{3/2}} \cdot \left\{ S_{1R,I} Z_W - |S_1|^2 \left[\frac{a_{1R} b_{1R} + a_{1I} b_{1I}}{(1-Q)^2} + \frac{|b_1|^2 Q}{(1-Q)^3} \right] \frac{\partial Q}{\partial S_{1R,I}} \right\}$$

$$\frac{\partial W}{\partial S_{2R,I}} = -\frac{|S_1|}{Z_W^{\frac{3}{2}}} \cdot \left[\frac{a_{1R} b_{1R} + a_{1I} b_{1I}}{(1-Q)^2} + \frac{|b_1|^2 Q}{(1-Q)^3} \right] \frac{\partial Q}{\partial S_{2R,I}}$$

where

$$Z_W = |a_1|^2 + 2(a_{1\mathrm{R}}b_{1\mathrm{R}} + a_{1\mathrm{I}}b_{1\mathrm{I}})\frac{Q}{(1-Q)} + |b_1|^2\left(\frac{Q}{1-Q}\right)^2$$

The derivatives of F are given by

$$\frac{\partial F}{\partial S_{1R,I}} = \frac{1}{|S_1|Z_F^{3/2}} \cdot \left\{ S_{1R,I}Z_F + |S_1|^2 \left[\frac{a_{1R}b_{1R} + a_{1I}b_{1I}}{Q^2} + \frac{|a_1|^2(1-Q)}{Q^3} \right] \frac{\partial Q}{\partial S_{1R,I}} \right\}$$

$$\frac{\partial F}{\partial S_{2R,I}} = \frac{|S_1|}{Z_F^{3/2}} \cdot \left[\frac{a_{1R}b_{1R} + a_{1I}b_{1I}}{Q^2} + \frac{|a_1|^2(1-Q)}{Q^3} \right] \frac{\partial Q}{\partial S_{2R,I}}$$

where

$$Z_F = |a_1|^2\left(\frac{1-Q}{Q}\right)^2 + 2(a_{1\mathrm{R}}b_{1\mathrm{R}} + a_{1\mathrm{I}}b_{1\mathrm{I}})\frac{(1-Q)}{Q} + |b_1|^2$$

The derivatives of α are given by

$$\frac{\partial \alpha}{\partial S_{1R}} = \frac{1}{ip}\left(-\frac{p}{S_1} + A\frac{\partial Q}{\partial S_{1R}}\right)$$

$$\frac{\partial \alpha}{\partial S_{1I}} = \frac{1}{ip}\left(-\frac{ip}{S_1} + A\frac{\partial Q}{\partial S_{1I}}\right)$$

$$\frac{\partial \alpha}{\partial S_{2R}} = \frac{1}{ip}\left(\frac{p}{S_2} + A\frac{\partial Q}{\partial S_{2R}}\right)$$

$$\frac{\partial \alpha}{\partial S_{2I}} = \frac{1}{ip}\left(\frac{ip}{S_2} + A\frac{\partial Q}{\partial S_{2I}}\right)$$

where for brevity we now represent p_{rel} simply as p, and

$$A = \frac{S_2(b_1 - a_1) - S_1(b_2 - a_2)p}{S_1[a_2 + (b_2 - a_2)Q]}$$

In all of the above formulas, Q is given by

$$Q = \frac{c_1 \pm \sqrt{c_3}}{c_1 + c_2}$$

where c_1, c_2, and c_3 are the same as the constants defined for the generalized version of Berglund's solution in Chapter 3. Continuing with the chain rule, we get

$$\frac{\partial Q}{\partial x} = \frac{(c_1 + c_2)\left(\frac{\partial c_1}{\partial x} \pm \frac{1}{2\sqrt{c_3}}\frac{\partial c_3}{\partial x}\right) - \left(c_1 \pm \sqrt{c_3}\right)\left(\frac{\partial c_1}{\partial x} + \frac{\partial c_2}{\partial x}\right)}{(c_1 + c_2)^2}$$

where x can stand for any of S_{1R}, S_{1I}, S_{2R}, or S_{2I}.

For c_1:

$$\frac{\partial c_1}{\partial S_{1R,I}} = 2S_{1R,I}[|a_2|^2 - Re(a_2^* b_2)]$$

$$\frac{\partial c_1}{\partial S_{2R,I}} = -2S_{2R,I}[|a_1|^2 - Re(a_1^* b_1)]$$

For c_2:

$$\frac{\partial c_2}{\partial S_{1R,I}} = 2S_{1R,I}[|b_2|^2 - Re(a_2^* b_2)]$$

$$\frac{\partial c_2}{\partial S_{2R,I}} = -2S_{2R,I}[|b_1|^2 - Re(a_1^* b_1)]$$

For c_3:

$$\frac{\partial c_3}{\partial S_{1R,I}} = 2S_{1R,I}\left\{|a_1 a_2 S_2|^2 \left|\frac{b_1}{a_1} - \frac{b_2}{a_2}\right|^2 + 2\mathrm{Im}(a_2^* b_2)[|S_2|^2 \mathrm{Im}(a_1^* b_1) - |S_1|^2 \mathrm{Im}(a_2^* b_2)]\right\}$$

$$\frac{\partial c_3}{\partial S_{2R,I}} = 2S_{2R,I}\left\{|a_1 a_2 S_1|^2 \left|\frac{b_1}{a_1} - \frac{b_2}{a_2}\right|^2 - 2\mathrm{Im}(a_1^* b_1)[|S_2|^2 \mathrm{Im}(a_1^* b_1) - |S_1|^2 \mathrm{Im}(a_2^* b_2)]\right\}$$

Wherever a "$\pm$" sign occurs, the sign corresponding to that of the correct solution must be chosen. That is, for each set of input values (TE_1, TE_2, W, and F), the two possible values of Q must be calculated; the one that matches the input values determines which sign should be chosen in computing the derivatives in all of the above formulas.

Eggers' Method

Similar results for Eggers' method were derived as follows. The derivatives for W are given by

$$\frac{\partial W}{\partial S_{1R,I}} = -\frac{\beta_1}{|a_1|^2}\frac{\partial F}{\partial S_{1R,I}} \pm \frac{|a_1|^2 S_{1R,I} + (\beta_1^2 - |a_1 b_1|^2)F\frac{\partial F}{\partial S_{1R,I}}}{|a_1|^2\sqrt{|a_1 S_1|^2 + (\beta_1^2 - |a_1 b_1|^2)F^2}}$$

$$\frac{\partial W}{\partial S_{2R,I}} = -\frac{\beta_1}{|a_1|^2}\frac{\partial F}{\partial S_{2R,I}} \pm \frac{(\beta_1^2 - |a_1 b_1|^2)F\frac{\partial F}{\partial S_{2R,I}}}{|a_1|^2\sqrt{|a_1 S_1|^2 + (\beta_1^2 - |a_1 b_1|^2)F^2}}$$

The derivatives for F are

$$\frac{\partial F}{\partial x} = \frac{1}{2\sqrt{-2c_1}} \frac{1}{\sqrt{c_2 \pm \sqrt{c_2^2 - 4c_1c_3}}} \left[\frac{\partial c_2}{\partial x} \pm \frac{c_2 \frac{\partial c_2}{\partial x} - 2c_1 \frac{\partial c_3}{\partial x}}{\sqrt{c_2^2 - 4c_1c_3}} \right]$$

where x can stand for any of S_{1R}, S_{1I}, S_{2R}, or S_{2I}, and the constants c_1, c_2, and c_3 are the same as the constants defined for the generalized version of Eggers' solution in Chapter 3.

The derivatives for α are

$$\frac{\partial \alpha}{\partial S_{1R}} = \frac{1}{ip} \left[\frac{LS_2 - S_1^* S_2 B(S_{1R})}{L^2} \right]$$

$$\frac{\partial \alpha}{\partial S_{1I}} = \frac{1}{ip} \left[\frac{-iLS_2 - S_1^* S_2 B(S_{1I})}{L^2} \right]$$

$$\frac{\partial \alpha}{\partial S_{2R}} = \frac{1}{ip} \left[\frac{LS_1^* - S_1^* S_2 B(S_{2R})}{L^2} \right]$$

$$\frac{\partial \alpha}{\partial S_{2I}} = \frac{1}{ip} \left[\frac{iLS_1^* - S_1^* S_2 B(S_{2I})}{L^2} \right]$$

where

$$L = (a_1^* W + b_1^* F)(a_2 W + b_2 F)$$

and, once again allowing x to stand for any of S_{1R}, S_{1I}, S_{2R}, or S_{2I},

$$B(x) = \left(a_1^* \frac{\partial W}{\partial x} + b_1^* \frac{\partial F}{\partial x} \right) (a_2 W + b_2 F) + (a_1^* W + b_1^* F) \left(a_2 \frac{\partial W}{\partial x} + b_2 \frac{\partial F}{\partial x} \right)$$

To carry these derivatives out fully using the chain rule, we must also provide the derivatives of c_2, and c_3 as follows. (Note that c_1 has no signal dependence.)

$$\frac{\partial c_2}{\partial S_{1R,I}} = -4[2\beta_2(|a_1|^2\beta_2 - |a_2|^2\beta_1) - |a_2|^2(|a_1 b_2|^2 - |a_2 b_1|^2)]S_{1R,I}$$

$$\frac{\partial c_2}{\partial S_{2R,I}} = 4[2\beta_1(|a_1|^2\beta_2 - |a_2|^2\beta_1) - |a_1|^2(|a_1 b_2|^2 - |a_2 b_1|^2)]S_{2R,I}$$

$$\frac{\partial c_3}{\partial S_{1R,I}} = 4(|S_1 a_2|^2 - |S_2 a_1|^2)|a_2|^2 S_{1R,I}$$

$$\frac{\partial c_3}{\partial S_{2R,I}} = -4(|S_1 a_2|^2 - |S_2 a_1|^2)|a_1|^2 S_{2R,I}$$

As in Chapter 3, $\beta_1 = a_{1\mathrm{R}}b_{1\mathrm{R}} + a_{1\mathrm{I}}b_{1\mathrm{I}}$ and $\beta_2 = a_{2\mathrm{R}}b_{2\mathrm{R}} + a_{2\mathrm{I}}b_{2\mathrm{I}}$. Again, wherever a "$\pm$" sign occurs, the sign corresponding to that of the correct solution must be chosen.

Appendix B:
Implementation with Multiple Coils

When an image is acquired using multiple receiver coils, the data for a single slice is a 3D array in which the first two dimensions are spatial (the dimensions of the slice) and the third dimension is the coil number. For example, if there are 8 coils, the data set is essentially 8 separate images, each of which has high SNR in just one region of the FOV (the region near that particular coil). When the images are combined, the result is an image with (hopefully) uniformly good SNR.

Combining the data from multiple coils can be tricky when phase information must be preserved (as in the case of Dixon imaging). Choosing an effective method is especially important when Dixon imaging is combined with parallel imaging.

Recalling that the signal equations are

$$S_1 = (a_1 W + b_1 F) e^{i\varphi_1}$$

$$S_2 = (a_2 W + b_2 F) e^{i\varphi_2}$$

we first note that for N coils, we now have N pairs of equations, one pair for each coil. We must eliminate the phase factors, which are coil-dependent, so that we can then simply add the modified signals to obtain a single composite complex image for each echo time.

Note that W and F implicitly depend on coil sensitivity and are therefore coil-dependent. The background phasors $e^{i\varphi_1}$ and $e^{i\varphi_2}$ are also coil-dependent, but the

change in phase from TE_1 to TE_2, $e^{i\alpha} = e^{i(\varphi_2 - \varphi_1)}$, is coil-independent. The coefficients a and b are also coil-independent, since they only depend on the properties of the tissue and the echo times. Therefore, using k as an index to denote coil number, the signal equations can be rewritten as

$$S_{1k} = (a_1 W_k + b_1 F_k) e^{i\varphi_{1k}}$$

$$S_{2k} = (a_2 W_k + b_2 F_k) e^{i\varphi_{1k}} e^{i\alpha}$$

We proceed as follows. First, using either Berglund's or Eggers' method, we solve for the possible values of either Q_k or W_k and F_k and calculate the corresponding relative background phasors. The phasor $e^{i\varphi_{1k}}$ can then be calculated for each coil, and we can divide the signals S_{1k} by $e^{i\varphi_{1k}}$ and S_{2k} by $e^{i\varphi_{1k}} e^{i\alpha}$ to get the following modified signals.

$$S'_{1k} = a_1 W_k + b_1 F_k$$

$$S'_{2k} = a_2 W_k + b_2 F_k$$

Defining $W' = \sum_k W_k$ and $F' = \sum_k F_k$, we then obtain combined signals for the two echo times by taking the sum:

$$S_1{}^{com} = \sum_{k=1}^{N} S'_{1k} = a_1 W' + b_1 F'$$

$$S_2{}^{com} = \sum_{k=1}^{N} S'_{2k} = a_2 W' + b_2 F'$$

Using the smoothed phase map, these combined signals can then be used to generate the re-estimated W and F matrices according to Berglund's least-squares method. Since the values of W_k and F_k are already naturally weighted by coil sensitivity, *W'* and *F'* are effectively weighted averages in which the values from coils with higher SNR are given greater weight and values from coils with lower SNR are given lesser weight. Note that if the sum-of-squares method were used, then *W* and *F* would be forced to take on positive values, in which case the non-negativity criterion could no longer be used in the fat-water identification process described in Chapter 6.

References

1. Dixon WT. Simple Proton Spectroscopic Imaging. Radiology 1984(153):189-194.
2. Delfaut EM, Beltran J, Johnson G, Rousseau J, Marchandise X, Cotten A. Fat Suppression in MR Imaging: Techniques and Pitfalls. Radiographics 1999;19(2):373-382.
3. Daly CP, Jaeger B, Sill DS. Variable appearances of fat necrosis on breast MRI. AJR American journal of roentgenology 2008;191(5):1374-1380.
4. Kellman P, Hernando D, Arai AE. Myocardial Fat Imaging. Current cardiovascular imaging reports 2010;3(2):83-91.
5. Berglund J, Ahlstrom H, Johansson L, Kullberg J. Two-point dixon method with flexible echo times. Magnetic resonance in medicine : official journal of the Society of Magnetic Resonance in Medicine / Society of Magnetic Resonance in Medicine 2011;65(4):994-1004.
6. Eggers H, Brendel B, Duijndam A, Herigault G. Dual-echo Dixon imaging with flexible choice of echo times. Magnetic resonance in medicine : official journal of the Society of Magnetic Resonance in Medicine / Society of Magnetic Resonance in Medicine 2011;65(1):96-107.
7. Ren J, Dimitrov I, Sherry AD, Malloy CR. Composition of adipose tissue and marrow fat in humans by 1H NMR at 7 Tesla. Journal of lipid research 2008;49(9):2055-2062.
8. Ma J. Dixon techniques for water and fat imaging. Journal of Magnetic Resonance Imaging 2008;28(3):543-558.
9. Haacke EMB, Robert W.; Thompson, Michael R.; Venkatesan, Ramesh. Magnetic Resonance Imaging: Physical Principles and Sequence Design. New York: A John Wiley & Sons: 1999.
10. Le Bellac MM, Fabrice; Batrouni, G. George. Equilibrium and Non-Equilibrium Statistical Thermodynamics. 2004.
11. Aletras A. Basic MRI Physics. In: Kwong R, editor. Cardiovascular Magnetic Resonance Imaging, Contemporary Cardiology: Humana Press; 2008. p. 1-31.
12. Cheng H-LM, Stikov N, Ghugre NR, Wright GA. Practical medical applications of quantitative MR relaxometry. Journal of Magnetic Resonance Imaging 2012;36(4):805-824.
13. Hu HH, Bornert P, Hernando D, et al. ISMRM workshop on fat-water separation: insights, applications and progress in MRI. Magn Reson Med 2012;68(2):378-388.
14. Bydder GM, Young IR. MR imaging: clinical use of the inversion recovery sequence. Journal of computer assisted tomography 1985;9(4):659-675.
15. Haase A, Frahm J, Hanicke W, Matthaei D. 1H NMR chemical shift selective (CHESS) imaging. Phys Med Biol 1985;30(4):341-344.
16. Keller PJ, Hunter WW, Schmalbrock P. Multisection fat-water imaging with chemical shift selective presaturation. Radiology 1987;164(2):539-541.

17. Ma J. Breath-hold water and fat imaging using a dual-echo two-point Dixon technique with an efficient and robust phase-correction algorithm. Magnetic resonance in medicine : official journal of the Society of Magnetic Resonance in Medicine / Society of Magnetic Resonance in Medicine 2004;52(2):415-419.
18. Hernando D, Haldar JP, Sutton BP, Ma J, Kellman P, Liang ZP. Joint estimation of water/fat images and field inhomogeneity map. Magn Reson Med 2008;59(3):571-580.
19. Hernando D, Kellman P, Haldar JP, Liang ZP. Robust water/fat separation in the presence of large field inhomogeneities using a graph cut algorithm. Magn Reson Med 2010;63(1):79-90.
20. Xiang QS. Fat Suppression with Single Quadrature Acquisition. Proceedings of the 6th Annual Scientific Meeting of the ISMRM 1998:abstract 1880.
21. Xiang QS. Improved Single Point Water-Fat Imaging with Virtual Shimming. Proceedings of the 9th Annual Scientific Meeting of the ISMRM 2001:abstract 789.
22. Ma J. A single-point Dixon technique for fat-suppressed fast 3D gradient-echo imaging with a flexible echo time. J Magn Reson Imaging 2008;27(4):881-890.
23. Glover GH, Schneider E. Three-point Dixon technique for true water/fat decomposition with B0 inhomogeneity correction. Magn Reson Med 1991;18(2):371-383.
24. Yeung HN, Kormos DW. Separation of true fat and water images by correcting magnetic field inhomogeneity in situ. Radiology 1986;159(3):783-786.
25. Xiang QS. Two-point water-fat imaging with partially-opposed-phase (POP) acquisition: an asymmetric Dixon method. Magnetic resonance in medicine : official journal of the Society of Magnetic Resonance in Medicine / Society of Magnetic Resonance in Medicine 2006;56(3):572-584.
26. Lim TYM, J. Image-Based Determination of the Fat Signal Model for Dixon Water and Fat Imaging. Proceeedings of the 20th annual scientific meeting of the International Society of Magnetic Resonance in Medicine 2012:2483.
27. Eggers H. Water-Fat Identification in Dual-Echo Dixon Imaging. Proc Intl Soc Mag Reson Med 20 2011.
28. Xiang QS, An L. Water-fat imaging with direct phase encoding. J Magn Reson Imaging 1997;7(6):1002-1015.
29. Ahmad M, Liu Y, Slavens ZW, et al. A method for automatic identification of water and fat images from a symmetrically sampled dual-echo Dixon technique. Magn Reson Imaging 2010;28(3):427-433.